Université de Franche-Comté

École Doctorale SPIM

Thèse de Doctorat

En Cotutelle

Spécialité Sciences Pour l'Ingénieur

présentée par

Kirill Volyanskiy

Etudes spectrales du bruit de phase dans les oscillateurs opto-électroniques micro-ondes à ligne à retard

The study of phase noise spectra of a microwave delay line optoelectronic oscillator

Thèse dirigée par L. Larger, Professeur, Université de Franche-Comté,
E. Rubiola, Professeur, Université de Franche-Comté,
S.V. Kulakov, Professeur, Université Aérospatiale de St.Pétersbourg, Russie

soutenue le 31 Mars 2009

Jury :

Président :	R. Besson	Professeur délégué aux relations avec la Russie, UFC
Rapporteurs :	M. Prigent	Professeur, Université de Limoges, XLIM
	G. Brida	Chargé de recherche CNR, l'Institut National de la Recherche Métrologique, Italie
Examinateurs :	L. Larger	Professeur, UFC
	E. Rubiola	Professeur, UFC
	S.V. Kulakov	Professeur, Université Aérospatiale de St.Pétersbourg, Russie
	Y.V. Pisarevsky	Professeur, l'Institut de Cristallographie de A.V. Shoubnikov, Académie des Sciences de Russie
	Y.K. Chembo	Chercheur contractuel CNRS, FEMTO-ST

To my wife Anastassia, my father, my mother-in-law and to the memory of my mother, my father-in-law, and Liudmila Petrovna Konovalova.

Acknowledgements

This thesis was prepared in the Optics Laboratory named after P.M.Duffieux of the University of Franche-Comté (France) in collaboration with Saint-Petersburg State University of Aerospace Instrumentation (Russia).

I express my gratitude to professor Hervé Maillotte, Research Director of the laboratory for accepting me in the laboratory.

I express my deep gratitude to professor Laurent Larger who guided my work during these years. He almost always found some time for a scientific discussion although he was very busy by running various projects.

I am grateful to professor Enrico Rubiola who was co-director of the thesis, for numerous fruitful discussions of different aspects of noise metrology, for tips and tricks of this discipline. I could find many interesting ideas for realizing phase noise measurements due this.

I thank professor Sergey V. Kulakov who was also co-director of the thesis, guided my researches for several years and helped me in various ways.

I thank the President of the PhD examination board, professor Raymond Besson. He also helped me get acquainted with France and find the beautiful research team.

I thank my referees: professor Michel Prigent and senior researcher Giorgio Brida for considering my work and writing very favorable reviews.

I am grateful to researcher Yanne K. Chembo for numerous discussions on stochastic differential equations, for help in various mathematical problems and for being a jury member.

I am grateful to professor Yuri V. Pisarevsky for considering my work and for being a jury member.

I thank researcher Jean-Marc Merolla for numerous advices in the optical devices domain.

I thank Patrice Salzenstein for his support.

I am grateful to the French embassy in Russia for granting a scholarship to me.

I express my gratitude to everyone who helped in some way while I prepared this thesis.

I am grateful to Liudmila P. Konovalova who was the locomotive for most projects in the department of electronics and optical communication of the State University of Aerospace Instrumentation for many years and who encouraged me doing the thesis.

I thank Abdelhamid Hmima for his support. He is a real friend.

I express gratitude to members of my family. It would be much more difficult without their support.

And special gratitude to my wife Anastassia who supported me all the time.

Résumé

Ce manuscrit est consacré à l'étude du bruit de phase dans les oscillateurs optoélectroniques (OEO) à ligne à retard à fibre optique. Cette classe particulière d'oscillateurs dans la gamme micro-onde a été développée (1994) récemment, et étudiée par différents groupes de recherche dans le monde, du fait de son important potentiel en termes de très faible bruit de phase à court terme (applications radar, spatial, et télécom haut débit).

Sur la base d'un modèle théorique s'appuyant sur une description temporelle, nous avons étudié la dynamique de l'oscillateur, et ses propriétés de bruit de phase. L'équation différentielle stochastique, non linéaire, et à retard, est directement dérivée de la description des différents éléments de la chaîne d'oscillation : la non linéarité prédominante d'un modulateur électro-optique de Mach-Zehnder, le temps de retard induit par plusieurs kilomètres de fibre, la dynamique résonante du filtre micro-onde à 10 GHz sélecteur des modes à retard, et les différentes sources de bruit additif et multiplicatif (laser, photodiode, amplificateur RF). La linéarisation de ce modèle autour du point de fonctionnement a permis d'obtenir une expression théorique du bruit de phase et d'amplitude de l'OEO. Ces résultats sont confrontés à une exploration expérimentale des caractéristiques de bruit, à la fois des composants utilisés, et du système complet de l'OEO en régime d'oscillation monomode. Des techniques de mesure de bruit ultra-sensibles, utilisant des architectures opto-électroniques d'un banc de mesure, ainsi que des principes de mesure par corrélation, sont décrites. Une très bonne correspondance entre théorie et expérience est ainsi obtenue. Le travail a abouti à l'identification quantitative des principales sources de bruit limitant les performances de l'OEO. Par l'utilisation de composants optimaux, un niveau de bruit de phase de l'ordre de -143 dBrad^2/Hz à 10 kHz de la porteuse à 10 GHz, a été atteint. La discussion des sources de bruit résiduelles a également permis de proposer des améliorations pour les architectures futures d'OEO.

Abstract

This work is dedicated to the study of phase noise in fiber optic delay line optoelectronic oscillators (OEO). This particular class of microwave range oscillator was recently introduced (1994), and intensively explored due to its very attractive potential for ultra-low short term phase noise features. It is intended for applications to Radar, Space, and high bit rate optical telecommunications.

On the basis of a time domain theoretical approach, the dynamic and the phase noise properties of the OEO was investigated. A stochastic, nonlinear, delay differential equation was derived directly from the description of the oscillator loop chain: the most relevant nonlinearity of a Mach-Zehnder electro-optic modulator, the km-long fiber delay line, the dynamics ruled by the microwave amplitude selective filter, and the different additive and multiplicative noise sources (laser, photodiode, RF amplifier). The linearization of the model around the OEO monomode operating point led to the theoretical description of the phase and amplitude noise performances. Those theoretical results are compared with experimental investigations, covering both the device noise characteristics, as well as the whole oscillator. Specific high sensitivity noise measurement techniques were developed using optoelectronic architectures of the measurement bench on the one hand, and correlation principles on the other hand. A very good agreement between experiment and theory is obtained, leading to a quantitative description of the OEO phase noise features, and highlighting the most relevant noise sources limiting the performances. Selected devices allowed to achieve an OEO phase noise as low as -143 dBrad^2/Hz at 10 kHz from the carrier at 10 GHz. The remaining limiting noise sources are finally discussed, and various possible improvements are suggested for future OEOs.

Contents

List of Figures

List of Tables

List of abbreviations

AC	Alternating current
AM	Amplitude modulation
DC	Direct current
DFB	Distributed feedback
DRO	Dielectric resonator oscillator
DUT	Device under test
EDFA	Erbium-doped fiber amplifier
EOM	Electro-optical modulator
FFA	Feedforward amplifier
FSR	Free spectral range
IF	Intermediate frequency
LD	Laser diode
LO	Local oscillator
MMIC	Millimetre-wave Integrated Circuits
MZ	Mach-Zehnder
PD	Photodiode
PID	Proportionate-derivative-integral
PM	Phase modulation
PSD	Power spectral density
OE	Optoelectronic
OEO	Optoelectronic delay line oscillator
RA	Regenerative amplifier
RF	Radio-frequency
RHP	Right half plane
RIN	Relative intensity noise
SLCO	Sapphire loaded cavity oscillator
TEC	Thermoelectric cooler
VMDP	Velocity matched distributed photodetector
WGM	Whispering gallery mode

...

List of notations

General notations

b_i	coefficients of the power-law approximation of $S_\phi(f)$
c	the speed of light in vacuum
f	Fourier frequency, Hz
g_m	amplitude gain margin
j	imaginary unit, $j^2 = -1$
k	Boltzmann constant, $k = 1.386 \cdot 10^{-23}$ J/K
$n, n(\lambda)$	optical fiber refraction index, $n = 1.46$
q	electron charge, $q = 1.602 \cdot 10^{-19}$ C
s	complex variable, $s = \sigma + j\omega$
s_m	stability margin
$x(t)$	system parameter
$A(t)$	slowly varying amplitude
A	amplitude
$\mathcal{A}(t)$	slowly varying complex amplitude
D_λ	dispersion constant
$\mathbb{E}$	mathematical expectation
$\mathcal{F}$	noise figure of amplifier
F_{τ_d}	free spectral range produced by delay line
ΔF	filter bandwidth (also $\Delta\omega$)
G	amplitude gain of amplifier
$J_1(x)$	first order Bessel function of the first kind
$\mathcal{L}\{\cdot\}$	Laplace transform operator
$H(s)$	transfer function in Laplace s-domain
I_PD	photodiode current
L	delay line physical length
$\mathscr{L}$	single-sideband noise spectrum, dBc/Hz
$\mathbb{N}$	natural numbers
N_RIN	laser RIN PSD
$O(\cdot)$	asymptotic notation
P_opt	laser power
Q	quality factor
R	resistance

R_{eq}	equivalent load impedance for the photodiode
R_{PD}	current-voltage conversion resistance
$S_{\mathrm{a}}(f)$	one-sided power spectral density of the quantity a
T	temperature
T_0	reference temperature, $T_0 = 290$ K
V	DC or peak voltage
V_{B}	Mach-Zehnder EOM bias voltage
V_0	nominal amplitude
$V_{\pi\mathrm{B}}$	Mach-Zehnder EOM half-wave voltage of the bias input
$V_{\pi\mathrm{RF}}$	Mach-Zehnder EOM half-wave voltage of the RF input
$\alpha(t)$	amplitude noise
β	normalized loop gain
$\beta(s)$	feedback transfer function in Laplace s-domain
$\beta(j\omega)$	feedback transfer function in Fourier frequency domain
$\beta_{\mathrm{f}}(s)$	microwave filter transfer function in Laplace s-domain
γ	normalized gain parameter
$\delta(t)$	Dirac delta function
$\varepsilon(s)$	system sensitivity function
$\zeta_{\mathrm{a}}(t)$	complex Gaussian white noise
$\eta_{\mathrm{m}}(t)$	multiplicative noise
ϑ	RF filter selectivity parameter in the OEO differential equation, $\vartheta \simeq 1/(2Q)$
κ	amplitude attenuation
λ	wavelength
μ	RF filter selectivity parameter in the OEO differential equation, $\mu \simeq \Delta\omega/2$
ν	frequency (Hz), used for carriers
ν_0	nominal frequency (Hz), used for carriers
$\nu(t)$	instantaneous frequency, Hz
$\Delta\nu(t)$	frequency noise, Hz
$\xi_{\mathrm{a}}(t)$	additive noise, real Gaussian white noise
$\xi_{\mathrm{a}}(t)$	real Gaussian white noise
ρ	photodiode responsivity
ρ_φ	mixer phase-to-voltage conversion factor
σ	time jitter
$\varsigma(t)$	phase noise
τ_{d}	delay time
τ_{f}	microwave filter group delay
ϕ	phase, Mach-Zehnder EOM offset phase
$\varphi(t)$	phase noise
φ_{m}	phase margin
$\psi(t)$	oscillator phase
ω	angular frequency (both carrier and Fourier)
ω_0	oscillator angular frequency
ω_{m}	mode selection filter angular frequency
ω_{r}	resonator natural frequency
$\Theta(s)$	difference phase noise, $\mathcal{L}\{\theta(t)\}$

$\Phi(s)$	input phase noise, $\mathcal{L}\{\varphi(t)\}$
$\Psi(s)$	output phase noise, $\mathcal{L}\{\psi(t)\}$
$\Psi(j\omega)$	oscillator phase spectral density, $\Psi(j\omega) = \mathcal{F}\{\psi(t)\}$
...	

Chapter 1

l	mode number
n_r	relative degree
$y(t)$	normalized dimensionless frequency fluctuations
B_val	thermistor energy constant
C	contour in complex plane
$\mathrm{H}(s)$	phase transfer function, also $\mathrm{H}(jf)$
V_ol	output of the open-loop system
V_cl	output of the closed-loop system
θ_RF	RF signal phase
...	

Chapter 2

$a(t)$	noise process
$b(t)$	noise process
$c(t)$	noise process
$g(\tau)$	step response
ℓ	heat conducting rod length
$x(t)$	noise process
$y(t)$	noise process
$A(jf)$	noise process, $A(jf) = \mathcal{F}\{a(t)\}$
$B(jf)$	noise process, $B(jf) = \mathcal{F}\{b(t)\}$
$C(jf)$	noise process, $C(jf) = \mathcal{F}\{c(t)\}$
C_h	heatsink thermal conductivity to ambient
C_p	TEC thermal conductivity
C_RT	thermistor resistance to temperature conversion factor
$C_{\mathrm{T}\lambda}$	temperature to wavelength conversion factor
C_VR	voltage to thermistor resistance conversion factor
G_m	amplitude gain of mixer signal amplifier
G_p	proportional amplitude gain
G_stat	open loop static amplitude gain
I_TEC	TEC drive current
Q_1	heat produced by thermal load
Q_max	maximum heat transfer
R_p	TEC resistance
R_TE	thermistor resistance

T_3	ambient temperature
$X(jf)$	noise process, $X(jf) = \mathcal{F}\{x(t)\}$
$Y(jf)$	noise process, $Y(jf) = \mathcal{F}\{y(t)\}$
α	thermal diffusivity
θ	characteristic timescale parameter of the bandpass filter, Eq. (2.2)
Π	Peltier constant
τ	characteristic timescale parameter of the bandpass filter, Eq. (2.2)
τ_{d}	derivative time
τ_{i}	integral time
τ_{DL}	delay time of the delay line
τ_{r}	delay time produced by heat transfer through a rod
...	

Chapter 3

$\mathcal{B}$	slowly-varying amplitude
C_ν	voltage-to-frequency-noise conversion factor
C_ψ	frequency-noise-to-phase noise conversion factor
D_a	diffusion constant
$J_{\mathrm{c1}}(x)$	first order Bessel cardinal function of the first kind
$K(\nu)$	optical power transfer function
P_{o}	output power of amplifier caused by RIN, thermal noise, and shot noise
$R(\tau)$	autocorrelation function
ν	optical frequency
τ_{D}	differential delay of the asymmetric MZ interferometer
$\Delta\lvert\Psi_n\rvert^2$	n spurious peak height relatively to the phase noise floor
Ψ_{floor}	phase noise floor
...	

Chapter 4

f_{o}	offset frequency
$\ell_{\tau_{\mathrm{m}}}$	loss in the delay element τ_{m}
CS	carrier suppression factor
$\mathcal{F}_{\mathrm{ea}}$	noise figure of error amplifier
NS	noise suppression factor
P_{in}	input power
$P_{\mathrm{in}}^{\mathrm{ea}}$	input power of error amplifier
$S\varphi^{\mathrm{ea}(1Hz)}$	flicker phase noise of the error amplifier at 1 Hz
$S\varphi^{\mathrm{pa}}$	phase noise of the power amplifier
ϵ	amplitude mismatch
η_3, η_4	voltage coupling coefficients of couplers CP3 and CP4
θ	auxiliary variable

ϑ	argument of the filter transfer function $\rho(\omega)e^{j\vartheta(\omega)}$
ρ	modulus of the filter transfer function $\rho(\omega)e^{j\vartheta(\omega)}$
φ	phase error
χ	dissonance
...	

...

Introduction

Oscillations are almost ubiquitous in the Universe as they are found in many, if not in all, physical systems, every part of substance. They are used as a reference to measure time, as a carrier to transfer information and energy. The oscillator can be defined as a system that produces oscillations. Some examples of oscillators are the pendulum, the trumpet, the electronic generator, the quantum generator (laser), and the atom to mention a few. And the simplest, most used model of an oscillator is a harmonic oscillator. It is a physical system that is bound to a position of stable equilibrium by a restoring force proportional to the linear displacement from this position. It is widely used in various engineering systems. Usually it is expected that a real harmonic oscillator is as closer, to an ideal one as possible. But an ideal is not achievable and progress requires higher performances from engineering systems. That is why the task of improving stability of real oscillators is always actual.

There are several types and principles of sine wave (harmonic) oscillators in electronics. A particular type in use depends on frequency region because different principles better work in frequency regions they are developed for. As a result of increasing information traffic volumes, modern telecommunication, radar, signal processing systems go to the X – V bands (tens of GigaHertz). At present among other types of oscillators, optoelectronic oscillators (OEO) manifest better stability and flexibility in this range.

The optoelectronic oscillator consists of a laser, a high speed optical intensity modulator, a long optical-fiber delay-line, a fast photodetector, a mode selection microwave filter, and an amplifier. The modulator, the delay line, the photodetector, the filter, and the amplifier form a closed loop. The laser produces a carrier for optical part or pump energy to the loop. It is possible to have such oscillator functioning without amplifier inside the loop [1]. Stability or spectral purity of oscillations depends on energy storage time of oscillator circuit. The optical fiber delay line determines the loop length or the energy storage time and therefore determines the quality factor of the circuit. The selection microwave filter selects a mode of oscillation. As there is an optical part and a microwave part, there is an optical and a microwave output, which is also a practical advantage, depending on the possible application of the oscillator.

An electronic oscillator phase stabilization system based on a fiber-optic delay line was presented in 1991 [2]. Then a configuration, consisting of an electro-optical modulator that

is fed back with a signal from the detected light at its output, was studied by a number of investigators interested in the nonlinear dynamics [3, 4, 5, 6]. The use of this configuration as a possible oscillator was first suggested by Neyer and Voges [7]. The interest of their investigations was, however, primarily focused on the nonlinear regime and the chaotic dynamics of the oscillator. But Yao and Maleki focused in their research on the stable oscillation dynamics and the noise properties of the oscillator [8]. The first OEO was demonstrated by them in 1994 [9]. Then a number of researchers extensively studied oscillator of this type [10, 11, 12]. Other types of optical energy storage components, such as fiber Fabry-Perot resonators [13], fiber ring resonators [14], and optical micro-disk resonators [15, 16, 17, 18] were proposed to use instead of an optical fiber delay line.

In this work, investigations are focused on the OEO architecture containing an optical fiber delay line and on its phase noise properties.

This thesis is organized in four chapters. Chapter I contains some theory and principles relevant to an electronic delay line oscillator. Chapter II considers the use of optical fiber in such oscillator that makes it an optoelectronic delay-line oscillator due to the presence of optical and electronic parts. It also considers a phase noise measurement bench built with the use of optical fiber. Chapter III provides some equations and experiments that allow estimating phase noise of an OEO. Chapter IV contains some architectures and methods allowing to improve OEO phase noise performance, which were proposed after analysis, considerations and estimations of the OEO phase noise.

Chapter 1

Theory and principles of delay line oscillators

In this chapter, basic theory and principles for representing physical processes in oscillators and development of delay line oscillators are described. Theoretical developments on oscillators in general are partly applicable to delay line oscillators, as their main difference consists in the use of a delay line for defining and stabilizing oscillation frequency. The presence of delay line requires however special issues, mainly when considering oscillator noises. We will first concentrate on applicable theory and principles for oscillators in general, and then particular issues concerned by delay line oscillator will be considered.

1.1 The oscillator

An electronic oscillator converts direct current (DC) to alternating current (AC) or, in general, redistributes energy from one spectral range to others. It is inherently nonlinear. If it were linear, oscillation amplitude would grow infinitely in time. Therefore it is often divided in two parts, the linear, usually passive, circuit and the nonlinear, usually active, device. Then all the knowledge on linear phenomena can be applied to consider the linear part. The nonlinear part can be approximated or linearized depending on phenomena under study. More exact models require nonlinear differential equations.

The most used representation of an electronic oscillator is a feedback loop consisting of an amplifier and a positive feedback circuit. The basic form of a feedback oscillator is shown as a block diagram in Fig. 1.1.

The input V_{in} is used to set the initial conditions from which oscillation starts, and to introduce the equivalent noise of the loop components. Since amplifier gain G is considered as frequency independent, the feedback circuit is used to select oscillation frequency. In

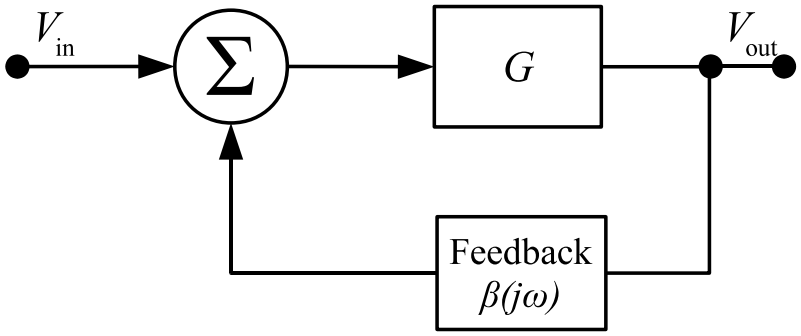

Figure 1.1: Block diagram of a feedback oscillator.

cases of harmonic oscillators, the feedback circuit frequency response $|\beta(j\omega)|$ has a sharp peak at $\omega = \omega_0$.

We will also often use the Laplace transform representation of network functions of linear circuits. Therefore the complex variable $s = \sigma + j\omega$ will indicate the use of this transform. In fact, the Fourier and Laplace transforms are closely related and passage from one formalism to another is often done by simple change of variables.

Oscillation starts from noise or from the switch-on transient. So the system should be unstable in its initial steady state.

The system transfer function of most systems can be represented or approximated as a rational function of the form

$$H(s) = \frac{b(s)}{a(s)}, \tag{1.1}$$

where $a(s)$ and $b(s)$ are polynomials.

The system (1.1) is stable if it has no poles in the right half plane (RHP) [19]. The equation

$$a(s) = 0, \tag{1.2}$$

is called the characteristic equation. The system is stable if the characteristic equation does not have any roots with positive real parts.

The transfer function of the system in Fig. 1.1 is

$$H(s) = \frac{G}{1 - G\beta(s)}. \tag{1.3}$$

So, the characteristic equation of the system is

$$1 - G\beta(s) = 0. \tag{1.4}$$

Instead of resolving the characteristic equation, the Nyquist criterion is often used to evaluate system stability. It is based on Nyquist plot that is a plot of real and imaginary

parts of open loop transfer function for $0 \leq \omega \leq \infty$ (see Fig. 1.2). It is formulated in the following way [19]. When the loop transfer function does not have poles in the right half plane, the condition for stability is that the critical point -1 is to the left of the Nyquist curve when it is traversed for increasing ω. The Nyquist plot also indicates what should be done to move the curve from the critical point and increase the stability of system. The first curve intersection with negative part of real axis gives the gain margin $-1/g_{\mathrm{m}}$. It shows how much the loop gain can be increased before it reaches the critical point. The phase margin φ_{m} shows the phase lag required to reach the critical point. Stability margin s_{m} shows the shortest distance from the curve to the critical point.

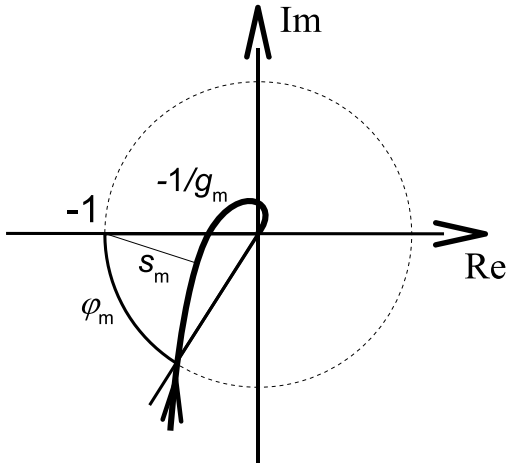

Figure 1.2: The Nyquist plot.

The open loop transfer function of the system $G\beta(s)$ does not have any pole on the right hand plane because the open loop is formed of an amplifier and a passive circuit. Therefore the system (Fig. 1.1) is unstable and oscillations can start if the critical point -1 is to the right of the Nyquist plot.

In "simple" cases [20], the condition for the oscillation to increase as defined by Nyquist criterion, can be reduced to the Barkhausen condition: the open loop transfer function should be more than one $|G\beta(j\omega)| > 1$ and $\arg G\beta(j\omega) = 0\,[\mathrm{mod}\,2\pi]$ at $\omega = \omega_0$.

The Nyquist contour is "simple" if it has the following properties [20]:

- It turns clockwise with ω.
- It begins and ends in the origin (a bandpass filter has this property).
- It crosses the real axis only once for positive ω. If it crosses the real axis more than once, it should return to the origin (or far to the right from $-1 + j0$) between the "resonance" crossings.

In the next section we will see that our case is the "simple" one and we can use the Barkhausen condition for oscillation to grow.

As amplitude approaches the determined level, loop gain should decrease to stop further grow of amplitude.

As a condition for stationary oscillation, the Barkhausen condition [21] is often used

$$G\beta(j\omega) = 1, \tag{1.5}$$

or

$$|G\beta(j\omega)| = 1, \tag{1.6}$$
$$\arg G\beta(j\omega) = 0 \bmod 2\pi. \tag{1.7}$$

1.2 A delay line oscillator

In a delay line oscillator, a delay line (with delay time τ_d) is used as a part of feedback circuit, that is $\beta_\mathrm{d}(s) = e^{-s\tau_\mathrm{d}}$. It determines oscillation frequency by the phase relation (1.7). In this case, multiple oscillation modes that are determined by the following equation are possible

$$\omega_l \tau_\mathrm{d} = 2\pi\, l, \text{ integer } l. \tag{1.8}$$

Therefore a mode selection (narrow passband) filter with the central frequency equal to the desired mode $l = m$ frequency $\omega_m = \frac{2\pi}{\tau_\mathrm{d}} m$ should be also included in the feedback circuit. A resonator type filter is a good choice because it has the transfer function with a non-flat maximum and allows to create the Barkhausen condition only for one mode without necessity of very high quality factor Q. Its transfer function can be defined as follows

$$\beta_\mathrm{f}(s) = \frac{\omega_m}{Q} \frac{s}{s^2 + \frac{\omega_m}{Q} s + \omega_m^2}. \tag{1.9}$$

A delay line can define stability of the system if it determines the frequency of the system. Other components, primarily the filter, have minor contribution. That is [21]

$$\frac{d}{d\omega} \arg \beta_\mathrm{d}(j\omega) \gg \frac{d}{d\omega} \arg \beta_\mathrm{f}(j\omega) \qquad \text{at } \omega = \omega_m, \tag{1.10}$$

because the higher the phase slope the less frequency deviations can be sustained in the system. Equation (1.10) is equivalent to

$$\tau_\mathrm{d} \gg \tau_\mathrm{f}, \tag{1.11}$$

where τ_{f} is the filter group delay

$$\tau_{\mathrm{f}} = \frac{2Q}{\omega_m}. \tag{1.12}$$

As a consequence of the condition (1.11), filter bandwidth contains several modes ω_l. Therefore it is necessary to consider positions of system poles to see possible oscillating conditions. The transfer function of the open loop $G\beta(s) = G\beta_{\mathrm{d}}(s)\beta_{\mathrm{f}}(s)$ is

$$\beta(s) = \frac{\omega_m}{Q} \frac{G\, s\, e^{-s\tau_{\mathrm{d}}}}{s^2 + \frac{\omega_m}{Q} s + \omega_m^2}. \tag{1.13}$$

And the system characteristic equation is

$$1 - \frac{\omega_m}{Q} \frac{G\, s\, e^{-s\tau_{\mathrm{d}}}}{s^2 + \frac{\omega_m}{Q} s + \omega_m^2} = 0. \tag{1.14}$$

Solution of this characteristic equation is well described in Ref. [21]. The system poles positions are illustrated in Fig. 1.3.

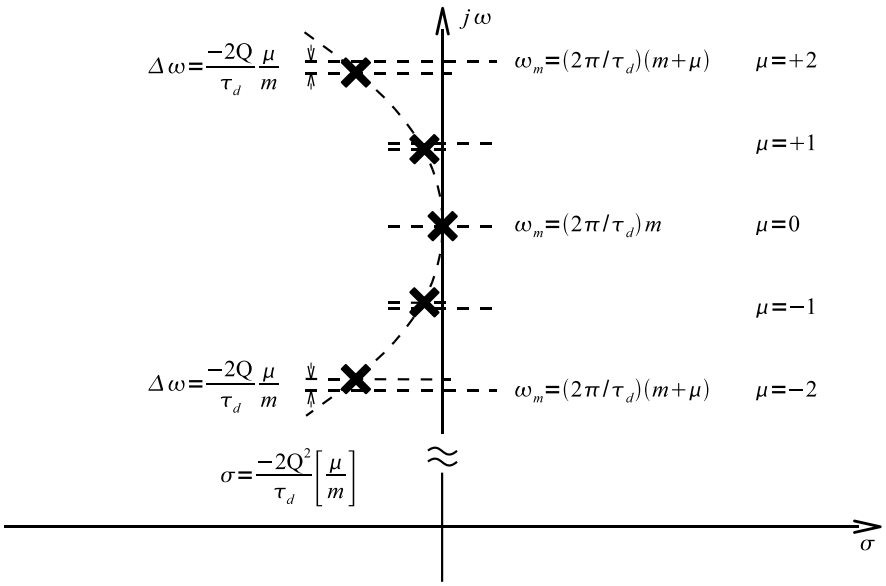

Figure 1.3: Symmetric positions of the poles of the transfer function $H(s)$. $H(s)$ describes the delay-line oscillator with a resonator as the mode selection filter.

The possible positions of poles with respect to ω_m are as follows:

1. The mth pole created by the delay line exactly corresponds to ω_m as shown in Fig. 1.3.

2. The mth pole created by the delay line shifted in relation to ω_m as shown in Fig. 1.4.

3. The mth and $(m+1)$th or $(m-1)$th poles created by the delay line are shifted so that they both have equal position relating $j\omega$ axis as shown in Fig. 1.5.

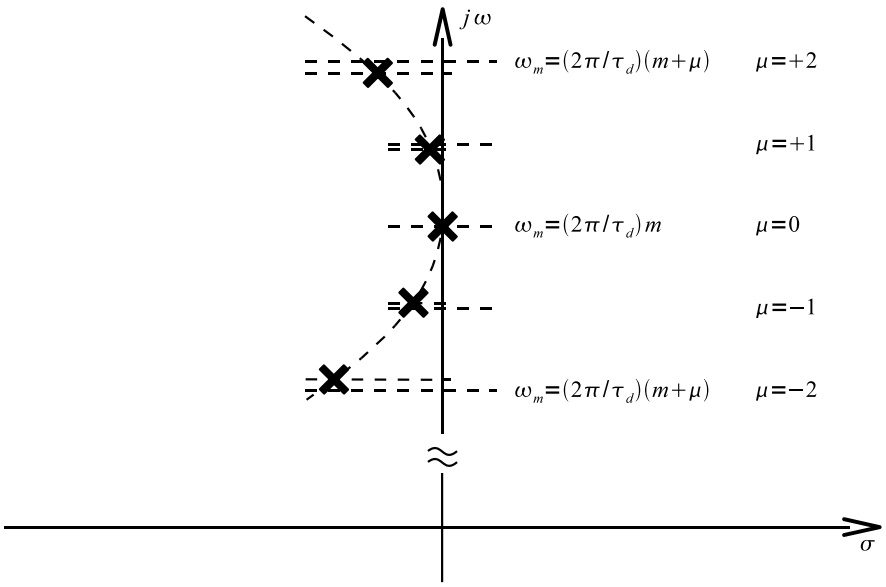

Figure 1.4: Asymmetric positions of poles of transfer function $H(s)$ of the delay-line oscillator with a resonator as the mode selection filter.

The first case is optimal amongst others. The second and third cases produce additional instabilities. So it is necessary to tune poles positions the have the optimal positions. The tuning methods will be described further in the Section 2.1.

1.3 Stochastic nonlinear delay differential equations for delay line oscillators

In previous sections, we considered the description of oscillator using deterministic linear equations. It is an approximative description of oscillator processes, which is nevertheless very helpful for understanding relatively simple processes. But to understand oscillator more deeply, a more complex model taking into account other physical processes is necessary. When tackling the problem of high spectral purity of oscillations, we often deal with stochastic processes. For example, the phase dynamics can be represented as a Brownian motion [22] or as a diffusion [23]. We use the phase diffusion approach in our work, according to which the phase of an oscillator undergoes a diffusion process, similar to a one-dimensional Brownian motion because of small perturbations since it can not be stabilized to a given value. Therefore stochastic description should be present in

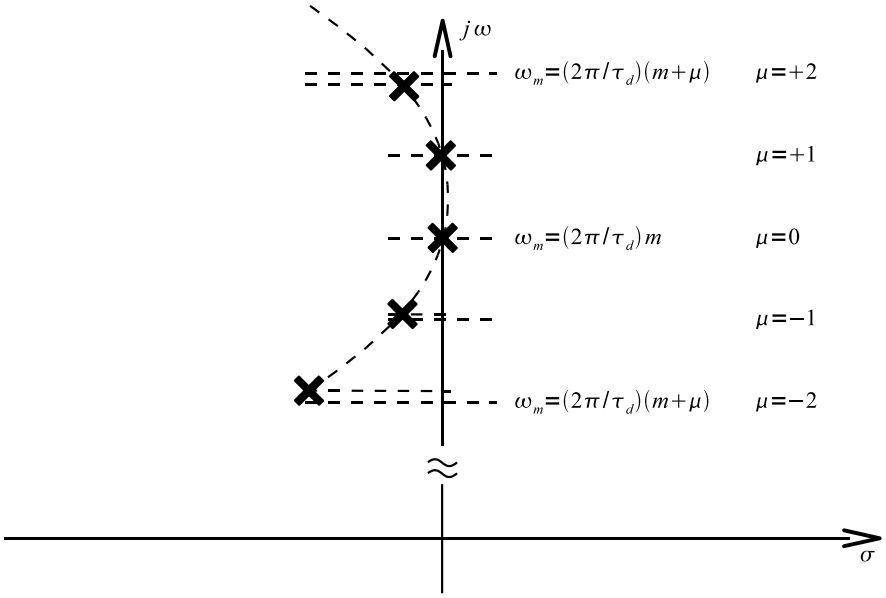

Figure 1.5: Symmetric positions of poles of transfer function $H(s)$ of the delay-line oscillator with a resonator as the mode selection filter with two poles on the imaginary axis.

the oscillator equation. As it was mentioned earlier, the oscillator is inherently nonlinear. Therefore a nonlinear term describing nonlinear elements of the oscillator should be included in the equation. A stochastic nonlinear delay differential equation is a relevant tool to describe a delay line oscillator. Since the resonator filter is included in the loop, it is relevant to use the second-order differential equation of an LCR circuit, including a nonlinear term and a time delay τ_d

$$\frac{\mathrm{d}^2x(t)}{\mathrm{d}t^2} + \frac{\omega_\mathrm{r}}{Q}\frac{\mathrm{d}x(t)}{\mathrm{d}t} + \omega_\mathrm{r}^2 x(t) + u(x(t-\tau_\mathrm{d})) = 0, \tag{1.15}$$

where $x(t)$ is a system parameter (voltage, current etc.), ω_r is the resonator central frequency, Q is the quality factor of the resonator, $u(x(t-\tau_\mathrm{d}))$ is the function describing the nonlinear element and the time delay.

In order to include noise effects in this equation, we will consider two main noise contributions.

The first contribution is an additive noise, corresponding to random environmental and internal fluctuations which are uncorrelated from the eventual existence of a microwave signal. The effect of this noise can be accounted for by addition of a Langevin forcing term in the right-hand side of Eq. (1.15). This additive noise can be assumed to be spectrally white, and since we are interested by its intensity around the carrier frequency ω_0, it can be explicitly written as

$$\xi_\mathrm{a}(t) = \frac{1}{2}\zeta_\mathrm{a}(t)e^{j\omega_0 t} + \frac{1}{2}\zeta_\mathrm{a}^*(t)e^{-j\omega_0 t}\,, \tag{1.16}$$

where $\zeta_a(t)$ is a complex Gaussian white noise, which correlation is $\langle \zeta_a(t)\zeta_a^*(t')\rangle = 4D_a\delta(t-t')$, so that the corresponding power density spectrum is $|\tilde{\xi}_a(\omega)|^2 = 2D_a$. The parameter D_a is referenced as the diffusion constant. Some authors considered possibilities to use nonlinear coupling of oscillator present state with its delayed state to decrease the phase diffusion [24, 25].

The second contribution is a multiplicative noise due to a noisy loop gain. We denote the normalized gain parameter γ. If all the parameters of the system are noisy, then the gain γ may be replaced by $\gamma + \delta\gamma(t)$, where $\delta\gamma(t)$ is the overall gain fluctuation. We therefore introduce the dimensionless multiplicative noise

$$\eta_m(t) = \frac{\delta\gamma(t)}{\gamma}, \tag{1.17}$$

which is in fact the relative gain fluctuation. Usually we have $\eta_m(t) \ll 1$. This noise is in general spectrally complex, as it is the sum of very different noise contributions (noise from the photodetector, from the amplifier, from CW energy source, etc.).

Thus introducing the two noise terms, Eq. (1.15) becomes

$$\frac{d^2x(t)}{dt^2} + \frac{\omega_r}{Q}\frac{dx(t)}{dt} + \omega_r^2 x(t) + (1+\eta_m(t))u(x(t-\tau_d)) = \xi_a(t). \tag{1.18}$$

We will use this equation in Chapter 3 to derive relations for noise evaluation in an OEO.

1.4 Bode's integral theorem, application to oscillators

Oscillator stability can be considered using the Bode's integral theorem. The Bode's integral is used for analysis of stable feedback systems [19]. It holds that

$$\int_0^\infty \ln|\varepsilon(i\omega)|\,\mathrm{d}\omega = 0, \tag{1.19}$$

where $\varepsilon(i\omega)$ is the system sensitivity function. It says that if sensitivity is reduced for one frequency it increases at another frequency. As it was developed for stable systems it can not be directly applied for unstable systems, such as oscillators. But experience shows that there is similar behavior of oscillators toward disturbances. Using this concept emphasizes that while considering the oscillator noise, we should distinguish sources of noise (noise spectra of disturbances) and the sensitivity of oscillator to the disturbances. Their interaction gives us the noise profile of oscillator close to the carrier frequency. So, it is important to see if we can apply a similar theorem to oscillators.

We define a sensitivity function of oscillator (see Fig. 1.1) similar to the one in Ref. [19]. Let $V_{ol} = GV_{in}$ be the output of the open-loop system and $V_{cl} = GV_{in}/(1 - G\beta(s))$ the

output of the closed-loop system. Then the sensitivity function of the feedback oscillator is

$$\varepsilon(s) = \frac{V_{\text{cl}}}{V_{\text{ol}}} = \frac{1}{1 - G\beta(s)}, \tag{1.20}$$

where G is the amplifier gain, $\beta(s)$ is the feedback transfer function.

Let's follow a proof [26] of the Bode integral theorem to see how we can use it for oscillator analysis.

Let $l(s)$ be a proper real, rational function of relative degree n_{r} (difference between number of poles and zeros of a function). Let's define

$$g(s) \triangleq \frac{1}{1 + l(s)}, \tag{1.21}$$

and assume that $g(s)$ has neither poles nor zeros in the closed right half-plane (RHP). Then

$$\int_0^\infty \ln|g(j\omega)|\mathrm{d}\omega = \begin{cases} 0 & \text{for } n_{\text{r}} > 1 \\ -\kappa\frac{\pi}{2} & \text{for } n_{\text{r}} = 1 \end{cases} \qquad \text{where } \kappa \triangleq \lim_{s\to\infty} s\, l(s). \tag{1.22}$$

Proof

Because $\ln g(s)$ is analytic in the closed RHP,

$$\oint_C \ln g(s)\mathrm{d}s = 0, \tag{1.23}$$

where $C = C_j \cup C_\infty$ is the contour defined in Fig. 1.6.

Then

$$\oint_C \ln g(s)\mathrm{d}s = j\int_{-\infty}^{\infty} \ln g(j\omega)\mathrm{d}\omega - \int_{C_\infty} \ln(1 + l(s))\mathrm{d}s. \tag{1.24}$$

For the first integral on the right-hand side, we use the conjugate symmetry of $g(s)$ ($g(s^*) = (g(s))^*$) to obtain

$$\int_{-\infty}^{\infty} \ln g(j\omega)\mathrm{d}\omega = 2\int_0^\infty \ln|g(j\omega)|\mathrm{d}\omega. \tag{1.25}$$

For the second integral, we notice that, on C_∞, $l(s)$ can be approximated by

$$\frac{a}{s^{n_{\text{r}}}}, \tag{1.26}$$

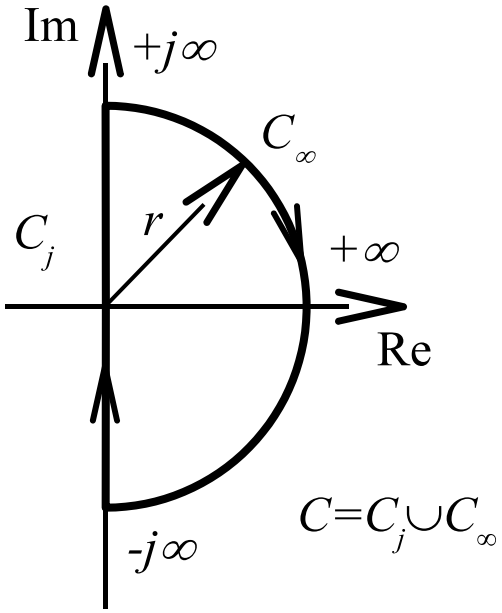

Figure 1.6: Contour definition.

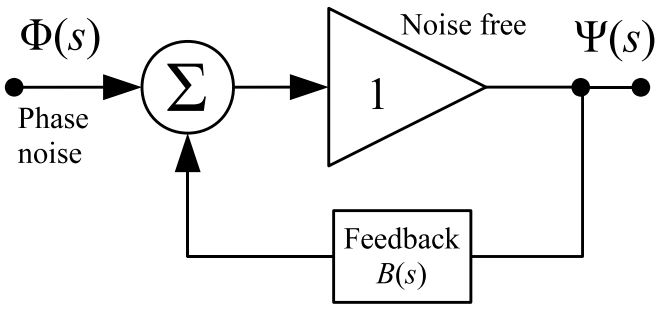

Figure 1.7: Phase loop block diagram [21].

where $a = \kappa$ for $n_\mathrm{r} = 1$.

We can define $l(s) = -G\beta(s)$ for our case as follows

$$l(s) = \frac{\omega_m}{Q} \frac{(-G)\, s\, e^{-s\tau_\mathrm{d}}}{s^2 + \frac{\omega_m}{Q} s + \omega_m^2}, \tag{1.27}$$

where Q is the RF filter quality factor, ω_m is the central frequency of the RF filter, $\tau_\mathrm{d} > 0$ is the delay time. It has $n_\mathrm{r} = 1$.

The sensitivity function of the oscillator (1.20) has a pole at $j\omega_m$. It prevents us from applying the Bode integral theorem directly. But we can use an infinitesimal circular indentation in C, constructed so as to leave the singularity outside and therefore apply the theorem to analysis of the oscillator.

Let's consider the phase-perturbation transfer function of a feedback oscillator as introduced in Ref. [21]. Feedback oscillator phase noise model can be presented as in Fig. 1.7.

$$\mathrm{H}(s) = \frac{\Psi(s)}{\Phi(s)} = \frac{1}{1 - B(s)}. \tag{1.28}$$

Since the feedback contains a delay line and a resonator

$$B(s) = e^{-s\tau_\mathrm{d}} \frac{1}{1 + s\tau_\mathrm{f}}. \tag{1.29}$$

Thus the sensitivity function for phase perturbations of the feedback oscillator

$$\varepsilon_\mathrm{phase}(s) \quad = \quad \frac{1}{1 - \frac{e^{-s\tau_\mathrm{d}}}{1+s\tau_\mathrm{f}}}. \tag{1.30}$$

It has a pole at $s = 0$ and the relative degree of the function $l(s)$, $n_\mathrm{r} = 1$. So, the Bode integral theorem can be applied with the infinitesimal circular indentation in $s = 0$.

So, we can apply the Bode integral theorem to the amplitude and phase sensitivity functions of the feedback oscillator. Therefore if we reduce oscillator noise sensitivity for one frequency, it increases at other frequencies. We are mostly interested in the cases where most of the sensitivity is concentrated near the oscillation frequency (in fact it is usually the case). But there are sensitivity peaks of the delay line oscillator near the ω_l frequencies, and when we suppress them we should see an increase of the sensitivity around them.

As we mentioned, we should distinguish between methods for reducing noise sources in the system (laser noise, amplifier noise, photodiode noise) and methods for reducing the system sensitivity to the noises (multiple loops, RF filter selectivity). Further in this work we will consider the noise sources and methods for reducing oscillator sensitivity to the noises.

1.5 Oscillator noise characterization

An ideal oscillator would generate a pure sine wave. In the frequency domain, this would be represented as a pair of delta functions (positive and negative conjugates) at the oscillator frequency, i.e., all the signal power is at a single frequency. Random perturbations produce amplitude and phase modulation. That is why all real oscillators have the spectrum, which is spread in some degree. The phase noise components spread the power of the delta functions to adjacent frequencies, resulting in sidebands.

A relatively simple model that was introduced in the early 1960's and was widely accepted [27, 28] is

$$V(t) = (V_0 + \alpha(t)) \sin[2\pi\nu_0 + \varphi(t)], \tag{1.31}$$

where $\varphi(t)$ is a random process denoting phase noise, V_0 and ν_0 are the nominal amplitude and frequency respectively; and the amplitude noise $\alpha(t)$ can usually be neglected. Such a quasi sinusoidal signal has an instantaneous frequency

$$\nu(t) = \frac{1}{2\pi}\frac{\mathrm{d}}{\mathrm{d}t}(2\pi\nu_0 t + \varphi(t)) = \nu_0 + \frac{1}{2\pi}\frac{\mathrm{d}\varphi(t)}{\mathrm{d}t}. \tag{1.32}$$

Frequency noise is the random process defined by

$$\Delta\nu(t) \equiv \nu(t) - \nu_0 = \frac{1}{2\pi}\frac{\mathrm{d}\varphi(t)}{\mathrm{d}t}. \tag{1.33}$$

Very often normalized dimensionless frequency fluctuations are introduced

$$y(t) = \frac{\Delta\nu(t)}{\nu_0}. \tag{1.34}$$

It can be used for comparison of oscillators at different nominal frequencies.

Two kinds of parameters are most often used to characterize the oscillator spectral purity:

- spectral densities of phase and frequency fluctuations in the Fourier frequency domain;
- variances (or standard deviation) of the averaged frequency fluctuations in the time domain.

In the Fourier frequency domain, phase and frequency fluctuations are characterized by respective one-sided spectral densities $S_\varphi(f)$ and $S_{\Delta\nu}(f)$. They have a simple relation

$$S_{\Delta\nu}(f) = f^2 S_\varphi(f)\,, \tag{1.35}$$

which is caused by the time derivative between $\varphi(t)$ and $\Delta\nu(t)$. The spectral density $S_y(f)$ is also widely used and related to $S_\varphi(f)$ and $S_{\Delta\nu}(f)$ by

$$S_y(f) = \frac{1}{\nu_0^2} S_{\Delta\nu}(f) = \frac{f^2}{\nu_0^2} S_\varphi(f)\,. \tag{1.36}$$

Time domain characterization of frequency stability is also widely used since it directly shows frequency stability on a time interval. The most used variances are the Allan variance and the modified Allan variance. They are related to spectral densities by integrals and transfer functions but some information is, however, lost. The Allan variances are useful for measuring oscillator stability by devices specially developed for this purpose. They can be rather easily calculated from spectral densities when it is easy to decompose

the phase or frequency noise spectral density to components of different slopes. It should be noted that some slopes can be characterized by only one value of Allan variance and others require also to note the interval between samples τ. If there are spurs in the density spectrum then the variance calculation becomes rather difficult. For stationary Gaussian random processes, the spectral density contains maximum information about the process. The spectral density also gives more information about other random processes than the Allan variance. It gives more insight in processes occurring in an oscillator. Further in this work, we will use mainly the phase noise spectral densities to characterize oscillator performance.

Phase noise power spectral density (PSD) is typically expressed in units of dBc/Hz (in industrial applications) or dBrad^2/Hz (in scientific applications) at various offsets from the carrier frequency. Phase noise can be measured and expressed as single sideband or double sideband values. Manufacturers and engineers prefer the quantity $\mathscr{L}(f)$, which is by definition

$$\mathscr{L}(f) = \frac{1}{2} S_\varphi(f), \tag{1.37}$$

given in dBc/Hz.

Originally it was defined as

$$\mathscr{L}(f) = \frac{\text{one-sideband noise power in 1 Hz bandwidth}}{\text{carrier power}}, \tag{1.38}$$

but this definition gives significant discrepancies between $\mathscr{L}(f)$ and $S_\varphi(f)$ in the presence of large noise.

It has been shown from both theoretical considerations and experimental measurements, that the spectral densities due to noise of oscillators can be represented by the power law model where the spectral densities vary as a power of f [27, 28, 29]. More specifically, $S_\varphi(f)$ can be written as the sum:

$$S_\varphi(f) = \sum_{i \le 0}^{0} b_i f^i \,. \tag{1.39}$$

Frequently encountered phase noise processes [21] are presented in Table 1.1.

Low frequency fluctuations of power spectral density inversely proportional to frequency are observed in various physical, technical, biological, and economic systems [30]. This peculiar phenomenon is called $1/f$-noise or flicker noise. Flicker noise can be considered as one of the major limiting factors for frequency stability because it is ubiquitous and seems to be a general fluctuation phenomenon mostly connected with collective motion of particles ([31], p. 1). Noises of other types are easier to eliminate. For example, $1/f^5$ noises of thermal fluctuation can be decreased by thermal stabilization.

law	slope	noise process
$b_0 f^0$	0	white phase noise
$b_{-1} f^{-1}$	-1	flicker phase noise
$b_{-2} f^{-2}$	-2	white frequency noise (or random-walk of phase)
$b_{-3} f^{-3}$	-3	flicker frequency noise
$b_{-4} f^{-4}$	-4	random-walk of frequency

Table 1.1: Noise processes.

The terms of the power law of different power are inherent to different processes and are a sort of signatures of the processes. Therefore they allow to see what happens in oscillator and are widely used.

The Allan variance can be determined from the phase noise density spectrum using [27]

$$\sigma_y^2(\tau) = \int_0^\infty S_y(f) \left|H_\mathrm{A}(jf)\right|^2 \mathrm{d}f \,, \tag{1.40}$$

where

$$\left|H_\mathrm{A}(jf)\right|^2 = 2\frac{\sin(\pi\tau f)^4}{(\pi\tau f)^2} \,. \tag{1.41}$$

This general equation was converted in rather simple formulas for different terms of the power-law model ([31], p. 79). But the general equation should be applied for PSD of more complex form that doesn't conform to the power law.

Also we will use the time jitter characterization since it better illustrates the influence of phase noise spectrum profile and particularly the spurs on phase stability and is easier to calculate than Allan variance. The time jitter can be calculated similar to [32] using the following equation:

$$\sigma = \frac{1}{2\pi\nu_0}\sqrt{\int_{f_\mathrm{min}}^{f_\mathrm{max}} S_\varphi(f) df} \,. \tag{1.42}$$

This expression is based on the one for the integrated phase noise [33] and is more convenient for calculation based on the phase noise PSD.

1.6 State-of-the-art microwave oscillators

Microwave oscillators started with vacuum tubes in 1940. Their theory and technology have been advancing for long time. Their varieties in the form of klystrons, reflex

klystrons, and magnetrons in microwave generation applications have so good performance that they are in use up to the present time. By the late 1970s transistor dielectric resonator oscillators could provide clean 10 mW of power at X-band in about one cubic inch of volume. More recently, surface-mount hybrid oscillators and complete Monolithic Millimetre-wave Integrated Circuits (MMIC) solutions are able to provide necessary performance occupying much less volume and at a fraction of the cost. The requirement of high spectral purity led to other approaches also. At present time, the most advanced in terms of the spectral purity among them are based on using:

- a coaxial resonator with frequency multiplication;
- a dielectric resonator with frequency multiplication;
- a crystal resonator with frequency multiplication;
- a sapphire whispering gallery mode resonator;
- an optoelectronic oscillator using a very long delay line;
- an optoelectronic oscillator using a high Q optical resonator.

Examples of these oscillators and their phase noise levels (dBc/Hz) for output frequency of about 10 GHz are presented in Table 1.2. These data are taken from the device datasheets, which can be found on websites of the companies.

Company	Model	Type	10 Hz	100 Hz	1 kHz	10 kHz	Ref.
Miteq	DLCRO15000	coaxial	−60	−79	−109	−118	[34]
Poseidon	DRO-10.4-FR	DRO		−59	−86	−111	[21, 35]
Wenzel	Agate I	OCXO		−82	−107	−127	[36]
Poseidon	Shoebox	WGM SLCO		−114	−142	−162	[37, 35]
OEWaves		OEO	−80	−115	−145	−157	[38]

Table 1.2: Phase noise levels of different microwave oscillators in dBc/Hz.

Frequency multiplication significantly degrades the phase noise level. Therefore oscillators based on this principle do not show best phase noise levels even if they have excellent results for fundamental frequencies.

The OEO oscillator of OEWaves has the best phase noise level in the indicated frequency range. OEOs usually have higher spurious peaks but their output frequencies can be easily tuned without phase noise level degradation. A sapphire loaded cavity oscillator (SLCO) at the whispering gallery mode (WGM) [39] competes with OEO. It has very low spurious peaks. But its frequency is fixed and can be possibly tuned only by temperature in small range.

The phase noise spectrum of OEwaves OEO [38] is shown in Fig. 1.8. It seems that it has some bump at frequencies higher than 10 kHz. Probably it is the trace of spurious

peak. The bump at about 200 Hz can be caused by some problems of measurement or by supply source noise.

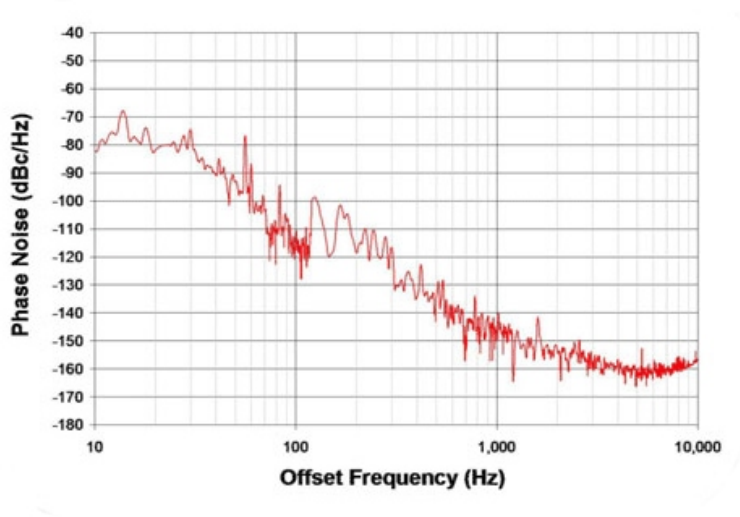

Figure 1.8: OEwaves OEO phase noise spectrum [38].

Recently an OEO without an RF amplifier in the loop was presented [40]. It operated at 1.25 GHz and had improved flicker-noise performance (about -70 dBc/Hz at 10 Hz offset).

The very perspective direction is the use of crystalline whispering-gallery-mode resonators. They can provide Q factor much higher than the optical fiber delay lines can do and they have very small dimensions (from several millimeters to several micrometers). WGM resonators generally exhibit Q in the range from 10^5 in the case of ring structures, to greater than 10^{11} for fluorite toroidal resonators [38]. They can be also used as resonant electro-optical modulators (EOM). Such resonators exhibit optical quality factors in excess of $8 \cdot 10^8$. They require only sub-milliwatt of applied microwave power for deep modulation of light.

1.7 Conclusion

Some basic principles of oscillator functioning and tools for its design and characterization that are applicable for an OEO are considered in this chapter. A possibility to apply the Bode's integral principle, which is used to predict behavior of stable control system with a feedback loop with regard to perturbations, to characterize phase noise sensitivity of an oscillator is discussed. Performances of state-of-the-art microwave oscillators are compared.

The first optoelectronic oscillators comprised an optical fiber as an intrinsic component

– delay line. Due to low loss, an optical fiber is irreplaceable for making long delay lines. In the next chapter, an application of optical fiber as a delay line in oscillators and phase noise measurement is discussed.

Chapter 2

Fiber delay lines for oscillators and phase noise measurement

Optical fiber has advantages over microwave coaxial cable, which enable its use as a long delay line. The main advantage is a very low loss. Typical microwave coaxial cable loss at 5 GHz is about 1 dB/m and it increases with frequency. Optical fiber loss is about 0.2 dB/km in a wide bandwidth. It enables to create delay lines of several kilometers length for tens GHz frequency range, which is almost impossible with a microwave coaxial cable. Optical fiber has a low thermal sensitivity of the delay. Its typical value is 6.85×10^{-6}/K, a factor of 10 better than the sapphire dielectric cavity. These features enable the implementation of high spectral purity oscillators and of high-sensitivity instruments for the measurements of phase noise. In both cases, the optical bandwidth turns into wide-range microwave tunability [41, 42] at virtually no cost in terms of phase noise.

The fiber refraction index has different dispersion for different spectral regions. The presence of dispersion can play negative or positive role for a system performance. For an example of positive role, it allows tuning the delay time through laser wavelength adjustment [43]. But it can also create delay time fluctuation since the laser wavelength fluctuates. The latter adds instability when dealing with an optoelectronic oscillator, and is considered further in this chapter.

2.1 Optoelectronic delay line oscillator

In the basic configuration, the optoelectronic fiber delay line microwave oscillator consists (Fig. 2.1) of a laser, a high speed optical intensity modulator, an optical fiber delay line, a fast photodetector, a mode selection microwave filter, and an amplifier. It has two types of output: optical and microwave [44]. This combination of microwave and optical domains is advantageous because it connects positive properties of optical and

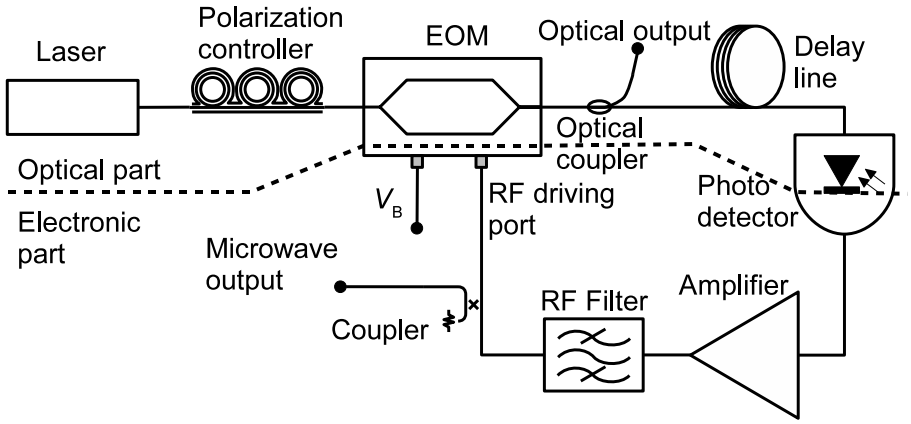

Figure 2.1: OEO basic architecture.

microwave components, with their own methods of physical signal processing. As it was mentioned, optical technology allows creating wide band and long delay line with low thermal sensitivity. The time delay can be finely tuned with adjustment of laser wavelength due to optical fiber dispersion. In their turn, semiconductor lasers allow adjusting laser wavelength through their stabilized temperature. Transformation from optical to microwave signal through the photodiode allows avoiding problems connected with polarization and phase instability of optical beam in the output of the fiber delay line. The microwave components allow more easily implementing mode selection and amplification without adding much of amplitude and phase noise.

Let's analyse the OEO in detail. For practical reasons, we had to use components available off-the-shelf, mainly intended for telecommunications applications. The microwave components limit the frequency range to 4-5 GHz around the central frequency of 10 GHz. The OEO is designed for low phase noise that includes high stability of the delay line also. The oscillation frequency of 10 GHz was chosen since it is a typical frequency for this class of oscillators.

We used continuous-wave semiconductor lasers EM4 (1561.83 nm, optical power up to 80 mW, EM4 Inc.) and CQF935 (1546.12 nm, optical power up to 24 mW, JDS Uniphase) since they have different noise and power characteristics and allow to compare their influence on oscillator performance. They are powered and controlled by the Thorlabs laser diode controllers LDC210C (up to 1 A) and LDC202C (up to 200 mA) and the Thorlabs thermoelectric temperature controller TED200C. The region of 1550 nm wavelength is the best choice for the low attenuation of the fiber.

Choosing the intensity-modulation method, we discarded a priori the direct modulation of the laser because the chirp induced while applying modulation, inherently, enhances the phase noise of the microwave signal. Thus, we opted for a Mach-Zehnder (MZ) electro-optic modulator (EOM). Other modulators, for example based on the acousto-optic effect, are not suitable to microwave modulation frequencies. We choose the EOspace $LiNbO_3$ modulator AZ-1K1-12-PFA-SFA having low half-wave voltage ($V\pi \simeq 4$ V at 10 GHz), so

that the maximum modulation is achieved with no more than 50 mW (+17 dBm) microwave power. This choice is important for stability of the half-transparency bias point because the $LiNbO_3$ is highly sensitive to temperature, thus to power and to thermal gradients.

A thermalized 4 km fiber performed a time delay of $\tau_d = 20$ μs on the microwave signal carried by the optical beam (the corresponding free spectral range is $F_{\tau_d} = 1/\tau_d = 50$ kHz and the Q factor is 628320 at 10 GHz). The optical fiber is a Corning SMF-28 wound on a cylinder of 15 cm diameter and 2 cm height. The spool with fiber is enclosed in a 5 mm thick Duralumin cylinder thermally insulated from the environment by 3 cm thick plastic foam. The cylinder is temperature stabilized within a fraction of a milliKelvin with a PID control.

For low noise at microwave frequencies, the photodetector can only be a InGaAs p-i-n diode operated in strong reverse-bias conditions, thus as a photoconductor. Reverse bias is necessary for high speed, as it reduces the junction capacitance. The need for low noise excludes other detectors, like the avalanche diode. In our case, the photodetectors loaded to a resistor are preferable to the (more modern) photodetectors with integrated transconductance amplifier because of the possibility to choose a low flicker external amplifier and higher maximum input optical power, which allows to decrease the necessary amplifier gain. So, we used the InGaAs p-i-n photodiodes DSC40S (Discovery Semiconductors) with a conversion factor $\rho = 0.75$ A/W. A 50 Ω resistor is included in the package (see Fig. 2.2). Connection line impedance is also 50 Ω. Therefore current-to-voltage conversion resistance is $R_{PD} = 25$ Ω.

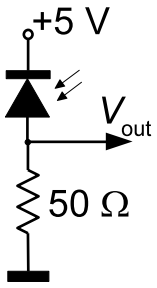

Figure 2.2: DSC40S internal circuit.

A narrow band microwave radio-frequency (RF) filter of central frequency $F_0 = \omega_0/2\pi = 10$ GHz, and -3 dB bandwidth of $\Delta F = \Delta\omega/2\pi = 50$ MHz was used as the mode selection filter.

We used microwave amplifiers AML with gain $G = 22$ dB. They have special architecture to provide low flicker phase noise. Their typical level of flicker phase noise is about -160 dBrad^2/Hz at 10 kHz offset. It is supposed [21] that such amplifier consists of several amplifiers connected in parallel. But this architecture increases the noise figure of the whole amplifier. It is indeed 6 dB, a higher value than the one of other microwave amplifiers.

The optical fiber of 4 km length and the photodiode produce significant reflection of light beam. This can disturb laser functioning and create multiple signal transitions between photodiode and delay line. Therefore it is preferably to include optical isolators between laser and delay line and between delay line and photodiode.

2.2 Mathematical model of OEO

In Section 1.3, we introduced the stochastic nonlinear delay differential equation (1.18) that can well describe the OEO dynamics. But it should be transformed into the equation describing OEO. For this purpose, the function of a nonlinear component is defined for MZ EOM

$$u(t) = \beta \cos^2[x(t - \tau_\mathrm{d}) + \phi], \tag{2.1}$$

where $\beta = \pi\kappa\rho R_\mathrm{PD} P_\mathrm{opt}/2V_{\pi\mathrm{RF}}$ is the normalized loop gain, P_opt is the laser power, $\phi = \pi V_\mathrm{B}/2V_{\pi\mathrm{B}}$ is the Mach-Zehnder offset phase, $x(t)$ is the dimensionless variable $x(t) = \pi V(t)/2V_{\pi\mathrm{RF}}$. All optical and electrical losses are gathered in a single attenuation factor κ. We will not consider the noise terms in this section. So, the dynamics of OEO microwave oscillation can be described as follows [45]

$$x + \tau\frac{dx}{dt} + \frac{1}{\theta}\int_{t_0}^{t} x(s)\mathrm{d}s = \beta \cos^2[x(t - \tau_\mathrm{d}) + \phi], \tag{2.2}$$

where $\tau = 1/\Delta\omega$ and $\theta = \Delta\omega/\omega_0^2$ are the characteristic timescale parameters of the bandpass filter.

Since we are interested by single-mode microwave oscillations, the solution of Eq. (2.2) can be expressed under the form

$$x(t) = \frac{1}{2}\mathcal{A}(t)\, e^{j\omega_0 t} + \frac{1}{2}\mathcal{A}^*(t)\, e^{-j\omega_0 t}\,, \tag{2.3}$$

where $\mathcal{A}(t) = A(t)\, \exp[j\psi(t)]$ is the slowly varying complex amplitude of the microwave $x(t)$. We can simplify significantly the right-hand side term of Eq. (2.2) because the cosine of a sinusoidal function of frequency ω_0 can be expanded as a series of signal harmonics of ω_0. In other words, since $x(t)$ is nearly sinusoidal around ω_0, then the Fourier spectrum of $\cos^2[x(t - \tau_\mathrm{d}) + \phi]$ is sharply distributed around the harmonics of ω_0 according to the relationship $\cos^2 z = [1 + \cos 2z]/2$ and the Jacobi-Anger expansion

$$e^{iz\cos\alpha} = \sum_{n=-\infty}^{+\infty} i^n \mathrm{J_n}(z) e^{jn\alpha}\,, \tag{2.4}$$

where $\mathrm{J_n}$ is the n-th order Bessel function of the first kind. Hence, since the filter of the feedback loop is narrowly resonant around ω_0, it can be demonstrated that discarding all

the spectral components of the signal except the fundamental is an excellent approximation. Equation (2.2) can be rewritten as

$$x + \frac{1}{\Delta\omega}\frac{\mathrm{d}x}{\mathrm{d}t} + \frac{\omega_0^2}{\Delta\omega}\int_{t_0}^{t} x(s)\mathrm{d}s = -\beta \sin 2\phi$$
$$\times \mathrm{J}_1[2|\mathcal{A}(t-\tau_\mathrm{d})|]\,\cos[\omega_0(t-\tau_\mathrm{d}) + \psi(t-\tau_\mathrm{d})]\,. \tag{2.5}$$

The stable oscillation of the OEO is achieved at the Barkhausen condition (1.6). If the open loop gain exceeds 1, the excessive energy goes to harmonics and is eliminated due to the RF filter and other band limited components (e.g. the photodiode). The amplifiers we use in the OEO have −1 dB gain compression at about 17 dBm of output power, but the EOM has much higher nonlinearity. Other components do not manifest significant nonlinearity at the usual operation power. So we can use the EOM modulation characteristic to estimate oscillation amplitude and power at given open loop gain.

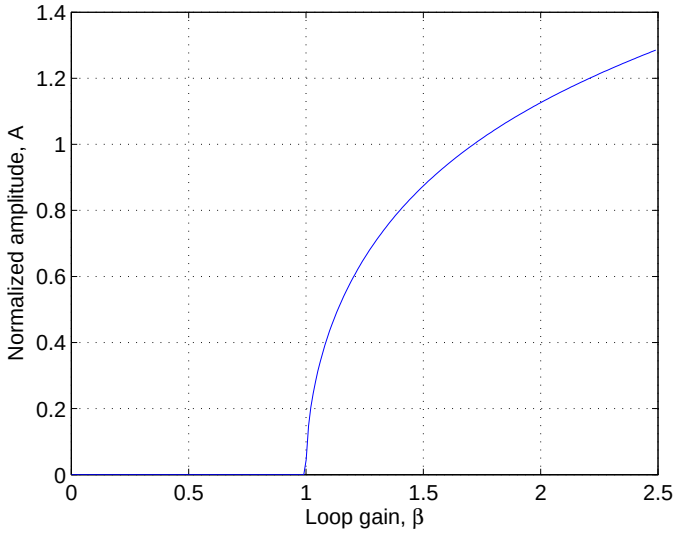

Figure 2.3: Normalized amplitude A vs. loop gain β.

For this purpose, we write the following equation based on Eq. (2.5) in a way similar to the one described in Ref. [45]

$$A = \beta \mathrm{J}_1[2A]\,. \tag{2.6}$$

It assumes $\phi = \pm\pi/4$ [π], which is usual condition for MZ EOM in OEO. Since we are interested in $A \leq 1$, this Bessel function can be represented by the first three terms of its Taylor expansion and this equation becomes

$$\frac{1}{\beta} \simeq 1 - \frac{A^2}{2} + \frac{A^4}{12}\,. \tag{2.7}$$

Resolving this equation for A we get positive solutions meeting the condition $A \leq 1$ as

$$A \simeq \sqrt{3 - \sqrt{12/\beta - 3}}\,. \tag{2.8}$$

This equation is illustrated in Fig. 2.3. As one can see, after the threshold $\beta = 1$, the amplitude quickly grows and then its growth slows down. The amplifier gain compression (17 dBm corresponds to $A \simeq 0.9$) was not taken into account in this equation. It should produce additional slowdown of the amplitude growth.

This equation allows choosing proper open loop gain to achieve desired oscillation power and estimating oscillation power using known parameters of the loop components.

2.3 Phase noise measurement

2.3.1 Phase noise measurement methods

When measuring the phase noise of high spectral purity oscillator, one deals with very low noise components near a strong carrier. This requires measurement methods of high dynamic range. The required dynamic range can only be achieved by suppressing the carrier, which can be done in the following ways:

- convolution methods (high Q filters);
- time domain product methods (using mixers) [46];
- vector difference methods (bridge technique) [47, 48].

For general phase-noise measurement, the time-domain product method is the most appropriate. There are two ways of applying this method: with reference source or with delay line. The first way requires an expensive highly stable and tunable source. When measuring the phase noise of an oscillator of very high stability, a higher stability reference source is required. These problems are not present with a delay line, and the measurement setup time is also smaller. However, with delay line, high sensitivity is only achieved with very long delay line. Of course, the delay line must exhibit suitably high stability and low noise. Again the advantages of optical fiber become crucial.

A basic scheme for phase noise measurement including a delay line is shown in Fig. 2.4 [49].

Delaying the signal $v(t)$ by τ, all time-varying parameters of $v(t)$ are also delayed by τ, thus the phase fluctuation $\psi(t)$ turns into $\psi(t-\tau)$. By virtue of the time-shift theorem, the Fourier transform of $\psi(t-\tau)$ is $e^{-j2\pi\tau f}\Psi(jf)$. This enables the measurement of the oscillator phase noise $\psi(t)$ by observing the difference $\theta(t) = \psi(t) - \psi(t-\tau)$. The double balanced mixer saturated at both the inputs, used as a phase detector [50]. By inspection on Fig. 2.4, it holds that

$$\Theta(jf) = \mathrm{H}(jf)\Psi(jf), \tag{2.9}$$

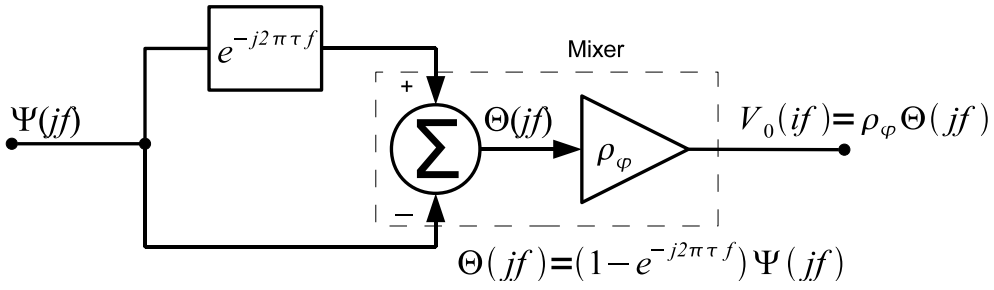

Figure 2.4: A basic scheme of phase noise measurement using a delay line [49].

where $\mathrm{H}(jf) = 1 - e^{-j2\pi\tau f}$, and consequently

$$S_\theta(f) = |\mathrm{H}(jf)|^2 S_\psi(f) \tag{2.10}$$

$$|\mathrm{H}(jf)|^2 = 4\sin^2(\pi f\tau) \tag{2.11}$$

The oscillator phase noise $S_\psi(f)$ is deduced by applying $|\mathrm{H}(jf)|^{-2}$ to the measured output $S_\theta(f)$. In actual measurements it is important to keep the measurement and the use of $|\mathrm{H}(jf)|^2$ separated because detecting most of the experimental mistakes on $S_\theta(f)$ is significantly easier than on $S_\psi(f)$. For $f \to 0$, it holds $|\mathrm{H}(jf)|^2 \sim f^2$. High slope processes such as frequency flicker ($S_\psi(f) = b_{-3}/f^3$) dominate in this region, which compensates the decreasing of sensitivity. The phase noise measurement is therefore possible. The function $|\mathrm{H}(jf)|^2$ has a series of zeros, in the vicinity of which the experimental results are not useful. In practice, the first zero sets the maximum measurement bandwidth to $0.9/\tau$, as discussed in [49].

Some devices, which are components of OEO, should be measured to make sure that the phase noise is sufficiently low. When a pure sinusoidal signal $s_\mathrm{i}(t)$ of frequency ν passes through a device under test (DUT), the latter adds its internally generated noise. Then, the DUT output signal can be represented as

$$s_\mathrm{o}(t) = \sqrt{R_0 P_\mathrm{o}}(1 + \alpha(t))\cos(2\pi\nu t + \varphi(t)), \tag{2.12}$$

where R_0 is the impedance and P_o is the power at the output of the DUT; $\alpha(t)$ and $\varphi(t)$ are, respectively, the relative AM noise and the PM noise generated by the DUT.

A measurement system (see Fig. 2.5) similar to the one presented in Fig. 2.4 is traditionally used to measure phase noise of a device [51]. AM noise is usually much less than PM noise and the saturated double balanced mixer is less sensitive to AM noise than to PM noise. Therefore this system allows the measurement of PM noise.

When two identical DUTs are available, the measurement system can be modified by inserting the second device to the second branch. It doubles the DUT phase noise detected by the mixer when the noise is statistically independent and thus increases the system sensitivity. This measurement system is shown in Fig. 2.6. The device D1 is put in the

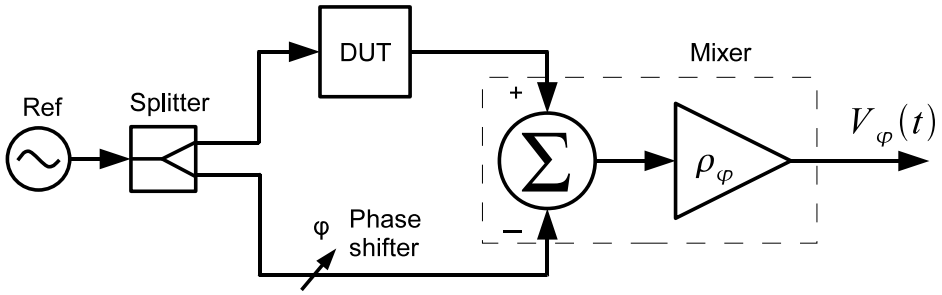

Figure 2.5: A basic scheme of phase noise measurement [51].

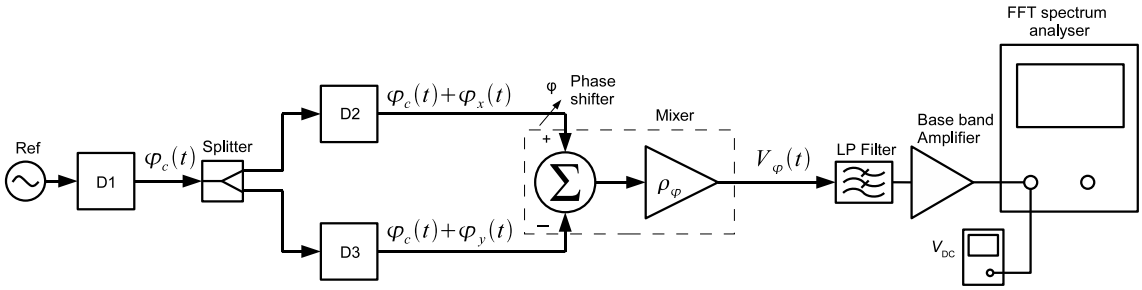

Figure 2.6: The block scheme of components phase noise measurement. D1 is a device, D2, D3 are devices of the same type each.

scheme to emphasize that the phase noise common for both branches is not detected by the measurement system.

The voltage at the output of mixer is defined by the following equation

$$V_\varphi(t) = \rho_\varphi \left[(\varphi_\mathrm{c}(t) + \varphi_\mathrm{x}(t)) - (\varphi_\mathrm{c}(t) + \varphi_\mathrm{y}(t))\right] = \rho_\varphi \left[\varphi_\mathrm{x}(t) - \varphi_\mathrm{y}(t)\right]. \tag{2.13}$$

As one can see, the phase noise common for the two branches is cancelled by the mixer and only the difference of the phase noises in the two branches is measured. The phase noise of the carrier and of other components in the common path (as $\varphi_\mathrm{c}(t)$) is eliminated by the mixer. Only the phase noise of the separate branches is measured, if the branches are statistically independent. It is also supposed that their mean equals to zero. It can be expressed in the following way

$$\begin{aligned}
\mathbb{E}\left\{|X-Y|^2\right\} &= \mathbb{E}\left\{(X-Y)(X^*-Y^*)\right\} \\
&= \mathbb{E}\left\{XX^* - XY^* - YX^* + YY^*\right\} \\
&= \mathbb{E}\left\{XX^*\right\} + \mathbb{E}\left\{YY^*\right\} \\
&= 2\,\mathbb{E}\left\{XX^*\right\} \\
&= 2\,S_{XX},
\end{aligned} \tag{2.14}$$

where $\mathbb{E}\{\}$ stands for the statistical expectation, the uppercase X and Y are the single-sided Fourier transform of the $\varphi_\mathrm{x}(t)$ and $\varphi_\mathrm{y}(t)$, S_{XX} is the power spectral density, and the superscript '*' stands for complex conjugate. In practice, the expectation is replaced with the average on a suitable number of measured values.

2.3.2 Photonic delay line for phase noise measurement

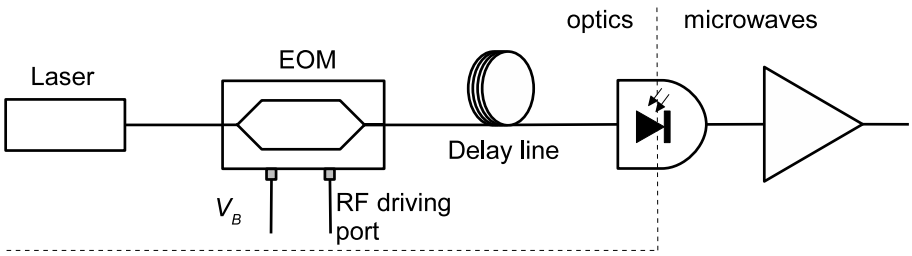

Figure 2.7: A basic scheme of photonic delay line channel [52].

Figure 2.7 shows the optical-fiber microwave delay unit [52]. We use a 2 km (10 μs) fiber. As well as for OEO (see the Section 2.1), the fiber spool is enclosed in a cylinder thermally insulated from the environment and temperature stabilized at room temperature. The advantage of the temperature control vs. a passive time constant, i.e., large metal mass and thermal insulator, is still questionable. For short-term fluctuations (100 ms or less), the passive stabilization would certainly be preferable because it does not suffer from the noise inherent in the control. On the other hand, we need to keep the delay and the phase relationships stable for the duration of the correlation measurements, which can last up to one day.

As in the OEO, the light source is the EM4 laser, temperature controlled and powered with a low-noise current source. We choose an EOM JDSU Z5 having low half-wave voltage ($V_{\pi\mathrm{RF}} \simeq 3.9$ V). The available EOM has a low-frequency photodetector with an output port, which is used to stabilize the bias point as will be shown in Section 2.4.2. The photodetector is the InGaAs p-i-n diode DSC40S. The microwave signal is amplified by a low phase noise amplifier AML.

2.3.3 Cross-correlation method

The measured noise PSD includes the device under test (DUT) noise and the instrument background. Improved sensitivity is obtained using a cross-spectrum method, in which two equal instruments measure simultaneously the same DUT. A short description is given here. The mathematical details and the in-depth analysis of the experimental method are given in [53].

Let $a(t)$ and $b(t)$ be the background noise of the two instruments, and $c(t)$ the common noise. By definition, $a(t), b(t)$ and $c(t)$ are statistically independent. The two outputs are

$$x(t) = c(t) + a(t) \tag{2.15}$$

$$y(t) = c(t) + b(t). \tag{2.16}$$

We denote the Fourier transform with the uppercase of the time-domain function, thus $a(t) \leftrightarrow A(jf)$, etc. The cross-spectrum averaged on m measurements is

$$\begin{aligned} S_{yx}(f) &= \langle YX^* \rangle_m \\ &= \langle [C+A] \times [C+B]^* \rangle_m \\ &= \langle CC^* \rangle_m + \langle CB^* \rangle_m + \langle AC^* \rangle_m + \langle AB^* \rangle_m \\ &= S_c(f) + O(\sqrt{1/m}) \ . \end{aligned} \tag{2.17}$$

Owing to statistical independence, the cross terms decrease as $\sqrt{1/m}$.

The measurement and the assessment of the instrument background go as follows.

1. With no DUT noise, and maintaining the hypothesis of statistical independence of the two channels, it holds that $c = 0$. The statistical limit of the measurement is

$$S_{yx}(f) \approx \sqrt{\frac{1}{m} S_a(f) S_b(f)} \qquad \text{(stat. limit)}. \tag{2.18}$$

   Accordingly, a 5 dB improvement on the single channel noise costs a factor of 10 in averaging, thus in measurement time.

2. Breaking the hypothesis of the statistical independence of the two channels, we interpret $c(t)$ as the correlated noise of the instrument, due to environment, crosstalk, etc... Thus, still at zero DUT noise, we get the hardware limit of the instrument sensitivity

$$S_{yx}(f) = S_{c'}(f) \qquad \text{(hardware limit)}. \tag{2.19}$$

3. Now we introduce the DUT noise. If (i) m is large enough for the statistical limit to be negligible, and (ii) the background is negligible as compared to the DUT noise, the cross spectrum gives the DUT noise

$$S_{yx}(f) = S_c(f) \simeq S_{c'}(f) \qquad \text{(DUT meas.)}. \tag{2.20}$$

This is the regular use of the instrument.

2.3.4 Dual-channel phase noise measurement bench

Figure 2.8 shows the scheme of the instrument [54]. The instrument consists of two equal and fully independent channels that measure the oscillator phase noise by comparing its phase to a delayed copy. The single channel noise is removed using the cross-spectrum method [Eq. (2.20)] before calculating the oscillator phase noise $S_\varphi(f)$ with Eq. (2.10).

Looking at one channel, we observe that the microwave signal is split into two branches before the EOM, so that the long branch consists of a modulator, an optical fiber (delay

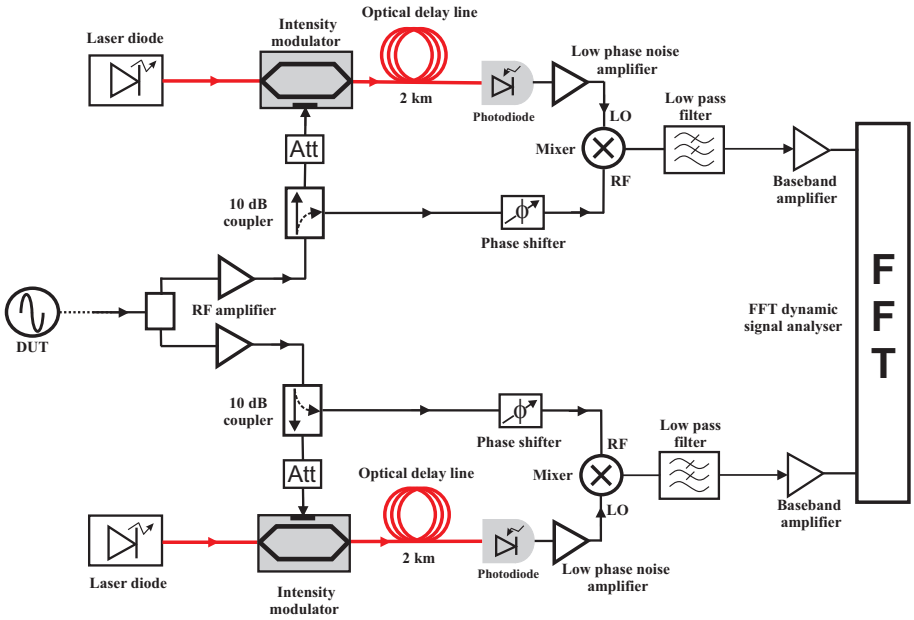

Figure 2.8: Scheme of the dual-channel instrument for phase noise measurement [54, 52].

τ), a photodetector and a microwave amplifier, while the short branch is a pure microwave path of negligible length. This differs from the single channel instrument ([49], Fig. 7), in which the signal was split at the output of the EOM. The absence of the photodetector and the microwave amplifier in the short branch, yields lower noise, and in turn faster convergence of the correlation algorithm. Additionally, lower laser power is needed. A further, yet minor, reason is that the noise of a Wilkinson microwave power splitter, shared by the two channels, is negligible for our purposes [55, 47]; conversely, we have no first-hand knowledge in the case of an optical power splitter. The price to pay for the fully-microwave short branch is that we don't have an optical input, so we are not able to measure the noise of microwave-modulated light beams.

The two RF amplifiers increase DUT signal to the saturation level of the mixers at one port, and maximum modulation index for EOM. They also serve as limiting amplifiers to reduce possible contribution of amplitude noise in the total measured noise because it can have effect on indications of the same order – if not greater – than the phase noise [56] in some spectral windows. The noticeable signal compression appears at the power splitter input signal level of about +4 dBm. So the DUT power should be at least +4 dBm. The balance of power between the mixer and EOM is achieved by introducing attenuators. The power at the second port of each mixer is adjusted by varying the optical power. In practice, the appropriate RF power level at mixers ports is achieved at the laser power of about 35 mW.

The mixers are used as phase detectors, with both inputs saturated. In this way, the amplitude fluctuations have little effect on the output signal. The low-pass filters are used to eliminate the high frequency components of the mixer output signal. The baseband amplifiers are the low flicker-noise DC amplifiers described in Ref. [57].

To define proper input power levels, we have done a series of measurements of the mixer response as a phase detector at different input power according the scheme shown in Fig. 2.9. One synthesizer is frequency shifted by 159 kHz, that is, 1 Mrad/s and we could observe triangular curves on the screen of oscilloscope of different slope depending on mixer input power. The mixer input power was verified with a RF power meter. The

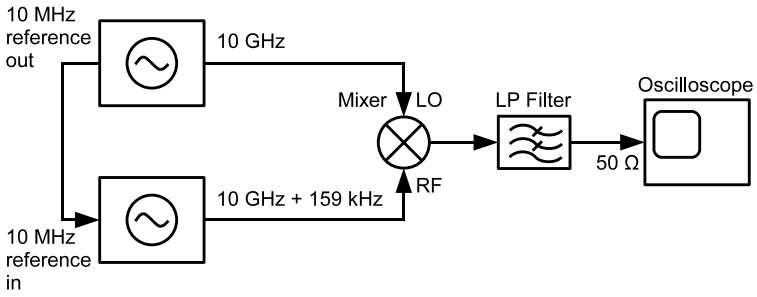

Figure 2.9: The measurement scheme of the phase-voltage conversion factor in a mixer, at different power levels.

results are shown in Fig. 2.10 as a 3D diagram and for power levels of interest in Fig. 2.11 as a 2D diagram.

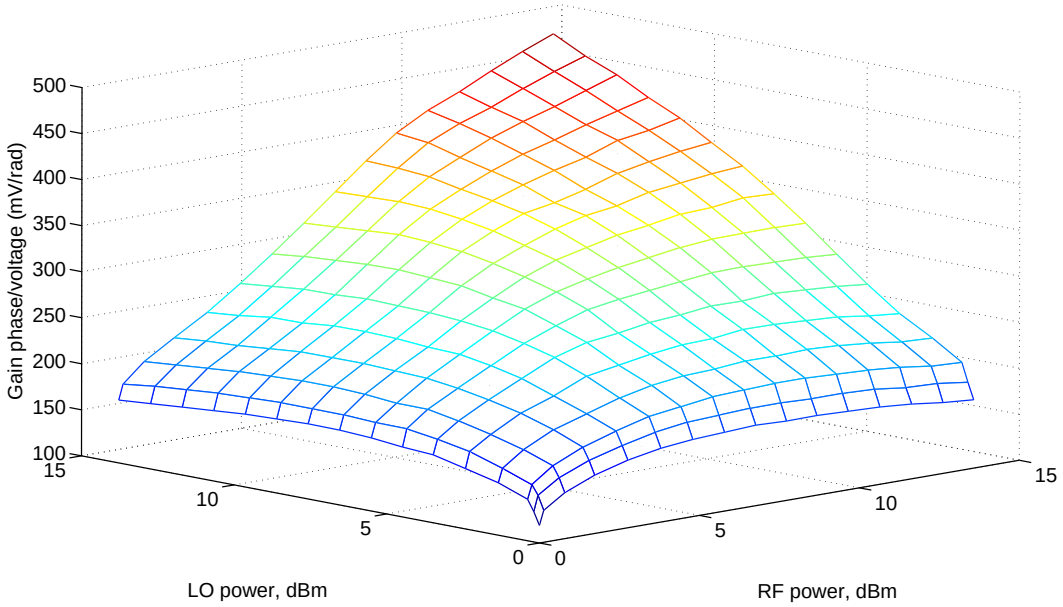

Figure 2.10: The phase-voltage conversion factor of the mixer at different power levels.

As one can see, the 3D diagram of the phase-voltage conversion factor of the mixer Marki M4-0226LC is symmetric regarding the power at input ports. The sensitivity of the phase-voltage conversion factor to input power fluctuation decreases at higher powers. According to the data sheet, the saturation is reached in the range of input

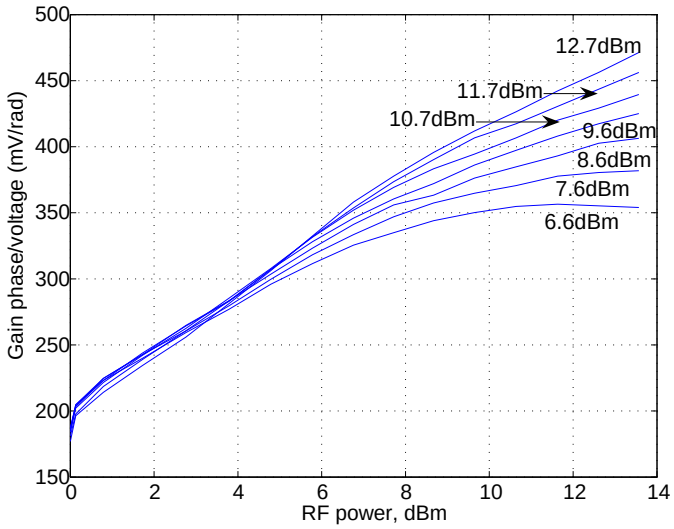

Figure 2.11: The phase-voltage conversion factor of the mixer at different power levels.

power $+7 \ldots +13$ dBm. Maximum power ratings without damage for this mixer is $+23$ dBm at $+25$ °C and is derated linearly to $+20$ dBm at $+100$ °C. So we have enough large margin of input power to operate in saturation mode for both input ports. We have chosen the input power $+12$ dBm to ensure the saturation, because the input power can slowly fluctuate during measurement cycle. Increasing the input power also increases the conversion factor and decreases the phase noise measurement bench background noise.

Adjustment of the measurement bench consists in adjusting the phase shift between the mixer input signals with the phase shifters to obtain the quadrature condition, which manifests as zero mean voltage at the outputs of the measurement bench.

In principle, the background noise can be measured using an oscillator of lower phase noise. At present time, this could only be possible with a cryogenic oscillator or with other exotic sources. Otherwise the background noise can be found using a special setup excluding the oscillator phase noise from indications. Actually the photonic delay-line channel of the measurement bench is the same as in the OEO. Therefore we will discuss its phase noise and the background noise in the next chapter (Section 3.1) while determining the phase noise sources in OEO.

2.4 Auxiliary components of the measurement bench

The measurement at low Fourier frequencies or at high frequency resolution narrow takes proportionally long time. Using the cross-correlation method, the measurement time increases by a factor 10 for every 5 dB noise rejection. For this reason we have to stabi-

lize the entire system against the temperature fluctuation and other fluctuations of the environment.

2.4.1 Mixer quadrature control loop

When the LO and the RF ports of a mixer are saturated by sinusoidal signals of the same frequency ω_0, the IF signal contains their product and higher order frequency terms. Their product is

$$\cos(\omega_0 t + \varphi)\cos(\omega_0 t - \theta_{\mathrm{RF}}) = \frac{1}{2}\cos(2\omega_0 t + \varphi - \theta_{\mathrm{RF}}) + \frac{1}{2}\cos(\varphi + \theta_{\mathrm{RF}})\,. \tag{2.21}$$

When θ_{RF} is equal to $\pi/2 + 2\pi n$ ($n \in \mathbb{N}$), and when the term $2\omega_0$ and higher frequency terms are eliminated by low pass filtering, we have only the term $-\sin(\varphi)/2$, which is equal to $-\varphi/2$ for $\varphi \ll 1$. Denoting the phase to voltage conversion factor of mixer as ρ_φ [V/rad], we get the mixer output voltage

$$V = \pm\rho_\varphi \varphi, \tag{2.22}$$

where the sign is opposite to the sign of $\pi/2$ in the quadrature condition $\theta_{\mathrm{RF}} = \mp\pi/2 + 2\pi n$.

Therefore to use a mixer as a phase detector, the signals at RF and LO inputs should be in quadrature and the inputs should be saturated. The mixer mean output voltage equals to 0 V at this condition. It can be easily verified by a DC voltmeter. During long measurements, the channel delay changes, as well as the oscillator average frequency. These changes produce significant deviation from the quadrature condition and make long measurements impossible. A measurement session of one hour requires several hours warming up. Moreover shields were needed to break air flow turbulence. That is why a control loop keeping the quadrature condition is necessary. Let's consider the principle and the scheme of the control loop that we use in experiments.

The optical length of the photonic delay line is the physical length of the fiber divided by its refractive index. The latter depends on the light wavelength through dispersion of the silica fiber. Since the wavelength can be tuned through laser crystal temperature, it is possible to control the phase of the microwave at the output of the delay line, $\phi = \omega\, n(\lambda) L/c$, and thus the relative quadrature condition through laser diode (LD) temperature controller.

The control can be implemented as shown in Fig. 2.12. The block "I" represents an integrator, "PID" is the PID controller of LD temperature, "TEC" is the thermoelectric cooler (a Peltier element), "Th" is the thermistor, "LD PD A" is the optical delay line, photodiode, and amplifier, "PS A" is the phase shifter and amplifier, "F A" is the low pass filter and the baseband amplifier. Some of the blocks are nonlinear but they can be linearized for the purpose of considering the system stability.

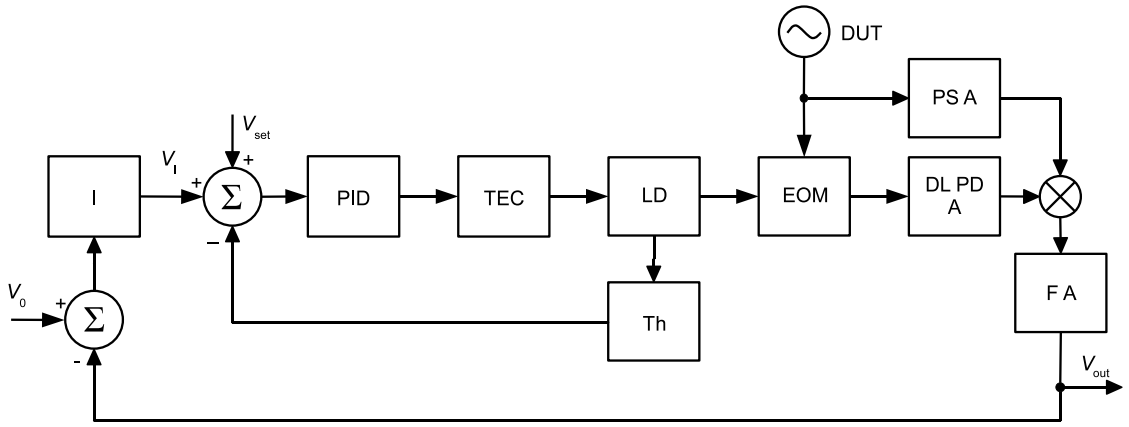

Figure 2.12: Control loop block diagram.

The LD we use has a thermistor and a thermoelectric cooler element inside. The thermistor resistance is related to the laser crystal temperature as follows [58]

$$T(R) = \frac{B_{\text{val}} T_0}{T_0 \ln\left(\frac{R}{R_0}\right) + B_{\text{val}}} \qquad [\text{K}], \tag{2.23}$$

where R_0 is the thermistor nominal resistance at temperature T_0, T_0 is the nominal temperature (typ. 298.15 K = 25 °C), B_{val} is the energy constant. The values of R_0 and B_{val} are given in LD datasheets. For the EM4 (EM253) laser: $R_0 = 10$ kΩ, $B_{\text{val}} = 3892$.

The inverse dependence is

$$R(T) = R_0 e^{\frac{B_{\text{val}}(T_0 - T)}{T\, T_0}} . \tag{2.24}$$

It can be linearized for the operational temperatures region (+20 . . . + 35 °C) as

$$R(T) = R_0 \left(1 + \frac{B_{\text{val}}(T_0 - T)}{T_0^2}\right) . \tag{2.25}$$

To consider the possibility of linearizing the TEC operation, a simple model [59] that predicts TEC thermal load temperature (T_1) as a function of load heat production, TEC data-sheet numbers, heatsink parameters, TEC drive current, and ambient temperature can be used.

$$T_1 = (-\Pi\, I_{\text{TEC}} + I_{\text{TEC}}^2 R_{\text{p}}/2 + Q_1)/(C_1 + C_{\text{p}}) + (Q_1 + I_{\text{TEC}}^2 R_{\text{p}})/(C_{\text{h}} + T_3) \tag{2.26}$$

where $\Pi = (Q_{\max} + I_{\max}^2 R_{\text{p}}/2)/I_{\max}$ is the Peltier constant, $Q_{\max}$ is the maximum heat transfer, $R_{\text{p}} = V_{\max}/I_{\max}$ is the TEC resistance, I_{TEC} is the TEC drive current, Q_1 is the heat produced by thermal load (Watts), C_1 is the conductivity (Watts/°C) of thermal load to ambient, $C_{\text{p}} = Q_{\max}/\Delta T_{\max}$ is the TEC thermal conductivity, C_{h} is the heatsink thermal conductivity to ambient, T_3 is the ambient temperature.

We don't have most of the data for the TEC of the EM4 laser but we can say that this function can be linearized in a small interval of temperatures near the operation point.

The thermistor resistance serves as an input signal for the temperature controller TED200C that controls LD temperature through the TEC element. A desired value of the thermistor resistance is defined by a knob (V_{set} in the block scheme) on the front panel of the controller. The controller has also an analog temperature control input "TUNE IN", with input range of $-10 \ldots +10$ V and conversion coefficient 2 kΩ/V ± 5%. This voltage adds to the internal voltage defined by the knob and the thermistor resistance setting is proportional to the sum voltage. The temperature controller TED200C is a proportional-integral-derivative controller (PID controller) with the transfer function and the time constant depending on adjustment. Usually it is adjusted so that the actual temperature reaches the set temperature in short time with at most one overshoot. It can be described by the following transfer function [19]

$$H_{\text{PID}}(s) = G_{\text{p}} \left(1 + \frac{1}{s\tau_{\text{i}}} + s\tau_{\text{d}}\right) , \tag{2.27}$$

where G_{p} is the proportional gain, τ_{i} is the integral time, τ_{d} is the derivative time. The heat transfer from TEC to TE can be represented by a model of a rod of length ℓ and thermal diffusivity α at the condition of absence of radial heat transfer. The input is the temperature at one end of the rod, the output is the temperature at another end. In this case the transfer function [19] is

$$H_{\text{TEC-TE}}(s) = \frac{1}{\cosh\left(\sqrt{s\tau_{\text{r}}}\right)} , \tag{2.28}$$

where $\tau_{\text{r}} = \ell^2/\alpha$. The thermistor measures the temperature of LD. Therefore the LD temperature can be considered equal to the one of thermistor.

The optical length of the fiber is the physical length divided by the refractive index, which depends on optical frequency. This dependence can be calculated with the dispersion constant, which can be found in the data sheet of the specific fiber at a given wavelength. Such dispersion constant for optical fiber SMF-28e that we used in our experiments is $D_\lambda = 18$ ps/(km · nm) at 1550 nm. Therefore the delay is produced by an optical delay line of length L, at the wavelength λ is

$$\tau_{\text{DL}} = \frac{L\, n(\lambda)}{c} \approx \frac{L\, n(\lambda_0)}{c} + L D_\lambda \Delta\lambda . \tag{2.29}$$

In our case the delay is about 10 μs, which is negligible to the response time of the control.

Using the considered approximations and data, we can estimate the static gain of the open loop excluding the integrator. It can be expressed in the following way

$$G_{\text{stat}} = C_{\text{VR}} C_{\text{RT}} C_{\text{T}\lambda} L D_\lambda \omega_0 \rho_{\text{m}} G_{\text{m}} , \tag{2.30}$$

where $C_{\mathrm{VR}} = 2$ kΩ/V is the voltage to thermistor resistance conversion factor, C_{RT} [K/Ω] is the thermistor resistance to temperature conversion factor, $C_{\mathrm{T}\lambda}$ [nm/K] is the temperature to wavelength conversion factor, and $G_{\mathrm{m}} = 100$ is the amplifier gain.

Equation (2.23) can be approximated for small deviations of R at 25 °C as

$$T(R) = 320.8 - 0.0023R\,. \tag{2.31}$$

We have the value of $C_{\mathrm{T}\lambda}$ for the JDSU CQF935 laser (about 0.1 nm/K) but not for the EM4 laser. Both of them are DFB lasers, they have similar construction and almost the same wavelength. Therefore we will use this value to estimate the possible value of G_{stat}. ρ_{m} is about 0.445 V/rad at the LO and RF signal power of 12 dBm. Taking into account these values, we have $G_{\mathrm{stat}} = 46.3$.

The operating temperature range 27 ± 7 °C gives $\pm 7\, C_{\mathrm{T}\lambda} L D_\lambda \omega_0 = \pm 1.58$ rad. In practice, during phase noise measurements, the deviation from the quadrature condition is significantly lower. Therefore, this way gives the possibility to control the quadrature condition during the measurement. Since the quadrature control keeps the quadrature condition and at the same time the temperature variations are very slow, these variations can be considered small and the response of the system part from EOM to the output amplifier for wavelength deviations can be linearized and the transfer function can be represented by the product $H_\lambda = L D_\lambda \omega_0 \rho_{\mathrm{m}} G_{\mathrm{m}}$.

Since we linearized the control loop components for small signals, we can write the transfer function of open loop without the integrator as

$$H_{\mathrm{OL}}(s) = \frac{H_{\mathrm{PID}}(s) H_{\text{TEC-TE}}(s)}{1 + H_{\mathrm{PID}}(s) H_{\text{TEC-TE}}(s)} H_\lambda\,. \tag{2.32}$$

To determine the real open-loop parameters, we measured the stationary behavior of the open loop as the output voltage vs. input voltage. This is shown in Fig. 2.13 together with the thermistor resistance. The output voltage is well approximated by

$$V_{\mathrm{out}}(V_{\mathrm{I}}) = -133 V_{\mathrm{I}}^3 + 56 V_{\mathrm{I}}^2 + 8.33 V_{\mathrm{I}}. \tag{2.33}$$

The dependencies of V_{out} and R_{TE} in the figure are similar. Therefore we can suppose that the nonlinearity is mainly produced by TEC and TE. This function gives the mean $G_{\mathrm{stat}} = 14$ for the range shown. The difference between the measured and estimated G_{stat} can be explained by the difference in $C_{\mathrm{T}\lambda}$. This means that the wavelength of EM4 laser is more stable with regard to temperature.[1]

Then we measured the step response $g(\tau)$ by feeding the square wave voltage (100 $\mathrm{mV_{pp}}$) at the "TUNE IN" input (see Fig. 2.14). By matching simulated step response to

[1] Indeed EM4 is a recent DFB laser, with most probably improved features compared to the JDSU CQF935, an older device.

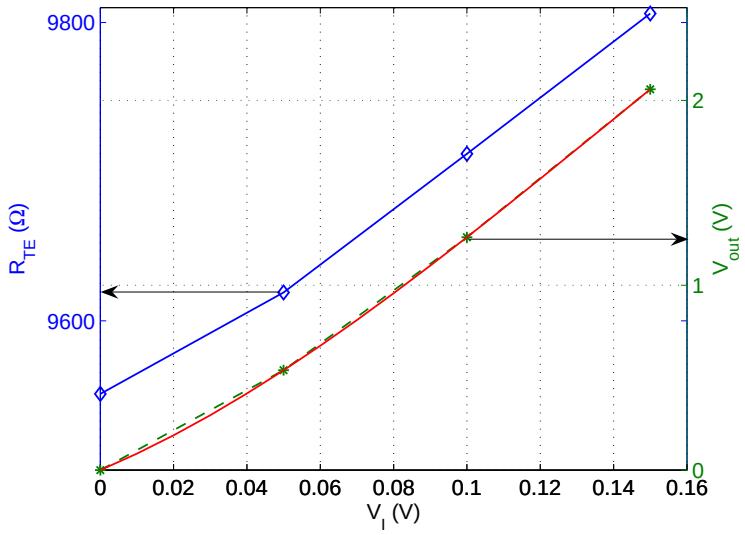

Figure 2.13: V_{out} and the thermistor resistance vs. V_{I}. The red solid line is the output voltage $V_{\text{out}}(V_{\text{I}})$ approximation. The green dashed line is the measured output voltage. The blue solid line is the thermistor resistance.

the measured one, we found parameters for Eq. (2.32). The parameters are: $G_{\text{p}} = 3.0$, $\tau_{\text{i}} = 0.45$ s, $\tau_{\text{d}} = 0.15$ s, and $\tau_{\text{r}} = 1.5$ s. The simulated step response is presented in Fig. 2.15. We have a good correspondence to the measured step response. Therefore we can use these parameters for estimating the system stability.

Now we consider the integral control[2] (the I control). The I control was chosen because it gives the zero steady-state error and because the controlled parameter (V_0) has always to be zero. Temperature instability typically produces very slow deviations that can be considered almost a steady-state. The proportional and derivative actions are redundant in this case. To eliminate any influence of the control loop on measurements with frequency bandwidth more than 0.1 Hz, we have chosen the time constant of the integrator $\tau_{\text{I}} = 100$ s.

Now we can consider the loop stability. The quadrature open-loop transfer function is

$$H_{\text{QOL}}(s) = H_{\text{OL}}(s)\frac{1}{s\tau_{\text{I}}}\,. \tag{2.34}$$

The Nyquist plot of $H_{\text{QOL}}(s)$ is shown in Fig. 2.16. The critical point -1 is on the left of the Nyquist curve when it is traversed for increasing ω. Therefore the closed loop is stable. The stability margin is 0.97, the phase margin is 89°, and the gain margin is 160.

Now we will consider the influence of quadrature control loop on the measurement

[2]see Appendix A for technical details on the electronic circuit.

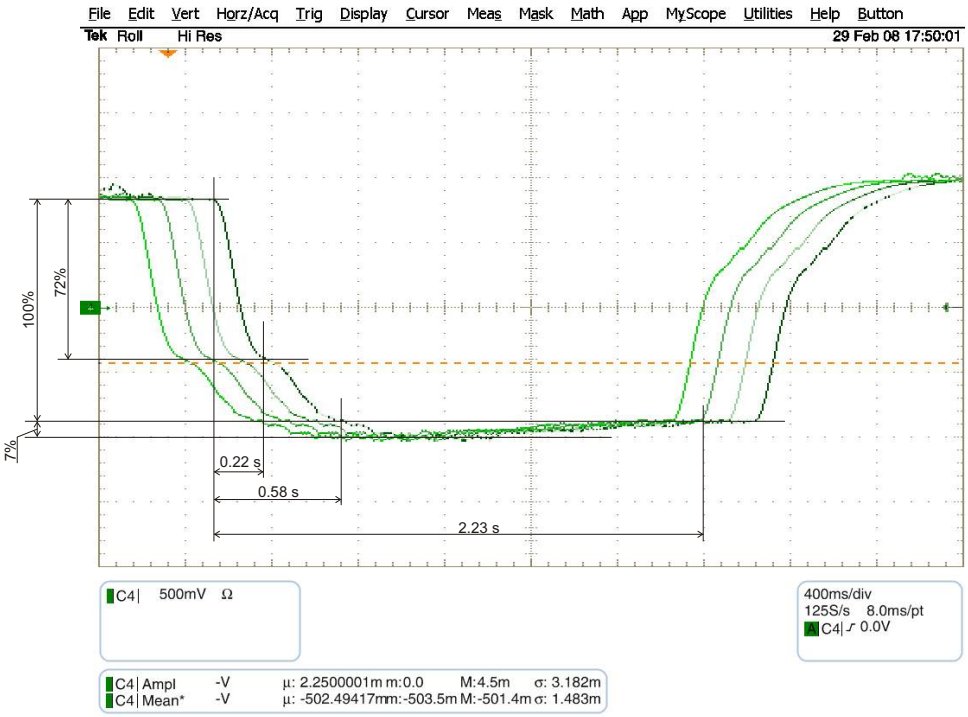

Figure 2.14: Measured step response.

indications. The transfer function for the phase of DUT is

$$H_{\varphi_{\mathrm{RF}}}(s) = \frac{\rho_{\mathrm{m}} G_{\mathrm{m}}}{1 + H_{\mathrm{QOL}}(s)} \,. \tag{2.35}$$

The normalized transfer function $H_{\varphi_{\mathrm{RF}}}(s)$ is shown in Fig. 2.17. The value of this function is 0 dB for $f \geq 0.1$ Hz but there is a 0.25 dB bump at 0.34 Hz. So the control has very little effect on the phase-noise beyond 0.1 Hz. The bump is supposedly caused by the laser temperature control and therefore it can vary depending on the PID controller tuning.

2.4.2 MZ operating point control loop

The $LiNbO_3$ MZ modulator is highly sensitive to temperature. The microwave power affects the crystal temperature via the Joule effect in the termination. At the scale of several hours, the ambient temperature also changes significantly. So, the MZ half-transparent bias point is subject to permanent change. This creates systematic errors. To stabilize the operating point and eliminate this error, we have designed an Integrator controller that controls the bias so as to keep the MZ modulator semi-transparent in average.

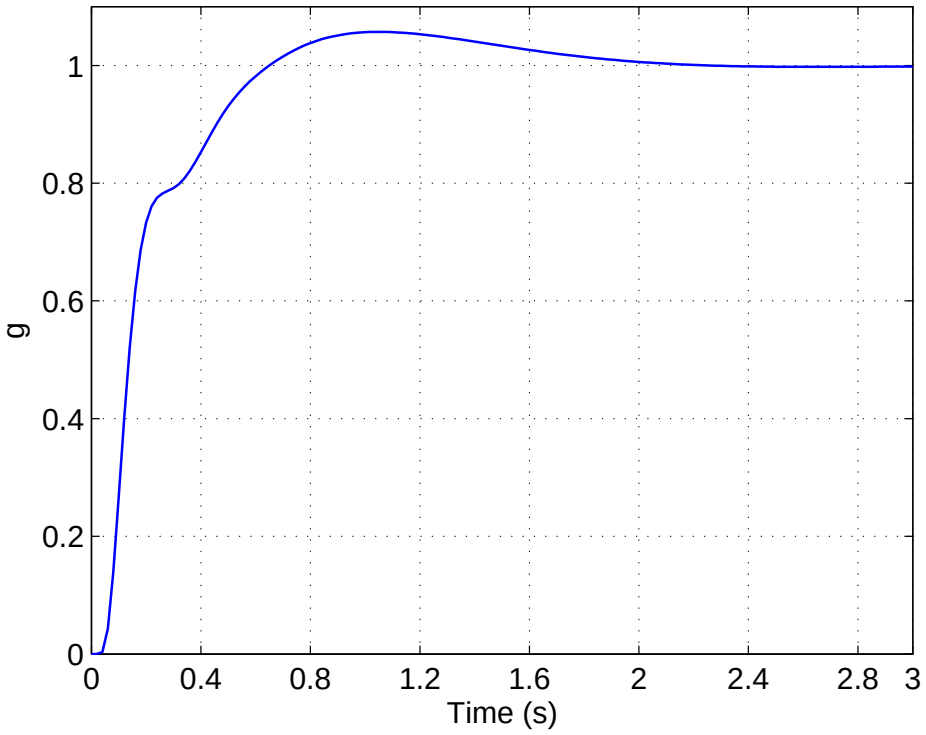

Figure 2.15: Simulated step response.

The JDSU Z5 modulators used in the phase noise measurement bench have internal photodiodes for bias and power control. Since we deal with slow temperature variations as in the case of the quadrature controller, and since we also want the zero steady-state error, we use an I controller. The block diagram of the controller is shown in Fig. 2.18. The LD and the JDSU Z5 modulator are a part of the phase noise measurement bench. The DUT is not connected to the modulator directly as one can see in Fig. 2.8, but we have simplified this part in Fig. 2.18, only to recall that the input measurement signal is connected to this port. The modulator is a non-linear device but its operation point is expected to be kept around the linear part. The modulator can thus be considered as linear from the RF input to the optical output and from the bias input to the V_{out} output (for the small deviations), and we can use the transfer functions to describe it. Since the BW of the monitor photodiode is of 100 kHz, the microwave signal at 10 GHz can not influence the control loop. Therefore we can consider the control and the signal paths as independent. The modulator equation relating is

$$V_{\text{out}}(t) = \frac{P_{\text{opt}}\rho R_{\text{PD}}}{2}\left[1 + \sin\left(\pi\frac{V_{\text{B}}(t)}{V_{\pi\text{B}}} + \phi(t)\right)\right], \tag{2.36}$$

where $\phi(t)$ is the MZ modulator offset phase. Here we make $\phi(t)$ depending on time to show that it changes in time (primarily due to the temperature changes). This dependence makes the operating point control loop necessary.

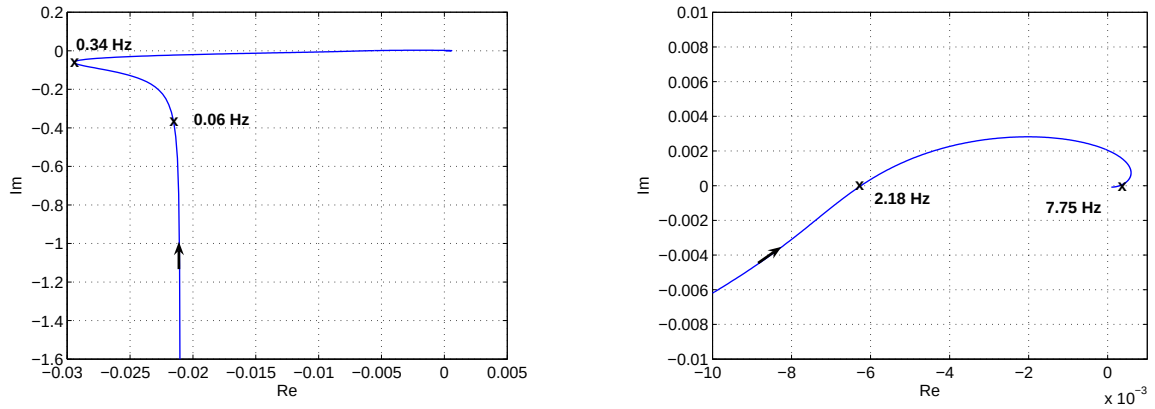

(a) (b)

Figure 2.16: The Nyquist plot of $H_{\mathrm{QOL}}(s)$.

This relation can be linearized for small deviations of V_{B} about the half-transparency point. The derivative of (2.36) is

$$\frac{\delta V_{\mathrm{out}}(t)}{\delta V_{\mathrm{B}}(t)} = \frac{P_{\mathrm{opt}}\rho R_{\mathrm{PD}}}{2}\frac{\pi}{V_{\pi\mathrm{B}}}\cos\left(\pi\frac{V_{\mathrm{B}}(t)}{V_{\pi\mathrm{B}}} + \phi(t)\right). \tag{2.37}$$

Since for small deviations the cosine term is equal to 1, the deviations ratio and the small deviation transfer function become

$$H_{\Delta V_{\mathrm{B}}} = \frac{\Delta V_{\mathrm{out}}}{\Delta V_{\mathrm{B}}} = \frac{P_{\mathrm{opt}}\rho R_{\mathrm{PD}}}{2}\frac{\pi}{V_{\pi\mathrm{B}}}. \tag{2.38}$$

In practice, the optical power P_{opt} is about 30 mW. According to the data sheet, the photodiode responsivity $\rho = 25$ mA/W and $V_{\pi\mathrm{B}} = 2.5$ V. The current-to-voltage conversion resistor was chosen $R_{\mathrm{PD}} = 1$ kΩ, so that $H_{\Delta V_{\mathrm{B}}} = 0.47$ in our case. After linearization the transfer function of the control loop is

$$H(s) = \frac{\Delta V_{\mathrm{out}}}{\Delta V_0} = \frac{\frac{H_{\Delta V_{\mathrm{B}}}}{s\tau_{\mathrm{I}}}}{1 + \frac{H_{\Delta V_{\mathrm{B}}}}{s\tau_{\mathrm{I}}}}. \tag{2.39}$$

The integrator time constant was chosen $\tau_{\mathrm{I}} = 0.1$ s basing on characteristics of available capacitors and resistors because the stability margin is large. The Nyquist plot for the open loop is a line on the negative part of imaginary axis going to zero when $\omega \to \infty$. So the critical point -1 is on the left of the line and the system is stable. The stability margin is 1, the phase margin is 90°, and the gain margin is ∞.

2.5 Conclusion

The application of optical fiber as a delay line in OEO and a phase noise measurement bench is considered. The stochastic nonlinear delay differential equation for delay line

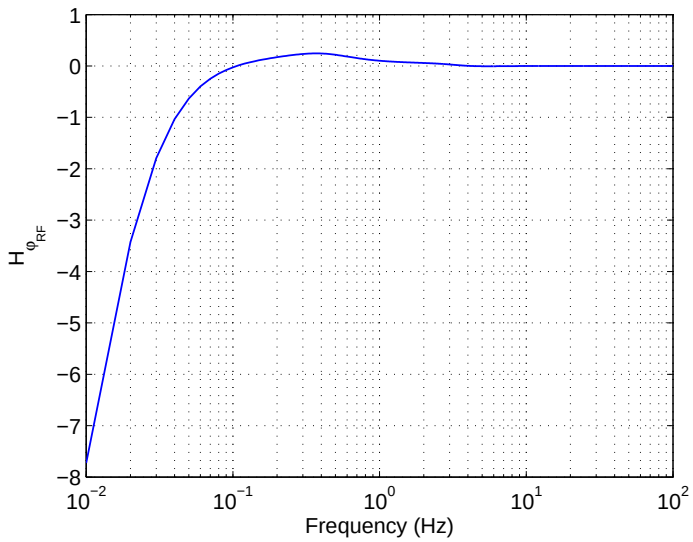

Figure 2.17: The normalized transfer function $H_{\varphi_{\mathrm{RF}}}(s)$.

oscillators is modified to describe the OEO dynamics. The methods for measuring very low phase noise of oscillators and devices are described. Auxiliary devices improving stability of the phase noise measurement are introduced.

In the next chapter, we will consider phase noise properties of some OEO architectures using the introduced analysis and measurement methods.

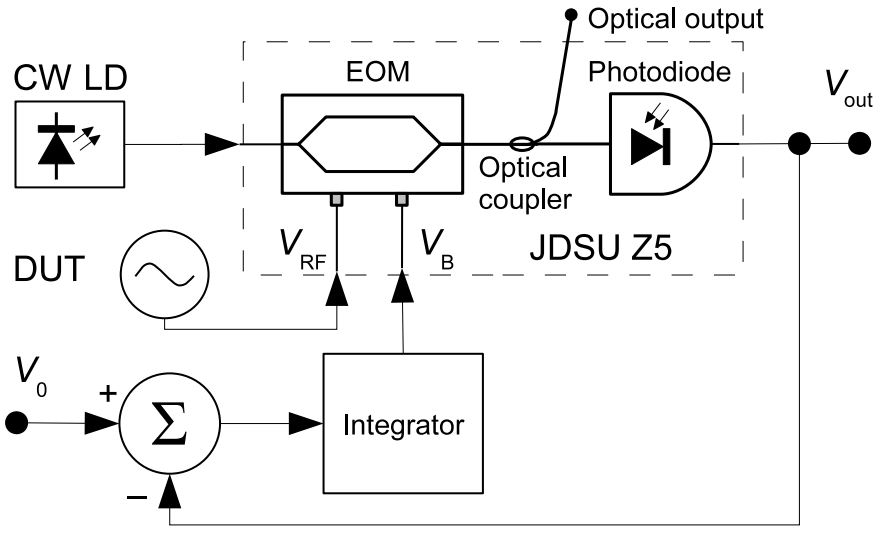

Figure 2.18: The block scheme of MZ EOM operating point control loop.

Chapter 3

OEO phase noise

As it was mentioned in Section 1.4, in the quest for lower phase noise, we can reduce the noise sources and reduce the system sensitivity. We start with the phase noise sources, estimating their contribution to the total phase noise in OEO, and then we consider the possibility to reduce them.

3.1 Phase noise contributions of OEO components

In order to identify the OEO components that most contribute to the phase noise, we measured them connected in cascade which partially reproduces the open loop of the oscillator. We used the measurement principle explained in Section 2.3.1.

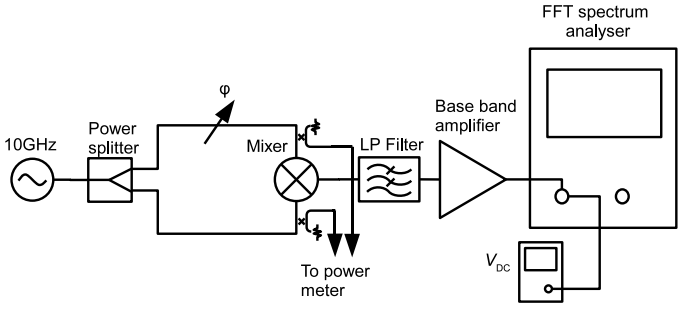

Figure 3.1: The background phase noise measurement [60].

First of all, we measured the background noise of the measurement system (Fig. 3.1), that is, without the OEO components in the branches. Then we added a low phase noise amplifier to each branch (Fig. 3.2) and we progressively added the other components (Figs. 3.3-3.5).

The results of phase noise measurement are presented on (Fig. 3.6).

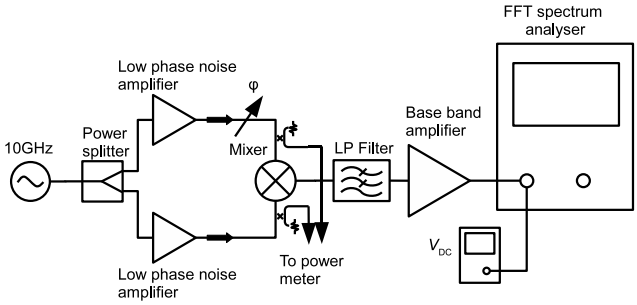

Figure 3.2: The phase noise of amplifiers measurement [60].

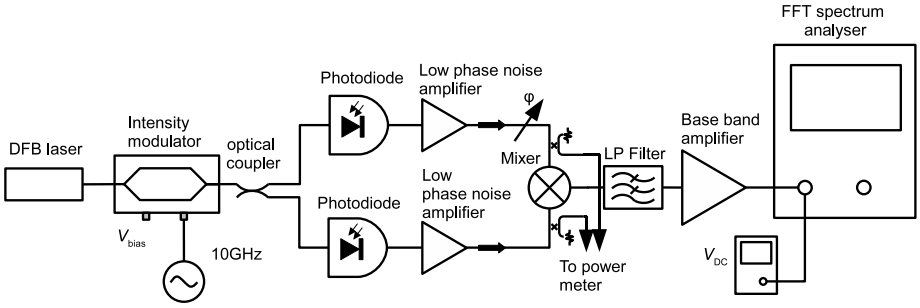

Figure 3.3: The phase noise of amplifiers with photodiodes measurement [60].

In the first two cases, we can see the flicker noise. The amplifiers have almost the same phase noise the mixer, but the total phase noise level increases. The peaks at 50 Hz and multiples are caused by the power supplies. Additional phase noise bursts and bumps appear when the optical components are added. The bursts around 40 kHz are ascribed to optical reflections. As one can see, the most significant phase noise increase appears when the delay line is included in the system. We believe that this phase noise is caused by the interaction of lasers frequency noise and dispersion of the delay line. If we could suppress this effect, the phase noise would decrease by about 10 dB. This statement must be verified by measuring the laser frequency noise. Then it will be possible to estimate its contribution to the total phase noise.

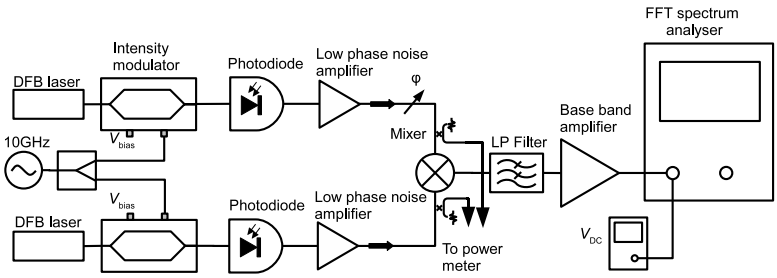

Figure 3.4: The phase noise of amplifiers with photodiodes and MZ EOM measurement [60].

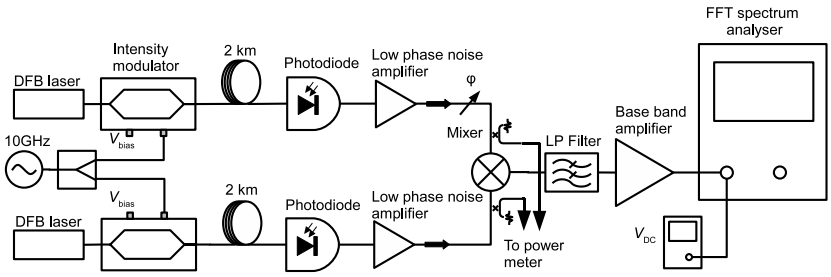

Figure 3.5: The phase noise of amplifiers with photodiodes, MZ EOM and delay lines measurement [60].

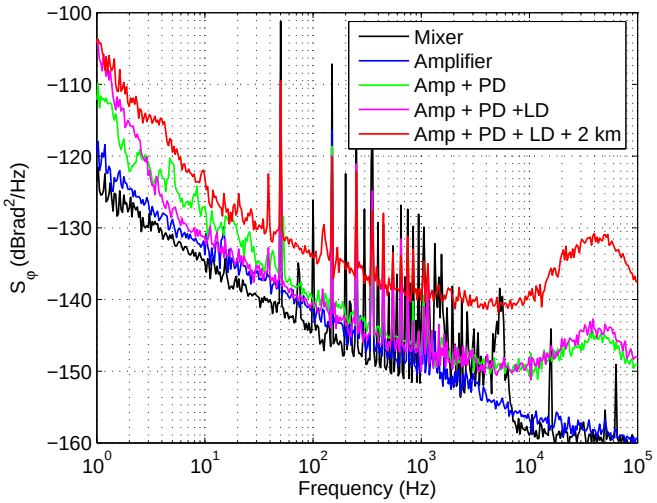

Figure 3.6: Comparison of the phase noise levels of OEO components. The black line ("Mixer") is the background phase noise of the measurement system (Fig. 3.1). The blue line ("Amp") is the phase noise of the system with the low phase noise amplifier (Fig. 3.2). The red line ("Amp + PD") is the phase noise of the system with the PIN photodiodes added to each branch (Fig. 3.3). The green line ("Amp + PD + Laser") is the phase noise of the system with the lasers (EM4) and MZ modulators included in the branches (Fig. 3.4). The brown line ("Amp + PD + 2km + Laser") is the phase noise of the system with a delay line of 2 km included in each branch.

These results can be also used to estimate the background noise of the measurement bench. As mentioned above, the OEO loop partially reproduces the phase noise measurement bench. Therefore the curve "Amp + PD + LD + 2 km" in Fig. 3.6 can be used for this purpose. This is the background noise at one measurement. To see the background noise at different numbers of measurements when applying the cross-correlation method, we apply Eq. (2.18). The result is shown in Fig. 3.7. If we could suppress the effect of the interaction of laser frequency noise and dispersion of the delay line or reduce the laser frequency noise, the background noise could be reduced by about 10 dB.

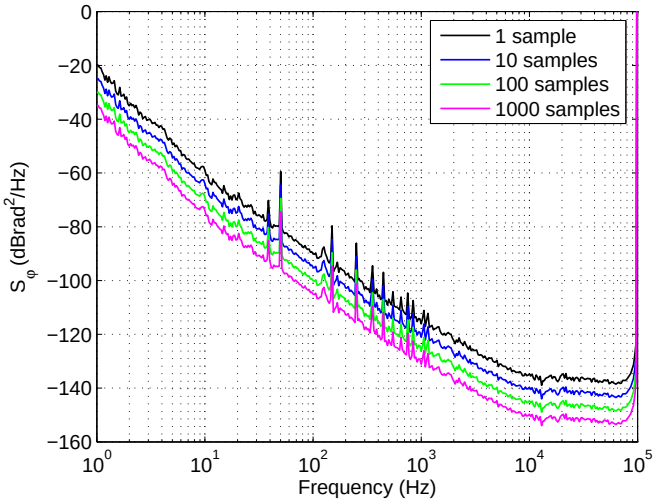

Figure 3.7: The background noise of the measurement bench at different numbers of measurements when applying the cross-correlation.

3.2 The frequency noise of DFB lasers

The scheme (see Fig. 3.8) with an asymmetric Mach-Zehnder interferometer as a frequency detector was used to measure the laser frequency noise.

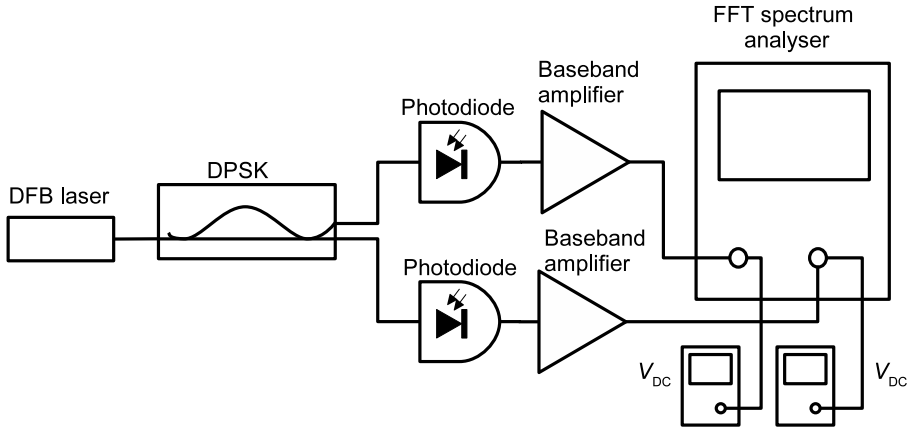

Figure 3.8: Frequency noise measurement bench [61].

Power spectral density was chosen as output of the FFT analyzer, and a correct calibration of noise could be achieved with an adequate conversion coefficient. The latter can be obtained from the analysis of the optical power transfer function of the interferometer

$$K(\nu) = \frac{1}{2} + \frac{\cos(2\pi\nu\tau_{\mathrm{D}})}{2}, \tag{3.1}$$

where τ_{D} is the differential delay of the asymmetric MZ interferometer and ν is the optical

frequency. Thus,

$$\frac{\delta K(\nu)}{\delta \nu} = -\pi \tau_{\mathrm{D}} \sin(2\pi \nu \tau_{\mathrm{D}}). \tag{3.2}$$

For a given laser wavelength, the interferometer unbalancing τ_{D} can be fine-tuned by adjusting the temperature or the laser wavelength, so that the laser-frequency detector operates as a linear detector ($\sin(2\pi\nu\tau_{\mathrm{D}}) \simeq \pm 1$). In this case the transfer function can be represented as

$$K(\nu) \approx K_0 + \delta\nu \cdot \left(\frac{\partial K(\nu)}{\partial \nu} \right)_{\nu_0}. \tag{3.3}$$

So the conversion factor for the frequency noise is

$$C_\nu = \frac{\delta \nu}{\delta V} = \frac{1}{\frac{\partial K(\nu)}{\partial \nu} P_{\mathrm{opt}} \rho R_{\mathrm{PD}} G} = \frac{1}{\pi P_{\mathrm{opt}} \tau_{\mathrm{D}} \rho R_{\mathrm{PD}} G}, \tag{3.4}$$

where $R_{\mathrm{PD}} = 50\ \Omega$ in this case. The mean voltage at the output of the amplifier is

$$V_{\mathrm{DC}} = \frac{P_{\mathrm{opt}} \rho R_{\mathrm{PD}} G}{2}. \tag{3.5}$$

Therefore the conversion factor is simplified as follows

$$C_\nu = \frac{1}{2\pi \tau_{\mathrm{D}} V_{\mathrm{DC}}}, \tag{3.6}$$

where $\tau_{\mathrm{D}} = 402.68$ ps.

Before measurement, we adjust the laser frequency so that the mean voltages of the branches are equal. This moves the operating point of the interferometer to the middle of linear part of the transfer function.

Thus, we have measured the frequency noise of EM4 laser and CQF935 laser. The results are presented in Fig. 3.9(a) and 3.10(a). The frequency noise levels at 10 Hz and 100 kHz are also shown in Fig. 3.9(b) and 3.10(b) to simplify seeing the dependence when varying the laser CW power.

As one can see, the EM4 laser has higher frequency noise than CQF935: about 10 dBMHz^2/Hz of difference in average at 10 Hz and about 8 dBMHz^2/Hz of difference in average at 100 kHz. The dependence of frequency noise on laser power for EM4 differs from the one for CQF935. The frequency noise of the EM4 increases vs. laser power and frequency noise of the CQF935 decreases vs. laser power. This difference can be caused both by difference of LD structures and by supply source characteristics (current noise). The EM4 is fed by LDC210C that typically has less than 5 μA as rms of the current noise in the range from 10 Hz to 10 MHz. The CQF935 is fed by LDC202C that typically has less than 1.5 μA as rms of the current noise in the range from 10 Hz to 10 MHz.

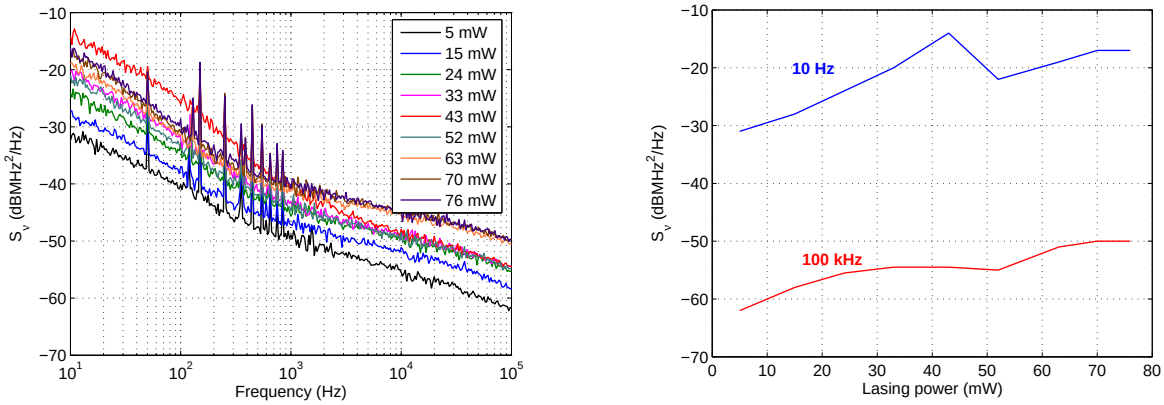

(a) (b) At 10 Hz and 100 kHz.

Figure 3.9: EM4 frequency noise [61].

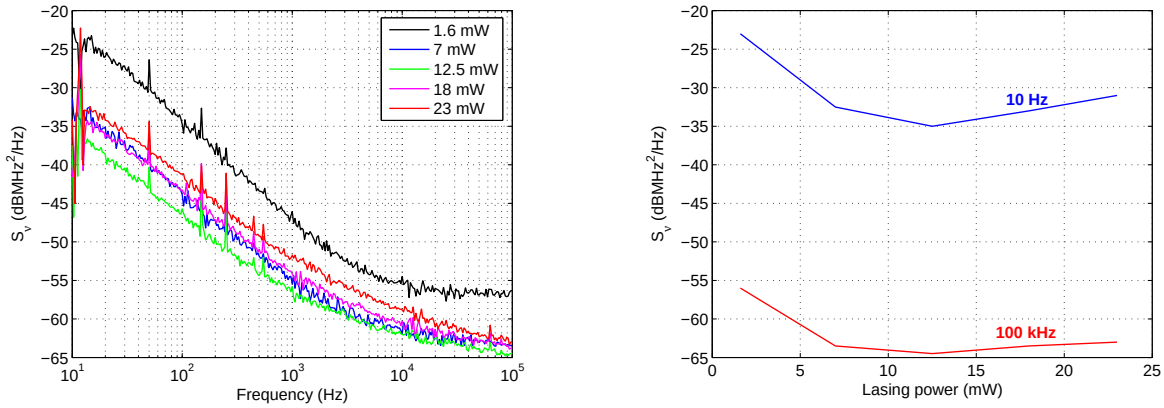

(a) (b) At 10 Hz and 100 kHz.

Figure 3.10: CQF935 frequency noise [61].

3.3 The RIN of DFB lasers

To see the contribution of DFB laser to the phase noise of OEO we should measure its relative intensity noise (RIN). The following measurement scheme (Fig. 3.11) was used to measure RIN.

In such a way we could measure RIN in spectral range up to 100 kHz. We used the cross-correlation method to eliminate the phase noise of photodiodes and amplifiers [62]. The results are presented on figures 3.12(a) and 3.12(b).

The EM4 laser is more powerful (up to 50 mW, 450 mA) than the CQF935 laser (up to 20 mW, 100 mA) but it has slightly higher RIN. The dependence of RIN on laser current is similar for both lasers.

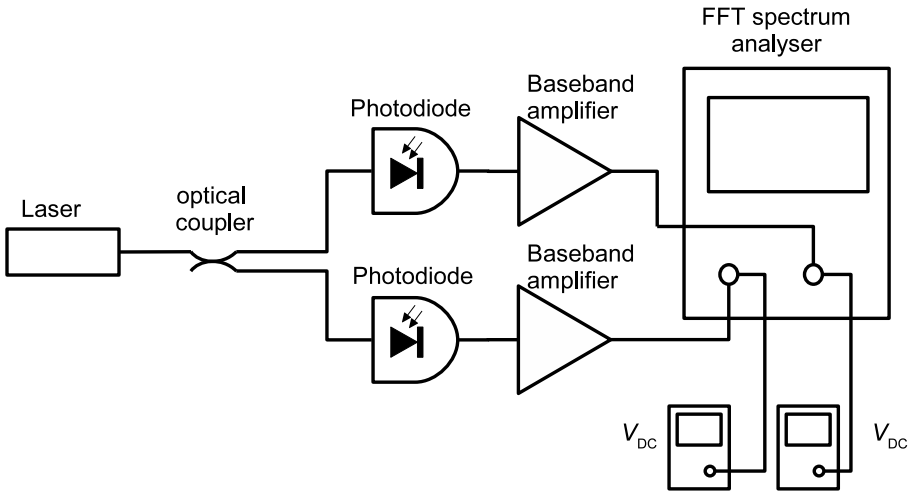

Figure 3.11: RIN measurement bench [61].

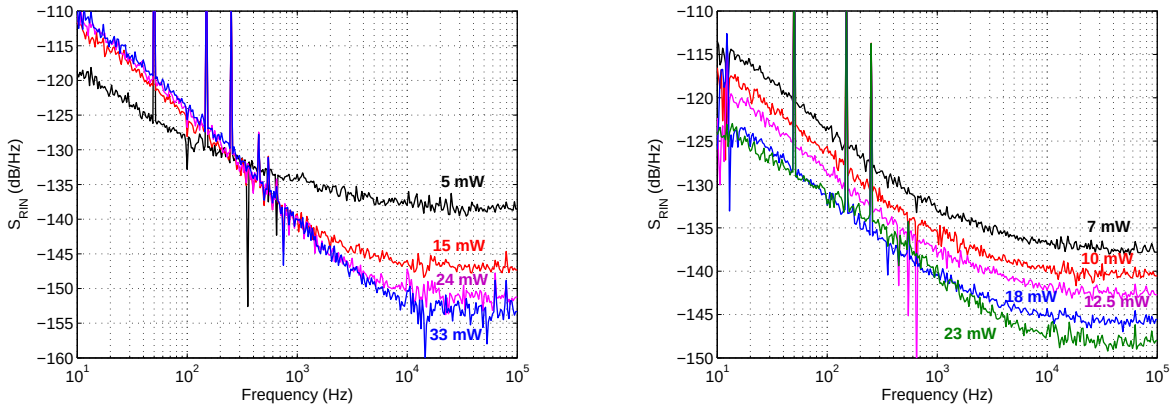

(a) Laser EM4 RIN.

(b) Laser CQF935 RIN.

Figure 3.12: Low frequency RIN [61].

3.4 Mathematical model for the OEO phase noise

Knowing the noise of the different OEO components, we can estimate the total OEO phase noise, the contribution of each component to the total phase noise, and the potential levels of phase noise using mathematical model based on the stochastic nonlinear delay differential equation (1.18). In Section 1.3 we introduced two main noise contributions in this system: the additive noise and the multiplicative noise. In the OEO configuration, we have the multiplicative noise $\eta_m(t) \ll 1$ as we will see afterwards. In Section 2.2, we modified the stochastic nonlinear delay differential equation to include the EOM modulation characteristic. Here, we will use the equation with the noise terms and deduce the OEO phase noise spectrum expression.

To avoid the integral term of Eq. (2.5) which is complicated to manage analytically,

it is mathematically convenient to use the intermediate integral variable

$$y(t) = \int_{t_0}^{t} x(s)\, ds = \frac{1}{2}\mathcal{B}(t)\, e^{j\omega_0 t} + \frac{1}{2}\mathcal{B}^*(t)\, e^{-j\omega_0 t}\,, \tag{3.7}$$

which is also nearly sinusoidal with a zero mean value. Using Eqs. (1.16), (1.17), and (2.5), it can be shown that the slowly-varying amplitude $\mathcal{B}(t)$ obeys the stochastic equation

$$\begin{aligned} &\{\ddot{\mathcal{B}} + (\Delta\omega + 2j\omega_0)\dot{\mathcal{B}} + j\omega_0\,\Delta\omega\,\mathcal{B}\}e^{j\omega_0 t} + \text{c.c.} \\ &= -2\Delta\omega\gamma\,[1+\eta_{\rm m}(t)]\ \left[\frac{1}{2}e^{j\omega_0(t-\tau_{\rm d})}e^{j\psi_{\tau_{\rm d}}} + \text{c.c.}\right] \\ &\times \mathrm{J}_1[2|\dot{\mathcal{B}}_{\tau_{\rm d}} + j\omega_0\mathcal{B}_{\tau_{\rm d}}|] + 2\Delta\omega\left[\frac{1}{2}\zeta_{\rm a}(t)e^{j\omega_0 t} + \text{c.c.}\right]\,, \end{aligned} \tag{3.8}$$

where c.c. stands for the complex conjugate of the preceding term. As a consequence of a slowly varying envelope, we can assume $|\ddot{\mathcal{B}}| \ll \Delta\omega|\dot{\mathcal{B}}|$ and $|\dot{\mathcal{B}}| \ll \omega_0|\mathcal{B}|$; the relationship $x(t) = \dot{u}(t)$ therefore gives $\mathcal{A} \simeq i\omega_0\mathcal{B}$, so that we can finally derive from Eq. (3.8) the following stochastic equation for the slowly varying envelope $\mathcal{A}(t)$

$$\begin{aligned} \dot{\mathcal{A}} \ &= \ -\mu e^{i\vartheta}\mathcal{A} + 2\gamma\mu e^{i\vartheta}\,[1+\eta_{\rm m}(t)]\ \mathrm{Jc}_1[2|\mathcal{A}_{\tau_{\rm d}}|]\mathcal{A}_{\tau_{\rm d}} \\ &\quad +\mu e^{i\vartheta}\zeta_{\rm a}(t)\,, \end{aligned} \tag{3.9}$$

where $\mathrm{Jc}_1(x) = \mathrm{J}_1(x)/x$ is the first order *Bessel cardinal* function of the first kind. The phase condition has been set to $e^{-j\omega_0\tau_{\rm d}} = -1$, so that the dynamics of interest is restricted to the case $\gamma \geq 0$. The key parameters of this equation are

$$\mu = \frac{\Delta\omega/2}{\sqrt{1+(1/2Q)^2}} \ \text{ and } \ \vartheta = \arctan\left[\frac{1}{2Q}\right]\,, \tag{3.10}$$

where $Q = \omega_0/\Delta\omega = 200$ is the quality factor of the RF filter. Since $Q \gg 1$, we may simply consider that $\mu \simeq \Delta\omega/2$ and $\vartheta \simeq 1/2Q$. The complex factor $\mu e^{i\vartheta}$ is a kind of "filter effect", which can be simply equated to the half-bandwidth $\Delta\omega/2$ when the Q-factor of the filter is sufficiently high.

When $\gamma > 1$, the stationary noise free amplitude $A_0 = |\mathcal{A}_0|$ of the microwave obeys the nonlinear algebraic equation $\mathrm{Jc}_1[2|\mathcal{A}_0|] = 1/(2\gamma)$. Linearizing Eq. (3.9) around this solution yields the following equation [63]

$$\dot{\mathcal{A}} = -\mu e^{i\vartheta}\mathcal{A} + \mu e^{i\vartheta}[1+\eta_{\rm m}(t)]\mathcal{A}_{\tau_{\rm d}} + \mu e^{i\vartheta}\zeta_{\rm a}(t)\,. \tag{3.11}$$

Using the Itô rules of stochastic calculus [63], we derive the following time-domain equation for the phase dynamics

$$\dot{\psi} = -\mu(\psi - \psi_{\tau_{\rm d}}) + \frac{\mu}{2Q}\eta_{\rm m}(t) + \frac{\mu}{|\mathcal{A}_0|}\xi_{{\rm a},\psi}(t)\,, \tag{3.12}$$

where $\xi_{\mathrm{a},\psi}(t)$ is a real Gaussian white noise of correlation $\langle \xi_{\mathrm{a},\psi}(t)\xi_{\mathrm{a},\psi}(t')\rangle = 2D_{\mathrm{a}}\delta(t-t')$ (same variance as $\xi_{\mathrm{a}}(t)$). We can add $\varsigma_\psi(t)$ to take into account contribution of laser frequency noise, amplifier phase noise, etc.

$$\dot{\psi} = \mu\left(\psi_{\tau_{\mathrm{d}}} - \psi + \varsigma_\psi(t) + \frac{\eta_{\mathrm{m}}(t)}{2Q} + \frac{\xi_{\mathrm{a},\psi}(t)}{|\mathcal{A}_0|}\right), \tag{3.13}$$

We can use Eq. (3.13) to obtain the Fourier spectrum $\Psi(\omega)$ of the phase $\psi(t)$. The resulting power density spectrum is as follows [63]

$$|\Psi(\omega)|^2 = \left|\mu\frac{\frac{\tilde{\eta}_{\mathrm{m}}(\omega)}{2Q} + \frac{\sqrt{2D_{\mathrm{a}}}}{|\mathcal{A}_0|} + \varsigma_\psi(\omega)}{i\omega + \mu\left[1 - e^{-i\omega\tau_{\mathrm{d}}}\right]}\right|^2 . \tag{3.14}$$

This equation should be modified to take into account statistical independence of the noise processes. The autocorrelation function of sum of random processes $x_1(t), ..., x_n(t)$ can be expressed as

$$R(\tau) = \sum_{i=1}^{n}\mathbb{E}\left\{x_i(t)x_i(t+\tau)\right\} + 2\sum_{i<j}\mathbb{E}\left\{x_i(t)x_j(t+\tau)\right\} . \tag{3.15}$$

In case of statistical independence of the processes, the second sum equals zero. Therefore supposing the statistical independence of the phase noise processes and taking into account the Wiener-Khinchin theorem, we can rewrite Eq. (3.14) in the following way

$$|\Psi(\omega)|^2 = \mu^2\frac{\left|\frac{\tilde{\eta}_{\mathrm{m}}(\omega)}{2Q}\right|^2 + \left|\frac{\sqrt{2D_{\mathrm{a}}}}{|\mathcal{A}_0|}\right|^2 + |\varsigma_\psi(\omega)|^2}{\left|i\omega + \mu\left[1 - e^{-i\omega\tau_{\mathrm{d}}}\right]\right|^2} . \tag{3.16}$$

To consider applicability of the Bode integral principle to this model, we deduce the sensitivity functions for the multiplicative noise

$$\varepsilon_{\mathrm{m}}(s) = \frac{\frac{\mu}{2Q}}{s + \mu\left[1 - e^{-js\tau_{\mathrm{d}}}\right]} , \tag{3.17}$$

and for the additive noise and the phase noise of components

$$\varepsilon_{\mathrm{a}}(s) = \frac{\mu}{s + \mu\left[1 - e^{-js\tau_{\mathrm{d}}}\right]} . \tag{3.18}$$

We can not apply the Bode integral principle to these sensitivity functions because $\lim_{s\to\infty}\ln|\varepsilon_{\mathrm{m}}(s)| \neq 0$ and $\lim_{s\to\infty}\ln|\varepsilon_{\mathrm{m}}(s)| \neq 0$. But they can be used to characterize the system sensitivity with respect to the noises.

The diffusion constant D_a can be calculated using the characteristics of OEO components. The output power of the amplifier caused by RIN, thermal noise, and shot noise can be expressed as

$$P_\mathrm{o} = \left[N_\mathrm{RIN} I_\mathrm{PD}^2 R_\mathrm{eq} + \mathcal{F} k T_0 + 2qI_\mathrm{PD} R_\mathrm{eq}\right] \frac{G\Delta F}{2} \tag{3.19}$$

where G is the amplifier gain, $\mathcal{F}$ is the noise figure of amplifier (6 dB at 298 K), $T_0 = 290$ K is the reference temperature, k is the Boltzmann constant, q is the electron charge, I_PD is the photodiode current, and R_eq is the equivalent load impedance of the photodiode.

D_a can be determined [63] as

$$D_\mathrm{a} = \frac{P_\mathrm{o}\pi R}{4V_{\pi\mathrm{RF}}^2 \Delta F}\,, \tag{3.20}$$

where R is the output impedance (in our case, $R = 50\ \Omega$) .

Equation (3.11) also allows to estimate the AM noise of OEO. For this purpose, we linearize it in the following way

$$\dot{\mathcal{A}} = -\mu e^{i\vartheta}\mathcal{A} + \mu e^{i\vartheta}\mathcal{A}_{\tau_\mathrm{d}} + \mu e^{i\vartheta}\eta_\mathrm{m}(t)\,|A_0| + \mu e^{i\vartheta}\zeta_\mathrm{a}(t)\,. \tag{3.21}$$

Then we apply Fourier transform and express the power density spectrum of AM noise.

$$|\tilde{\mathcal{A}}(\omega)|^2 = \frac{\mu^2\,|\eta_\mathrm{m}(\omega)A_0|^2 + 4\mu^2 D_\mathrm{a}}{|j\omega e^{-j\vartheta} + \mu(1 - e^{-j\omega\tau_\mathrm{d}})|^2}\,. \tag{3.22}$$

It should be noted that this power density spectrum is derived without taking into account the gain compression, which significantly reduces AM noise. But it can be used to discuss the possible influence of AM noise on phase noise measurement at some operation modes of OEO.

3.5 Contribution to the phase noise of OEO

Using the equations introduced in the previous section, we can estimate different phase noise contributions to the total phase noise of OEO.

The low phase noise AML amplifiers, which we use in experiments, can be characterized by the power law coefficient $b_{-1} = -128$ dBrad^2/Hz. It is extrapolated from phase noise values in the device data sheet. The typical flicker coefficient of a InGaAs p-i-n photodetector is of 10^{-12} rad^2/Hz (-120 dBrad^2/Hz) [64, 65, 66]. The passive components have supposedly lower magnitudes of the phase noise.

The low frequency RIN of lasers can be represented by multiplicative noise $\eta_\mathrm{m}(\omega)$ in Eq. (3.14) since the MZ modulator produces multiplication of optical and microwave

signals. In the most cases, the quality factor Q of the RF filter is high. In our case $Q = 200$ and the measured RIN is divided by $2Q = 400$ (-52 dB) when we calculate the phase noise spectral density according to Eq. (3.16). If we apply this to the above shown RIN levels, we can see that the low frequency RIN can be neglected regarding the phase noise, but not regarding the AM noise since it does not comprise a $1/2Q$ factor for this noise contribution. The EM4 laser RIN for microwave frequencies (10 GHz in our case) is about -159 dB/Hz and the CQF935 laser RIN is about -165 dB/Hz according to the laser data sheets.

To calculate the phase noise caused by the laser frequency noise over $L = 4$ km of optical fiber SMF-28e, we used the following conversion factor

$$C_\psi = \frac{\omega_0 D_\lambda L \lambda_0^2}{c\, n}, \tag{3.23}$$

where c is the speed of light in vacuum, n is the optical fiber refraction index (1.46).

Equation (3.14) is used to estimate the OEO phase noise PSD, taking into account the laser RIN at 10 GHz, its low frequency RIN, its optical frequency noise, the thermal white noise, and the photodiode shot noise.

We will consider the phase noise of two variants of the classical OEO architecture shown in Figs. 3.13 and 3.14. The first variant can be used with the CQF935 laser and with the EM4 laser at the low power mode

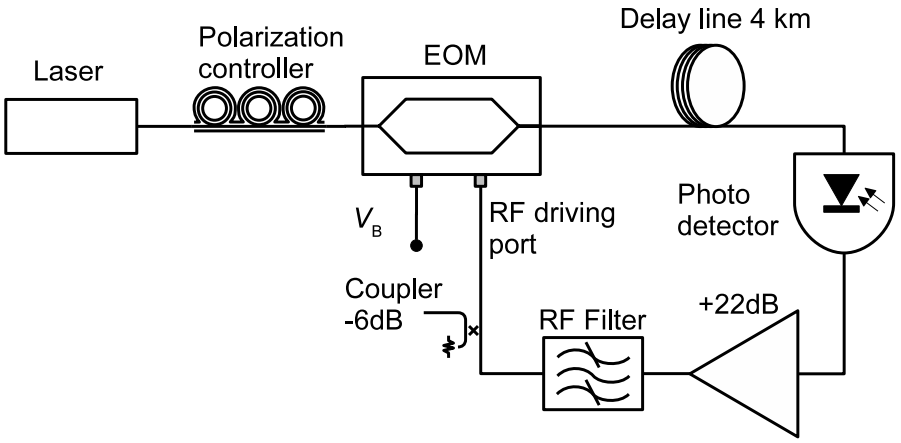

Figure 3.13: An OEO with one low phase noise amplifier ($G = 22$ dB).

The comparison of all mentioned phase noise contributions is shown on figures 3.15(a) - 3.17(b). The "LD RIN" curve is the microwave frequency LD RIN, "Amp white" is the thermal white noise including the amplifier, "PD shot" is the photodiode shot noise. These 3 terms are included in Eq. (3.19). The "LD low freq RIN" curve is the LD low frequency RIN. The "Amp flicker" curve is the flicker phase noise of one amplifier. The "PD flicker" curve is the flicker phase noise of photodiode. The "LD freq noise" curve is the laser frequency noise in interaction with the fiber dispersion.

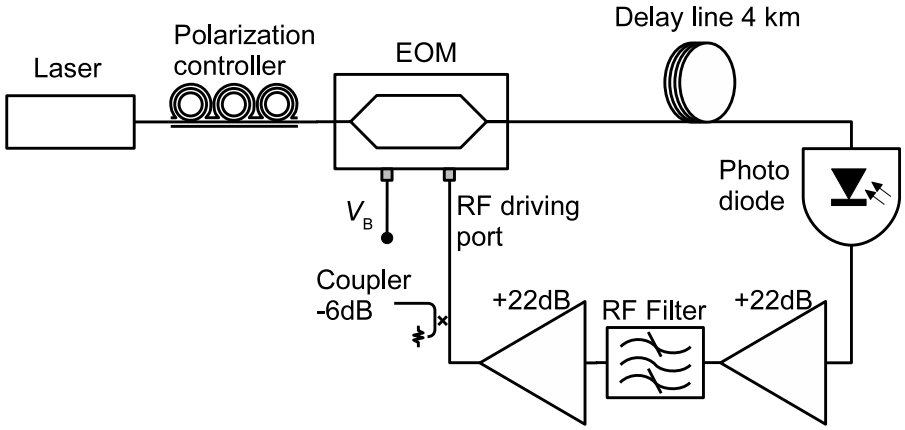

Figure 3.14: An OEO with two low phase noise amplifiers ($G = 44$ dB).

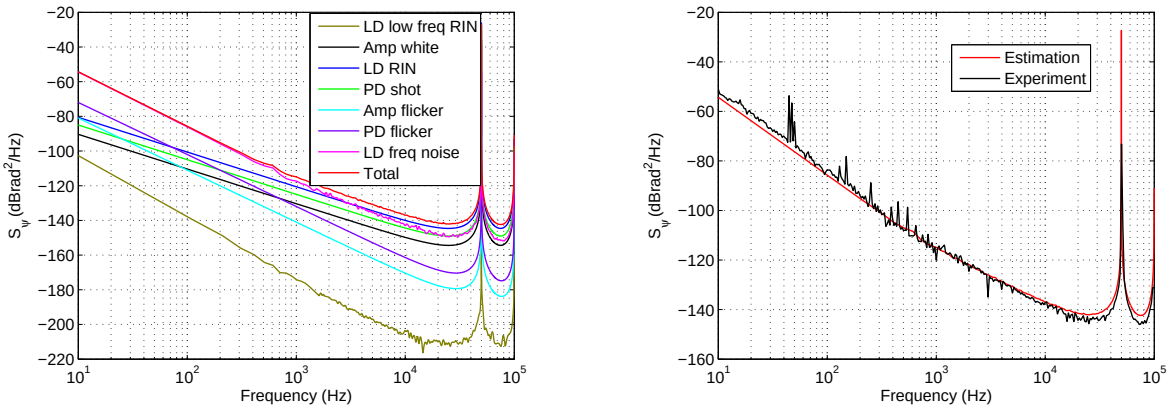

(a) (b)

Figure 3.15: The phase noise of OEO with EM4 laser at laser power 33 mW. Two low phase noise microwave amplifiers ($G = 44$ dB) are used.

We see good correspondence of prediction and experiment in the figures. The model also conforms well to the Leeson effect [67] since we can observe the conversion of the components phase noise to the OEO phase noise by the factor $(1 + (\nu_0/(2Q))^2/f^2)$.

The case, which is shown in Fig. 3.16(a) looks most promising regarding the potential of decreasing the OEO phase noise. Let's consider this variant in detail. As we can see, most of the phase noise is generated by the laser-frequency noise and delay line dispersion interaction. The possible solution is to use dispersion shifted optical fiber with zero dispersion at the laser wavelength in order to eliminate this phase noise component. It should considerably decrease the phase noise level in case of using the EM4 laser and one amplifier architecture. We can possibly achieve almost -160 dBrad^2/Hz at the frequency of about 25 kHz and -72 dBrad^2/Hz at the frequency of about 10 Hz (Fig. 3.16(a)). Further decrease of phase noise in the region lower 200 Hz seems possible using a velocity matched distributed photodetector (VMDP) and using a feedforward amplifier that would

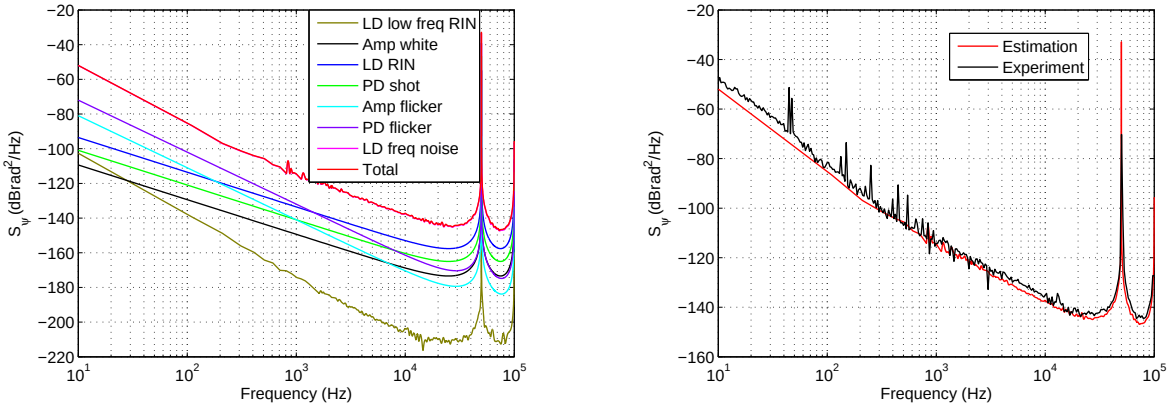

(a) (b)

Figure 3.16: The phase noise of OEO with EM4 laser at laser power 70 mW. One low phase noise microwave amplifier ($G = 22$ dB) is used.

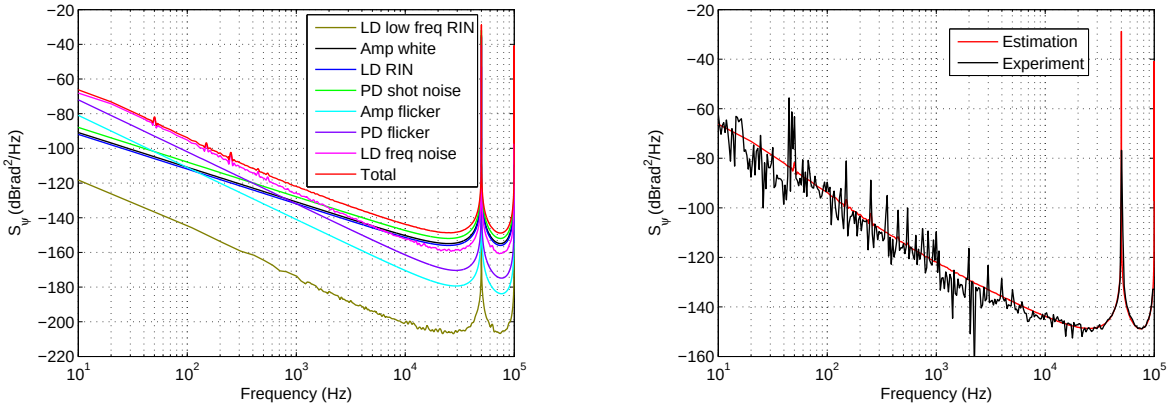

(a) (b)

Figure 3.17: The phase noise of OEO with CQF935 laser at laser power 23 mW. Two low phase noise microwave amplifiers ($G = 44$ dB) are used.

provide lower phase noise. These issues will be discussed in the next chapter. In the higher frequencies region, the next limiting factor is the high frequency RIN of laser. After reducing the high-frequency RIN, we expect that the next dominant factor will be the shot noise. Thus the next limiting level is, most probably, the level created by white noise. Since it is inversely proportional to the oscillation amplitude (see Eq. (3.16)), it can be decreased by increasing the oscillation power. This factor also allows to decrease AM noise as we will see further. But this possibility is very limited.

The experimental curve in Fig. 3.17(b) shows the best result obtained in our experiments: -66 dBrad^2/Hz at 10 Hz, -143 dBrad^2/Hz at 10 kHz, -149 dBrad^2/Hz at 25 kHz. As it follows from the analysis of the different phase noise contributions, this result is achieved mainly due to the low frequency noise of the JDSU CQF935 laser. Further

decrease of the phase noise in the given configuration is difficult because other noise components (amplifier noise figure, photodiode shot noise, laser high frequency RIN) have almost the same level in the range 1 - 100 kHz and they should be decreased simultaneously.

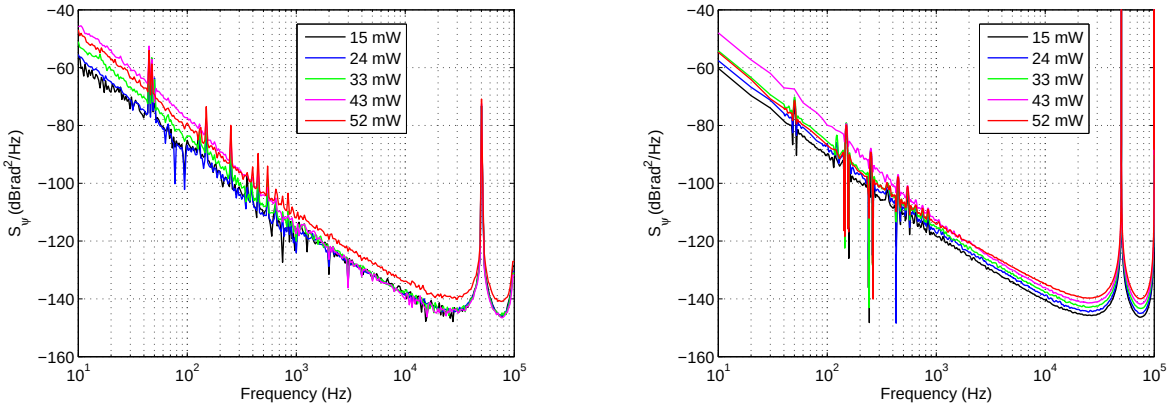

(a) Measured (b) Calculated

Figure 3.18: The phase noise of OEO with EM4 laser at different laser power. Two low phase noise microwave amplifiers ($G = 44$ dB) are used.

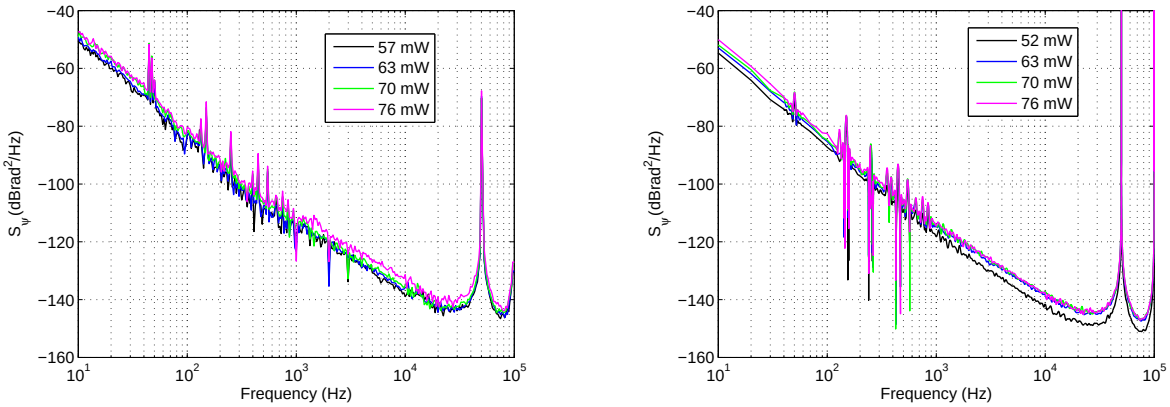

(a) Measured (b) Calculated

Figure 3.19: The phase noise of OEO with EM4 laser at different laser power. One low phase noise microwave amplifier ($G = 22$ dB) is used.

The OEO phase noises at different laser powers are shown in Figs. 3.18(a) – 3.20. As we can see, we have good correspondence of prediction and experiment in all cases except the cases of low power levels of the CQF935 laser (Fig. 3.20(a), 7 mW and 12 mW). In latter ones, random-walk of frequency noise appears in the region of 100 Hz – 10 kHz. This noise is usually attributed to environmental instabilities (mechanical shock, vibration, temperature, or other environmental effects). In this experiment, it manifests at low oscillation power only. Another possible reason of this phenomenon is the AM noise influence on the phase noise measurement and it will be considered in the Section 3.7.

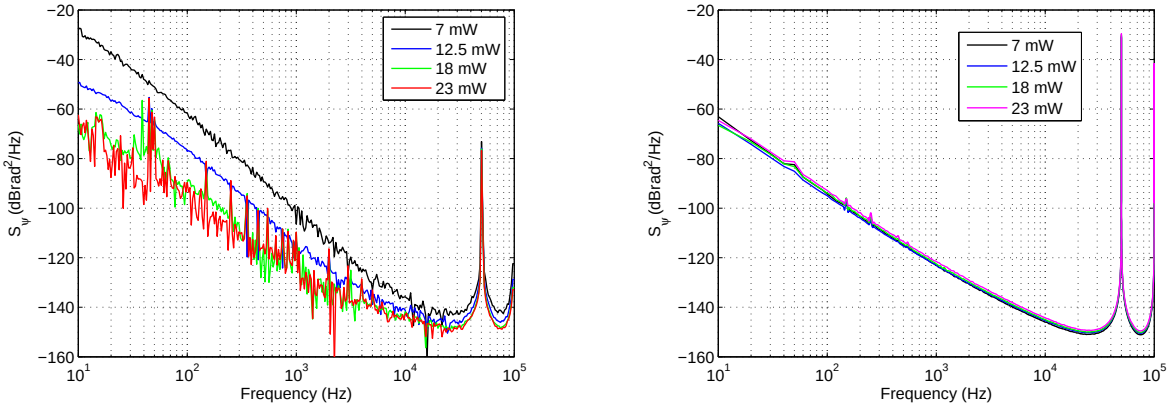

(a) Measured (b) Calculated

Figure 3.20: The phase noise of OEO with CQF935 laser at different laser power. Two low phase noise microwave amplifiers ($G = 44$ dB) are used.

3.6 The spurious peaks

The OEO phase noise model allows also to estimate level and linewidth of the spurious peaks. Comparing theoretical and experimental values is an interesting test for the discussion of our approach through nonlinear stochastic delay equation. According to [63], the spurious peaks height relatively to the phase noise floor can be estimated by

$$\Delta|\Psi_n|^2_{\mathrm{dB}} = 10\log\left[\frac{\Delta F\,\tau_{\mathrm{d}}}{n}\right]^4 = 10\log\left[\frac{\nu_0\,\tau_{\mathrm{d}}}{Q\,n}\right]^4 \tag{3.24}$$

and the spurious peaks width by

$$\Delta f_n = \frac{2}{\pi}\frac{n^2}{(\Delta F)^2{\tau_{\mathrm{d}}}^3}\,. \tag{3.25}$$

For $\nu_0 = 10$ GHz and $\tau_{\mathrm{d}} = 20$ μs, $\Delta|\Psi_n|^2_{\mathrm{dB}} = 212\,\mathrm{dB} - 40\log Q - 40\log n$. For $\Delta F = 50$ MHz and $n = 1$ it gives $\Delta|\Psi_1|^2_{\mathrm{dB}} = 120$ dB and $\Delta f_1 = 32$ mHz.

We have measured the first spurious peak and the noise floor with the same parameters in order to verify the model. The results are presented in Figs. 3.21(a) and 3.21(b).

Since the spurious peak is very narrow, the measurement was repeated with different frequency span and resolution[1]. The peak represented in high resolution (1.6 mHz) has distorted shape. It was probably caused by some instability during the measurement process. We will consider the higher narrower peak since it is closer to the Lorentzian shape. The noise floor is -143 dBrad^2/Hz and the peak level is -25.5 dBrad^2/Hz. So the peak height is 117.5 dB, which is close to the predicted one (120 dB). The peak width is about 40 mHz, which is also close to the predicted one (32 mHz).

[1]Generally, this is called "bandwidth" or "resolution bandwidth" (RBW) on the front panel of analyzers.

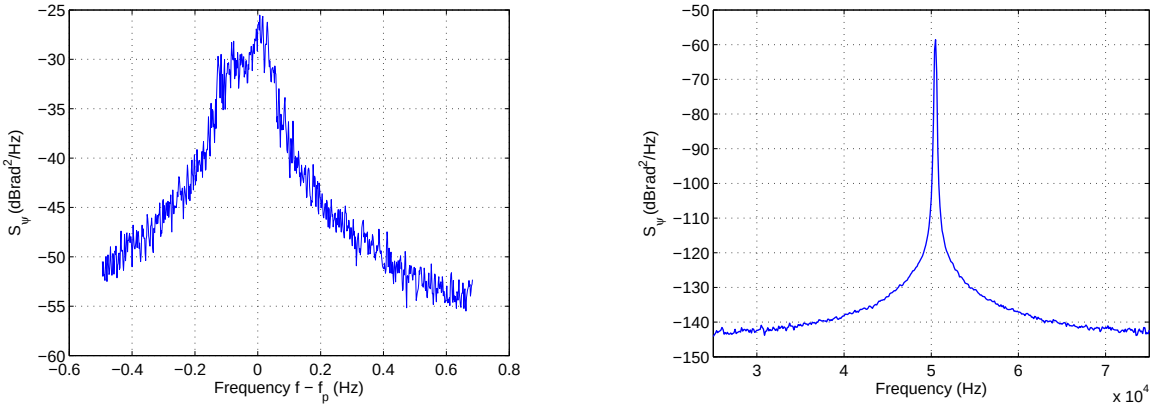

(a) (b)

Figure 3.21: The first spurious peak and the noise floor measured. $f_{\mathrm{p}} = 50594.3544$ Hz

Therefore we can use the OEO phase noise model for estimating the spurious peaks properties as well, and the very concordance between experiment and theory is a very positive argument supporting the adopted model.

Using Eq. (1.42), we can estimate the spurious peak time jitter contribution by

$$\sigma = \frac{1}{2\pi\nu_0}\sqrt{|\Psi_n|^2\Delta f_n} = \sqrt{\frac{1}{4\pi^2\nu_0^2}|\Psi_{\mathrm{floor}}|^2\Delta|\Psi_n|^2\Delta f_n}. \tag{3.26}$$

And using Eqs. (3.24) and (3.25) for $\Delta|\Psi_n|^2$ and Δf_n respectfully we have

$$\sigma = |\Psi_{\mathrm{floor}}|\sqrt{\frac{1}{4\pi^2\nu_0^2}\left(\frac{\Delta F\,\tau_{\mathrm{d}}}{n}\right)^4\left(\frac{2}{\pi}\frac{n^2}{(\Delta F)^2{\tau_{\mathrm{d}}}^3}\right)} = \frac{1}{nQ}|\Psi_{\mathrm{floor}}|\sqrt{\frac{\tau_{\mathrm{d}}}{2\pi^3}}\,. \tag{3.27}$$

We have estimated the first spurious peak time jitter contribution for $|\Psi_{\mathrm{floor}}|^2 = -150$ dBrad^2/Hz at different Q. The result is shown in Fig. 3.22. The increase of Q is very effective up to about 1000 and then its efficiency significantly decreases.

3.7 The influence of AM noise on measurement indications

As it was mentioned in the end of Section 3.5, there are significant discrepancies between experimental and theoretical results in Fig. 3.20. At the power of 7 mW and 12.5 mW, the phase noise is higher than predicted. Additionally, the presence of a 40 dB/decade slope makes one think that there are other noise phenomena not accounted for in the model. During some measurements, we observed a difference of about 12 dB between the

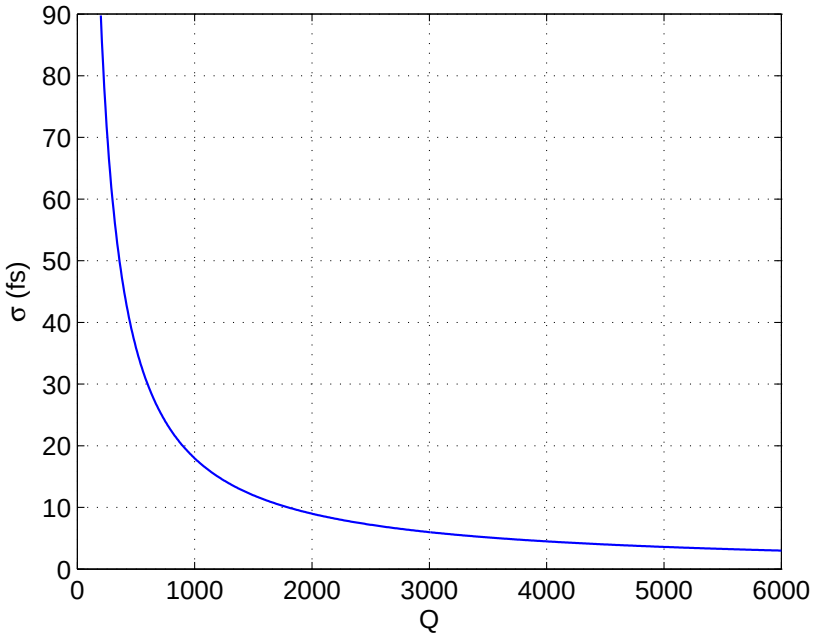

Figure 3.22: The time jitter vs Q at noise floor -150 dBrad^2/Hz.

two channels of the FFT analyzer. Of course, we expect equal indications of the channels because of symmetry. This suggests that the spurious indications are caused by AM noise. To verify this, we measured the phase noise spectrum of a 10 GHz signal with 4% AM by a square wave of 20 Hz. A square wave produces several spectrum peaks (harmonics). This allows to obtain AM sensitivity dependence on frequency by comparing their levels with theoretical. The signal was fed to the input of the measurement bench from Anritsu 68347C synthesizer at three different power levels: 4 dBm, 6 dBm, 8 dBm. Notice that the gain compression of input amplifiers starts at 4 dBm and saturation is observed at 6 dBm. The results are presented in Figs. 3.23(a) – 3.23(c).

The phase noise spectrum of the synthesizer is shown in Fig. 3.23. Comparing the two channels, we see that the phase noise levels are almost equal, but the peaks due to AM are different. We can see also the parts where the phase noise level is lower than the noise floor of single channels, i.e. where cross-correlation shows up (the green line lower than blue and red ones). The peaks of the square wave spectrum are observed at 20 Hz, 60 Hz, 100 Hz, 140 Hz, and 180 Hz. The difference between the peaks indicated by different channels is about 12 dBrad^2/Hz. This can be explained by different degree of asymmetry of the double balanced mixers that produces the AM noise sensitivity. It should be noted that the AM sensitivity decreases vs. frequency, because the peaks decrease with a higher rate than the ones of the square wave spectrum and it will be shown afterwards.

For small signals, the channels can be considered linear. Therefore the transfer function of channels regarding AM can be estimated. For this purpose, we calculate frequency

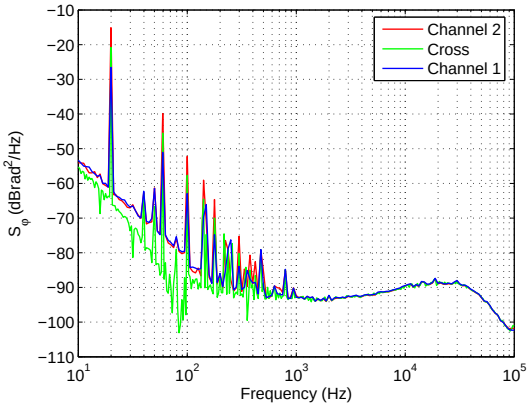

(a) 4 dBm

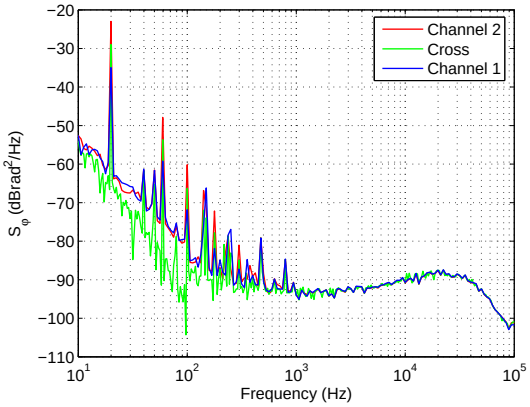

(b) 6 dBm

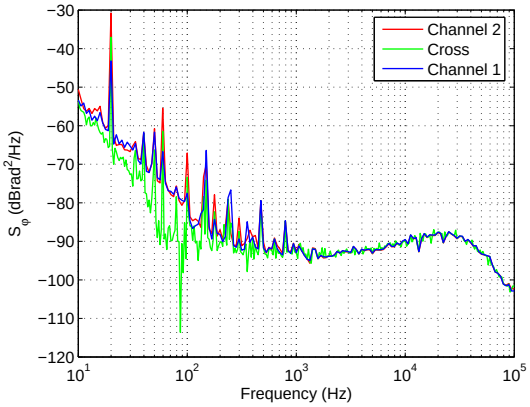

(c) 8 dBm

Figure 3.23: The phase noise spectrum of the 10 GHz signal at different power with AM by square wave of 20 Hz and 10 mV.

components of a sine wave modulated by a square wave.

$$\begin{aligned} s(t) &= A_0 \left[1 + \frac{4\,M}{\pi} \sum_{\text{odd}\, n=1}^{\infty} \frac{1}{n} \sin(n\omega_1 t)\right] \sin(\omega_0 t) \\ &= A_0 \sin(\omega_0 t) + \frac{2\,A_0\,M}{\pi} \sum_{\text{odd}\, n=1}^{\infty} \frac{1}{n} \left[\cos((\omega_0 - n\omega_1)t) - \cos((\omega_0 + n\omega_1)t)\right], \end{aligned} \tag{3.28}$$

where A_0 is the carrier amplitude, M is the modulation index. The average power is

$$\overline{s^2(t)} = \frac{A_0^2}{2} + \frac{4\,A_0^2\,M^2}{\pi^2} \sum_{\text{odd}\, n=1}^{\infty} \frac{1}{n^2}. \tag{3.29}$$

Then using the measured peaks $S_{\varphi\,\text{meas}}(\omega_n)$ corresponding to the square wave harmonics and the average power components corresponding to them, we determine values of the transfer function of the measurement system for AM at the harmonics frequencies in the

following way

$$|H_{\mathrm{AM}}(\omega)|^2 = \frac{(\mathrm{PSD})_{\mathrm{out}}\mathrm{BW}}{(\mathrm{PS})_{\mathrm{in}}}\,. \tag{3.30}$$

where $(\mathrm{PSD})_{\mathrm{out}}$ is the output PSD, BW is the bandwidth of analyzer digital filter per spectrum line, and $(\mathrm{PS})_{\mathrm{in}}$ is the input power spectrum.

In the logarithmic resolution mode, bandwidth depends on frequency as $\mathrm{BW}(f) = f(10^{1/N} - 1)$, where $N = 80$ is the number of lines per decade. Therefore

$$|H_{\mathrm{AM}}(\omega_n)|^2 = \frac{\pi\, S_{\varphi\,\mathrm{meas}}(\omega_n)\omega_n(10^{1/N} - 1)}{8\,\pi\, A_0^2\, M^2}\,. \tag{3.31}$$

This experimental transfer function for AM at different levels of carrier power is shown in Fig. 3.24. The unit is dBrad/V because it relates AM signal in $\mathrm{dBV}^2/\mathrm{Hz}$ to the

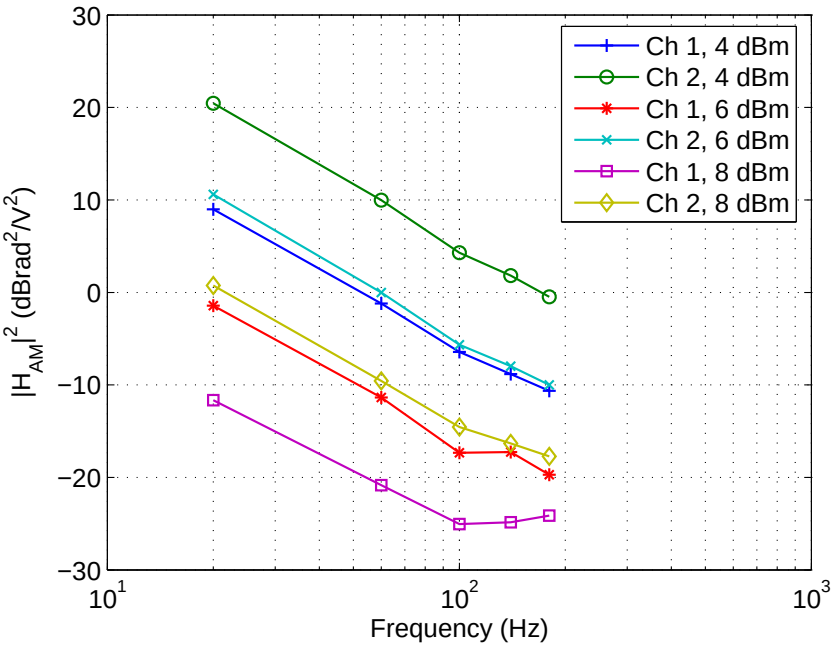

Figure 3.24: The transfer function of the measurement system for AM at different levels of carrier power.

indications in $\mathrm{dBrad}^2/\mathrm{Hz}$. The slope is about -23 dB/decade. It should be noted that the delay line contribution (see Eq. (2.11)) is included, giving an additional -20 dB/decade slope. This increases the transfer function at low frequencies. We can see also that the gain compression decreases $H(\omega)$ at increase of the carrier power.

In order to estimate the OEO AM noise indications, we calculate the OEO AM noise PSD with Eq. (3.22) taking into account that $x(t) = \pi V(t)/2V_\pi$ for CQF935 laser at

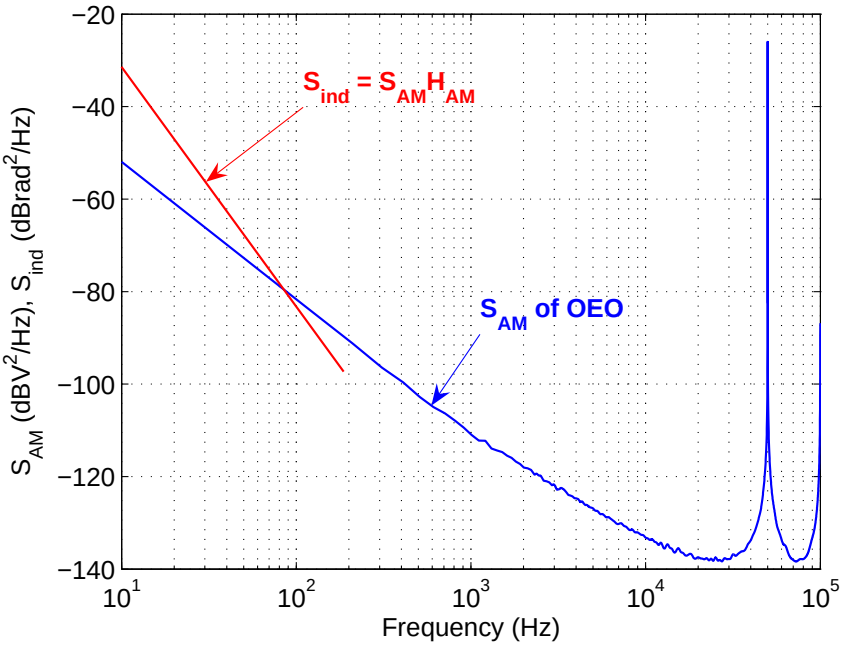

Figure 3.25: The OEO AM noise PSD.

7 mW and apply the transfer function of the measurement system for AM at 4 dBm. They are shown in Fig. 3.25. It doesn't correspond exactly to the curve for 7 mW for low frequencies in Fig. 3.20 but it shows that AM noise can appear in the phase noise measurement results. Perhaps some other AM noise emerged during the measurements. And it can require additional study. But it is evident that we can use the difference between channel indications as an indicator of AM noise presence in measurement data. It is also evident that oscillator should be run at the microwave power when there is highly expressed amplitude limiting factor due to either the amplifier saturation, either the MZ EOM operation mode, or some other effect. When OEO runs at the 7 mW power of the CQF laser, there is small gain compression in the OEO amplifier or in the MZ EOM that limits oscillation amplitude but it is not enough to significantly decrease AM noise.

3.8 Conclusion

The most significant OEO internal phase-noise sources are considered together with their influence on the output noise. The measured phase noise of some OEO components are discussed. The methods for the measurement of the laser frequency-noise and low-frequency RIN are introduced, and the measurement results are discussed. The contribution of different components to the total OEO phase noise is estimated using our mathematical model based on the stochastic nonlinear delay differential equation. The laser frequency noise combined with the fiber dispersion is found as a major source of phase noise in the

OEO. The model is compared to the measured phase noise. In most cases, we found good agreement between model and experiment. The model also conforms well to the Leeson effect [67]. The best result of OEO phase noise obtained in our experiments is: -66 dBrad^2/Hz at 10 Hz, -143 dBrad^2/Hz at 10 kHz, -149 dBrad^2/Hz at 25 kHz. It is not far from the best oscillators of the same type (for example, OEWaves: -77 dBrad^2/Hz at 10 Hz, -154 dBrad^2/Hz at 10 kHz).

The influence of AM noise on the phase noise measurement is shortly discussed since it can affect measurement results at some conditions.

In the next chapter, we will consider some architectures and methods improving the OEO phase noise performance, based on results shown here.

Chapter 4

Modified OEO architectures for reducing the phase noise

In the previous chapter, we have considered the phase noise contribution of the OEO components. After optimizing the components, noise reduction techniques can be employed to further reduce the noise. Among them are the feedforward amplifier (FFA), the Pound discriminator [68], the high-Q discriminator cavity (external or internal) [69]. The latter can be further improved by the carrier suppression technique [70]. The techniques of using high-Q cavity discriminator (including Pound discriminator) is not suitable to the OEO because it works only at one frequency, or at a set of frequencies, while the main appeal of the OEO is its tunability in small steps equal to the modes of the delay. The feedforward amplifier fits well the delay line OEO architecture. Another method proposed by Yao and Maleki [71], uses multiple loops to reduce the spurious peaks.

In this chapter, we will analyse the following noise-reduction techniques, some of which are new in the domain of optoelectronic oscillators:

- The regenerative amplifier;
- The multiloop architecture;
- The architecture with a feedforward amplifier and a velocity matched distributed photodetector (VMDP).

The first two architectures modify the sensitivity of OEO to noise. The third one has the purpose of reducing the flicker noise of amplifier and photodiode.

4.1 The architecture with a regenerative amplifier

The peaks of spurious modes in the phase noise power spectral density produced by the delay line give a major contribution to the OEO phase noise. This can be illustrated using the time jitter, which can be calculated using Eq. (1.42) and the OEO phase noise model. Let's take the curve 23 mW in Fig. 3.20(b). The range 10 Hz – 49 kHz produces the time jitter $\sigma = 27.35$ fs and the range 49 kHz – 51 kHz produces $\sigma = 100.7$ fs. Thus decreasing the spurs could significantly improve the phase stability.

According to Eq. (3.24) increasing Q by a factor of 10 reduces the spurious peaks by 40 dB. But the major problem with high-Q filters is that the filter introduces thermal fluctuations. Another problem is that the commercial filters are made for telecommunications, for they have flat response in the bandwidth, while a sharp response is preferable in our case. Finally, the filter must be tunable, so that the OEO frequency can be switched.

A possible way to implement a tunable high Q-factor filter is the regenerative amplifier (RA). In optics, the regenerative amplifier is an optical amplifier with a resonator in which a light pulse can do multiple round trips before being coupled out. There are some variations of such amplifier. One of the realizations of such amplifier is described by T.C. Teyo et al. in [72]. It consists of the erbium-doped fiber amplifier (EDFA) with optical feedback. In a similar way, if we implement a positive feedback for a microwave amplifier, with an attenuation preventing from sustained oscillation, we get a kind of microwave regenerative amplifier. An architecture with such an amplifier is shown in Fig. 4.1.

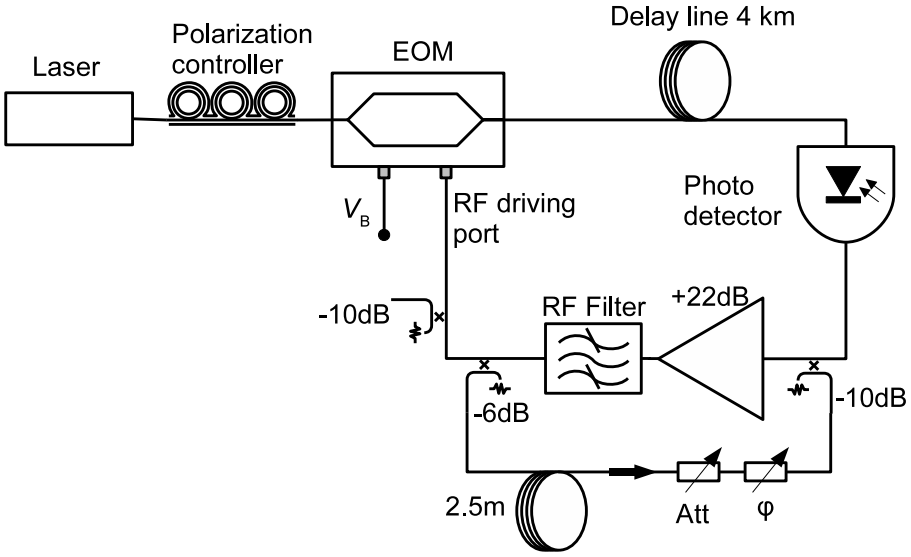

Figure 4.1: An OEO with the regenerative amplifier.

The whole OEO setup can also be viewed as a parallel multiloop architecture, but with one loop (the purely electronic one) of gain just below unity. It can be analyzed

using either the multiloop model, or an RA model together with the one loop model. Since the noise properties of microwave and optical loops differ, it is better to study the RA properties and the whole architecture properties separately.

The transfer function of the RA can be written as a transfer function of an amplifier with a positive feedback

$$H_{\mathrm{RA}}(j\omega) = \frac{G\,\beta_{\mathrm{f}}(i\omega)}{1 - G\,\kappa\beta_{\mathrm{f}}(i\omega)e^{i\omega\tau_{\mathrm{RA}}}}\,, \tag{4.1}$$

where κ represents all the losses in the RA loop, $\beta_{\mathrm{f}}(i\omega)$ is the RF filter transfer function, τ_{RA} is the delay time in the RA loop. The parameter κ impacts on the gain and on the equivalent Q-factor of the RA loop. The closer $\gamma = G\kappa$ to 1, the higher gain and narrower the bandwidth. The gain at ω_0 can be written as

$$G_{\mathrm{RA}} = \frac{G}{1 - G\kappa}. \tag{4.2}$$

The normalized gain is

$$\frac{H(j\omega)}{G_{\mathrm{RA}}} = \frac{(1 - G\kappa)\,\beta_{\mathrm{f}}(i\omega)}{1 - G\kappa\beta_{\mathrm{f}}(i\omega)e^{i\omega\tau_{\mathrm{RA}}}} = \frac{(1-\gamma)\,\beta_{\mathrm{f}}(i\omega)}{1 - \gamma\beta_{\mathrm{f}}(i\omega)e^{i\omega\tau_{\mathrm{RA}}}}\,. \tag{4.3}$$

Equating the square of normalized gain modulus to 0.5, we get the equation relating γ and $\Delta\omega$.

$$\left|\frac{(1-\gamma)\,\beta_{\mathrm{f}}(i\omega)}{1 - \gamma\beta_{\mathrm{f}}(i\omega)e^{i\omega\tau_{\mathrm{RA}}}}\right|^2 = \frac{1}{2}. \tag{4.4}$$

We use the following relations to resolve this equation for γ

$$\begin{aligned} \beta_{\mathrm{f}}(i\omega) &= \rho(\omega)e^{j\vartheta(\omega)}, \\ \rho(\omega) &= \frac{1}{\sqrt{1+\chi^2\,Q^2}}, \\ \vartheta(\omega) &= -\arctan(Q\chi), \\ \chi &= \frac{\omega}{\omega_0} - \frac{\omega_0}{\omega}. \end{aligned} \tag{4.5}$$

In the vicinity of the oscillation frequency where $\left|\frac{\omega-\omega_0}{\omega_0}\right| \ll \frac{1}{2Q}$ we can approximate for positive frequencies

$$\begin{aligned} \chi &\simeq 2\frac{\omega - \omega_0}{\omega_0}, \\ \vartheta(\omega) &\simeq -Q\chi. \end{aligned} \tag{4.6}$$

The dissonance χ is inversely proportional to the equivalent Q of RA, $\chi \simeq \frac{1}{Q_{\mathrm{RA}}}$ for Eq. (4.4). From Eq. (4.4), we get

$$\frac{2(1-\gamma)^2}{1+\chi^2\,Q^2} = \left|1 - \gamma e^{-i\chi(Q+\frac{1}{2}\omega_0\tau_{\mathrm{RA}})}\right|^2. \tag{4.7}$$

Solving this equation for γ, we get

$$\gamma_1 = \frac{(1+\chi^2 Q^2)\cos(\theta) - 2}{\chi^2 Q^2 - 1} - \\ - \frac{\sqrt{1+\chi^2 Q^2}\sqrt{(1-\chi^2 Q^2)\sin(\theta)^2 + 2\cos(\theta)^2 - 4\cos(\theta) + 2}}{\chi^2 Q^2 - 1}, \tag{4.8}$$

$$\gamma_2 = \frac{(1+\chi^2 Q^2)\cos(\theta) - 2}{\chi^2 Q^2 - 1} + \\ + \frac{\sqrt{1+\chi^2 Q^2}\sqrt{(1-\chi^2 Q^2)\sin(\theta)^2 + 2\cos(\theta)^2 - 4\cos(\theta) + 2}}{\chi^2 Q^2 - 1}, \tag{4.9}$$

with

$$\theta = \chi\left(Q + \frac{1}{2}\tau_{\mathrm{RA}}\,\omega_0\right).$$

Solution (4.8) gives $\gamma > 1$, which corresponds to an unstable loop resonator. Solution (4.9) gives $\gamma < 1$ and is suitable for RA. So Eq. (4.9) can be used to find γ at given $\Delta\omega$.

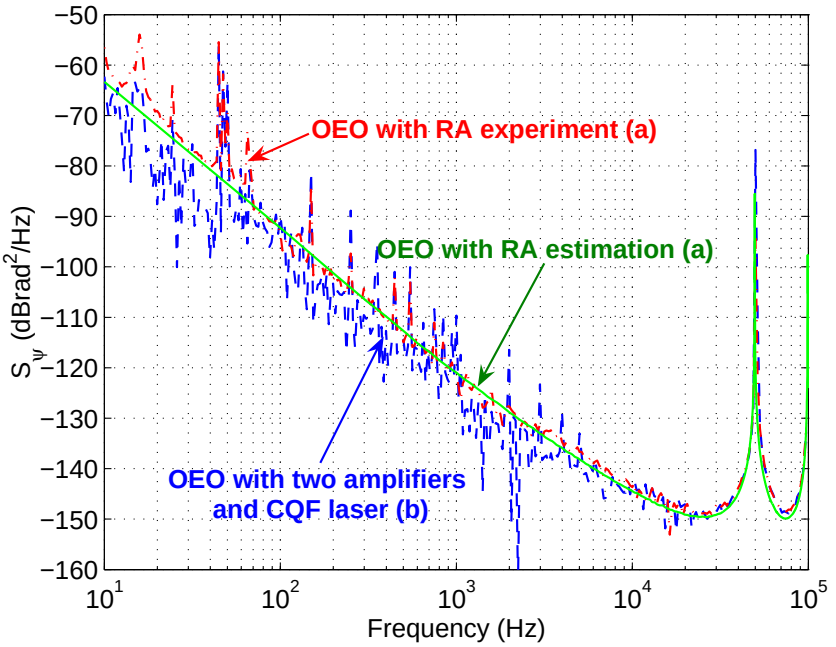

Figure 4.2: Phase noise of an OEO with the regenerative amplifier compared with the "standard" OEO. Output power is +12 dBm for (a), and +17.8 dBm for (b).

In the experiment (see Fig. 4.1), we tuned κ for a bandwidth 2 MHz ($Q_{\mathrm{RA}} = 5000$). The electrical length of the loop was about 2.9 m. The group delay time was 28.8 ns, which corresponds to a FSR 34.4 MHz. This is sufficient to suppress the other modes by the RF filter. Applying Eq. (4.9) and then Eq. (4.2) gives $\gamma = 0.8$ and $G_{\mathrm{RA}} = 36.5$ dB. The LD power was 23 mW. Figure 4.2 compares the OEO phase noise obtained with the

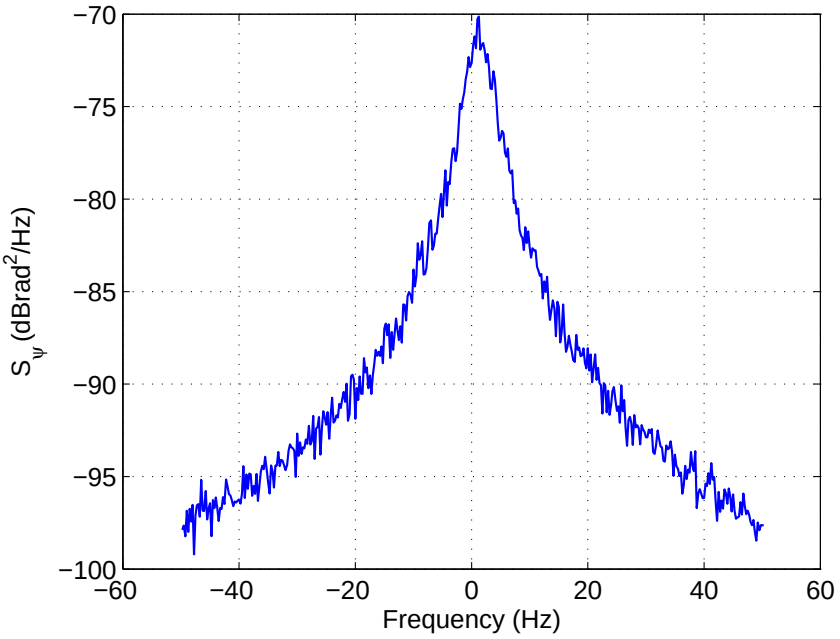

Figure 4.3: The spurious peak in high frequency resolution, for an OEO with RA.

RA and the phase noise obtained with two amplifiers (see Fig. 3.14). The second amplifier is not necessary in the case of the RA because the regeneration mechanism enhances the gain. The estimation details are discussed afterwards.

The spurious peak measured with high frequency resolution is shown in Fig. 4.3. The peak height is 77 dB and width is 6 Hz. As we can see, the spurious peak of OEO with RA is significantly lower. It gives 9.8 fs of time jitter instead of 100.7 fs in the range 49 kHz – 51 kHz. Equations (3.24) and (3.25) give 20 Hz width and 64 dB height of the first peak at $Q = 5000$. The difference in the peak characteristics can be explained by non-coincidence of the RA central frequency and the oscillation mode frequency and approaching of the near side pole to the imaginary axis as it was shown in Section 1.2. The estimated time jitter using the theoretical parameters is 4 fs in the range 49 kHz – 51 kHz. The time jitter has been successfully improved by nearby a factor of 10.

Further we will consider the noise properties of RA. The regenerative amplifier has the property of increasing the flicker phase noise since the delay time in its loop is much less than the coherence time of flicker noise. Let's consider its flicker noise properties. Since we need to consider the frequency range up to the flicker corner frequency, which is about 10 kHz and much less than the FSR of the RA and the RF filter bandwidth, their frequency dependent properties can be neglected. Flicker phase noise can be represented by a constant θ and RA can be represented by the block scheme in Fig. 4.4.

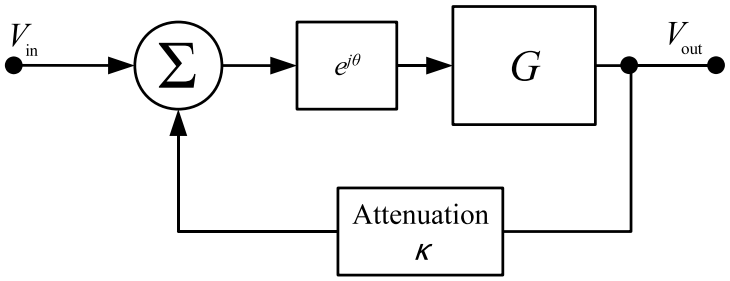

Figure 4.4: The regenerative amplifier block scheme.

Its transfer function is

$$H(j\omega) = \frac{G\, e^{i\theta}}{1 - G\,\kappa\, e^{i\theta}}\,. \tag{4.10}$$

Since $\theta \ll 1$, it can be shown that the argument of the transfer function is

$$\arg H(j\omega) = \frac{\theta}{1 - G\,\kappa} = \frac{\theta}{1-\gamma}. \tag{4.11}$$

Therefore the flicker noise is increased by factor 5 or by 14 dB at $\gamma = 0.8$

Regarding the thermal noise, RA open loop can be represented by the amplifier and the feedback and according to the Friis formula we have [21]

$$\mathcal{F}_{\mathrm{RAOL}} = \mathcal{F} + \frac{\kappa^2 - 1}{G^2}. \tag{4.12}$$

These modifications to the earlier described calculation procedure give the phase noise estimation curve in Fig. 4.2. We can see the very good correspondence of measured and calculated data.

So, the use of RA allows to significantly reduce the spurious peaks and the time jitter by creating a high Q amplifier-filter. Drawbacks are 1) the necessity of strict control and stabilization of the loop gain since the bandwidth and stability of the RA depend on the gain, 2) the introduced thermal sensitivity of RF cable in the regenerative amplifier loop, which is higher than the one of the optical fiber, 3) the higher flicker noise than the one of a cascaded amplifier of similar technology and gain.

4.2 The multiloop OE architecture

Multiple loops implemented with fiber delay lines of different length can be set to obtain large microwave FSR. Hence the spurs can be "easily" suppressed by an RF filter of

moderate Q. This method is already known [10, 73]. The drawbacks of the multiple-loop method are the increased attenuation and the decreased signal-noise ratio because splitters and combiners are introduced. A method for multiple loops optimization was developed by Banky et al. [74]. Particularly, it allows to withdraw the poles, nearest to the fundamental one, to an equal distance from the imaginary axis.

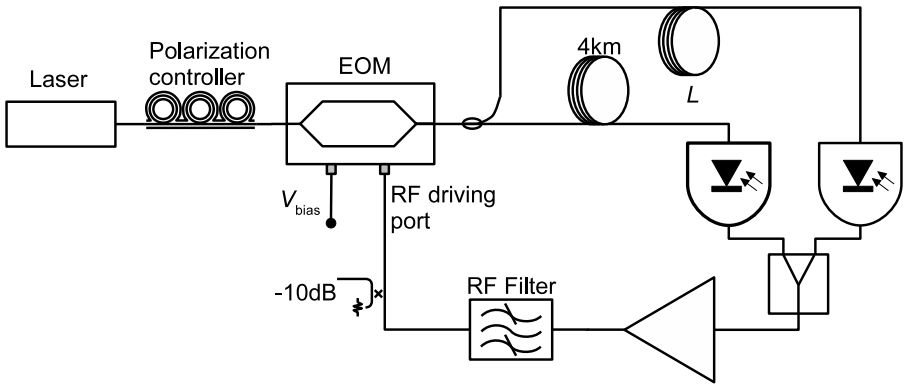

Figure 4.5: An OEO with two delay lines.

Suppressing the spurious peaks in this way, the average phase noise can increase. That can entail increasing the time jitter. We will use a dual loop architecture as shown in Fig. 4.5, and we will consider the time jitter as a function of the second loop length and of the amplitude balance between the loops.

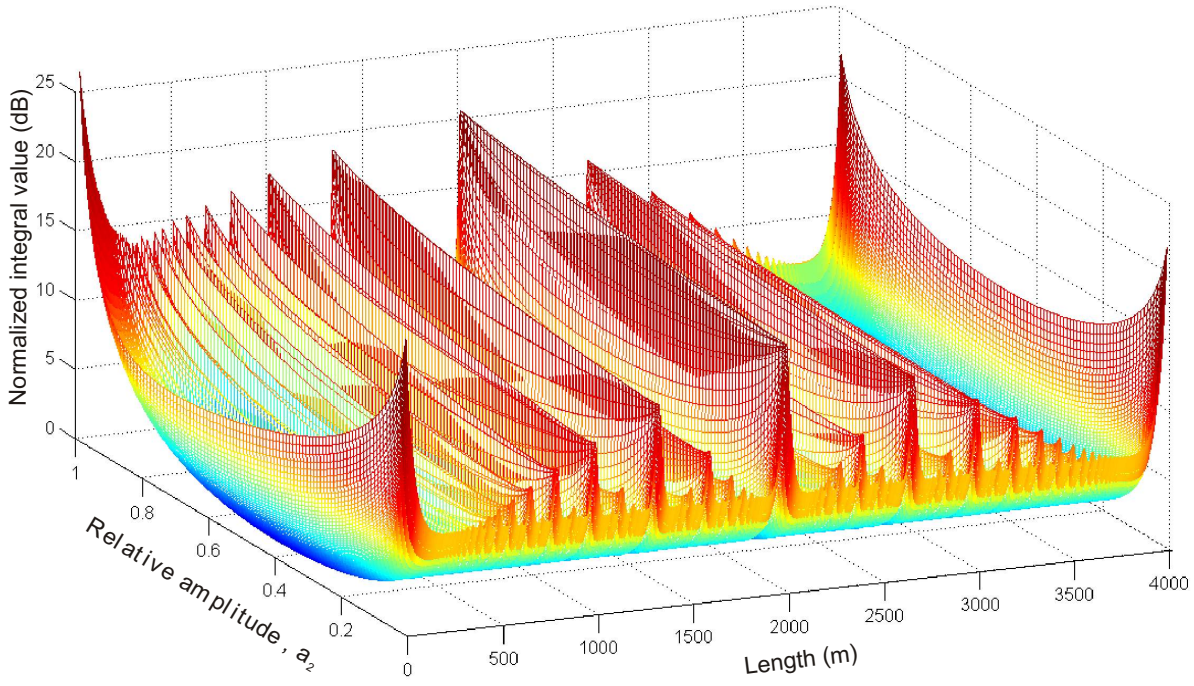

Figure 4.6: The normalized integral values for the white noise power law, dB.

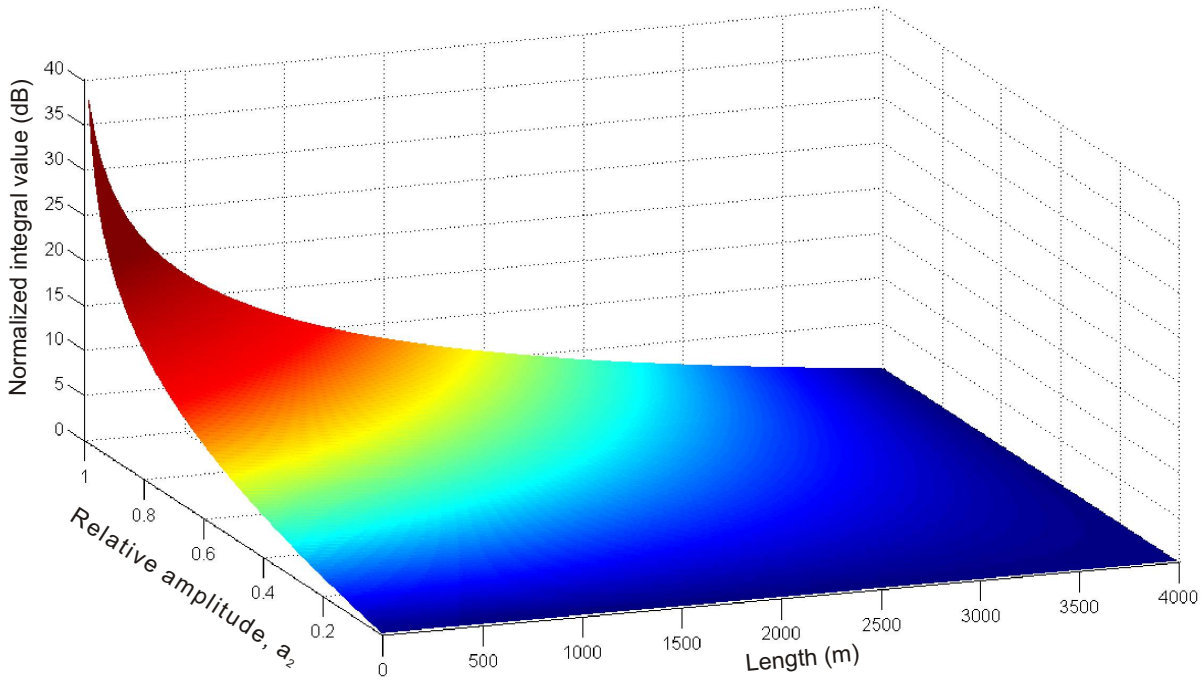

Figure 4.7: The normalized integral values for the flicker noise power law, dB.

Using the same ideas already used to derive Eq. (3.16), we obtain (see Appendix C) the following expression for the phase PSD in the dual loop architecture

$$|\Psi(\omega)|^2 = \mu^2 \frac{\left|\frac{\tilde{\eta}_{\mathrm{m}}(\omega)}{2Q}\right|^2 + \left|\frac{\sqrt{2D_{\mathrm{a}}}}{|\mathcal{A}_0|}\right|^2 + |\varsigma_\psi(\omega)|^2}{|i\omega + \mu\left[1 - a_1 e^{-i\omega\tau_{\mathrm{d}1}} - a_2 e^{-i\omega\tau_{\mathrm{d}2}}\right]|^2}\,, \tag{4.13}$$

where $\tau_{\mathrm{d}1}$ and $\tau_{\mathrm{d}2}$ are the delays created by the two loops, a_1 and a_2 are the optical intensity distribution coefficients in the two loops ($a_1 + a_2 = 1$), which affect the signal amplitudes in the electrical domain.

The sensitivity function for additive noise is

$$\varepsilon_{2\mathrm{L}}(\omega) = \frac{\mu}{i\omega + \mu\left[1 - a_1 e^{-i\omega\tau_{\mathrm{d}1}} - a_2 e^{-i\omega\tau_{\mathrm{d}2}}\right]}\,. \tag{4.14}$$

Since we seek for a reduction of the time jitter as a stability characteristics, we can use a modification of the time jitter integral (1.42) as the target function. Following the discussion in Section 1.4, the phase noise PSD, which is used in the integral, can be represented as a product of the components noise PSD and a square modulus of the

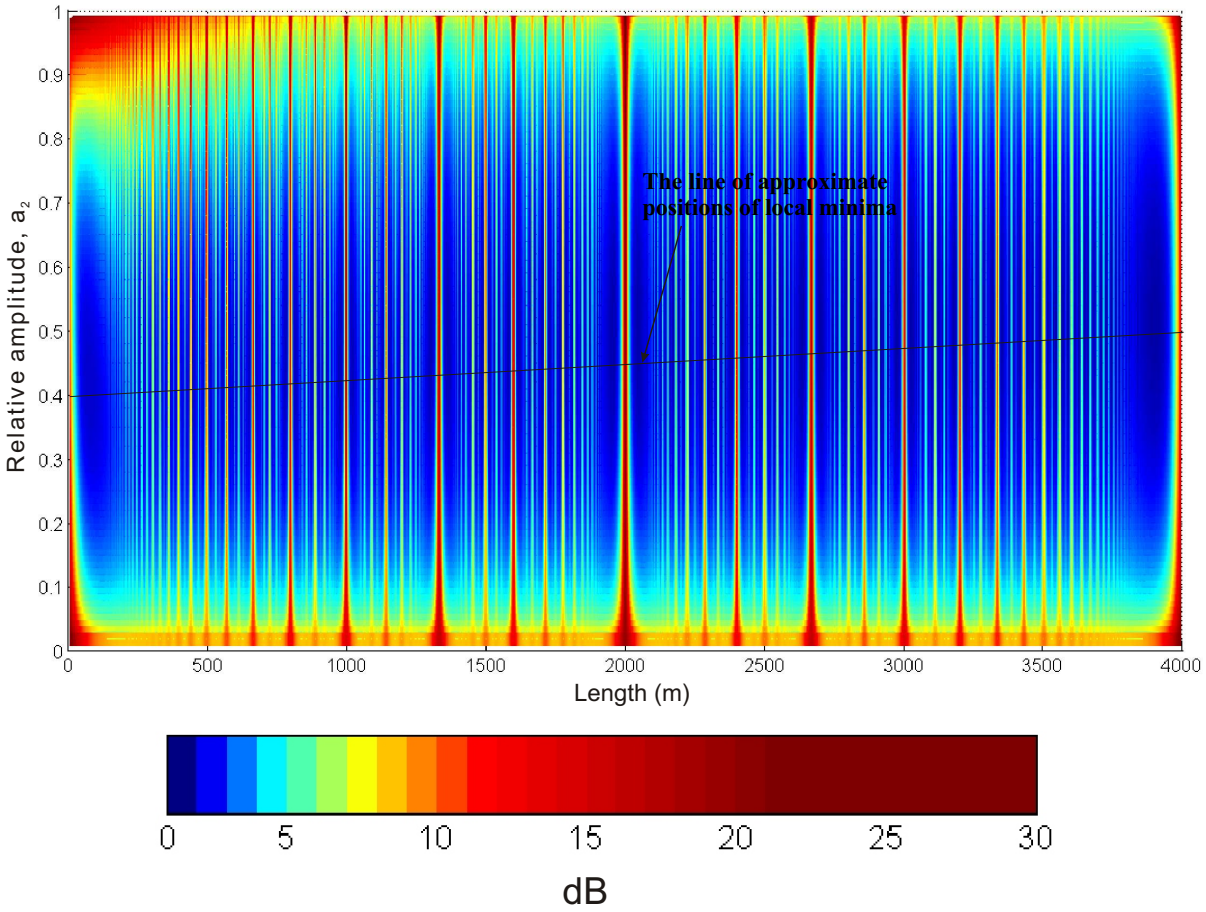

Figure 4.8: The normalized integral values for the white noise power law, dB.

sensitivity function. Using Eq. (1.39), the time jitter integral can be rewritten as

$$\sigma = \frac{1}{2\pi\nu_0}\sqrt{\int_{f_{\min}}^{f_{\max}} S_\phi(f)|\varepsilon_{2\mathrm{L}}(f)|^2\mathrm{d}f} = \frac{1}{2\pi\nu_0}\sqrt{\int_{f_{\min}}^{f_{\max}} \sum_{n\le 0}^{0} b_n f^n |\varepsilon_{2\mathrm{L}}(f)|^2\mathrm{d}f}$$
$$= \frac{1}{2\pi\nu_0}\sqrt{\sum_{n\le 0}^{0} b_n \int_{f_{\min}}^{f_{\max}} f^n |\varepsilon_{2\mathrm{L}}(f)|^2\mathrm{d}f}\,. \tag{4.15}$$

Thus, to find the optimal combination of parameters, it is sufficient 1) to calculate a mesh of integral values for different loop lengths and amplitude balance between the loops and for different power-law terms, 2) to multiply the values by corresponding b_n, 3) to sum the values corresponding to different power terms, and 4) to find the minimum.

We have done the mesh of integral values for $0.01 \le a_1 \le 0.09, 10\mathrm{m} \le L \le 3990$ m for white noise ($f_{\min} = 10$ Hz, $f_{\max} = 25$ MHz) and flicker noise ($f_{\min} = 10$ Hz, $f_{\max} = 20$ kHz) since they are predominant in OEOs. These meshes are presented in Fig. 4.6 and 4.7. The mesh values are normalized to the minimum values of each mesh and presented in dB.

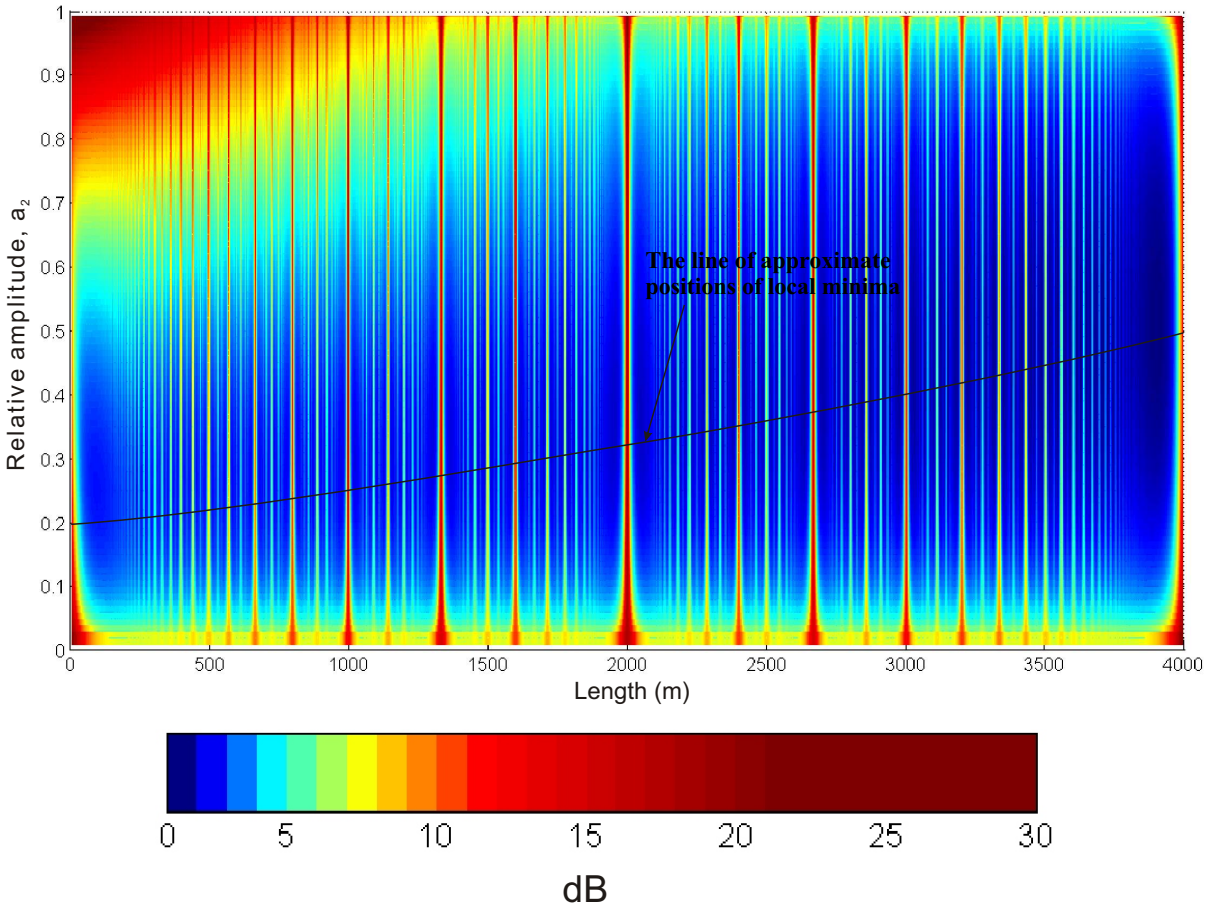

Figure 4.9: The normalized integral values for the sum of white noise and flicker noise power laws, dB.

The data of Fig. 4.6 are also shown in Fig. 4.8. The black line shows the approximate positions of local minima.

The sum of the meshes at $b_0 = -140$ dBrad^2/Hz and $b_1 = -120$ dBrad^2/Hz is shown in Fig. 4.9. It has a global minimum at $a_2 = 0.5$, $L = 3899$ m. The phase noise diagram for this global minimum is shown in Fig. 4.11. The black line shows the approximate positions of local minima in the vertical direction (vs. a_2). The diagram cut going by this line representing time jitter is shown in Fig. 4.10. As we can see, there are many local minima. The difference between the first minimum and the global minimum is about 3 fs. They have different widths and one could notice that wider minima are better, because they give less sensitivity to the length inaccuracies.

Further increasing number of loops can further decrease the level of some residual spurious peaks. Yet we don't expect a significant reduction of the total time jitter. The third loop adds two degrees of freedom increasing optimization complexity.

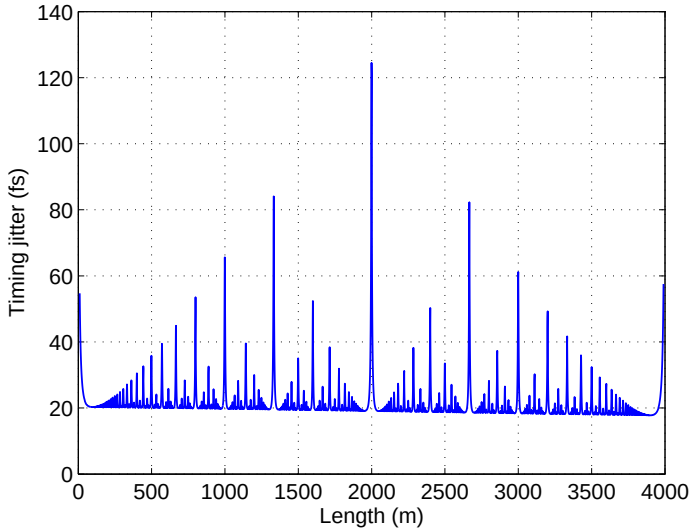

Figure 4.10: The cut by the approximate line of local minima.

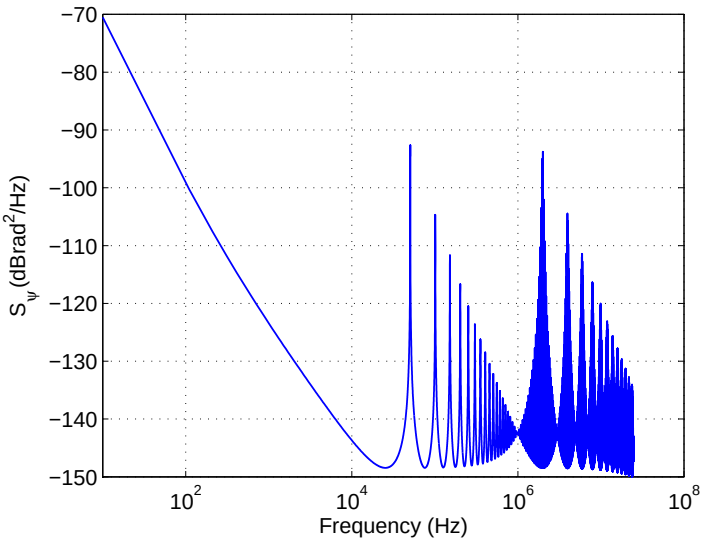

Figure 4.11: The calculated phase noise for the case of OEO with CQF935 laser at laser power 23 mW and two low phase noise microwave amplifiers ($G = 44$ dB). Frequency range is 10 Hz – 25 MHz. Two loops: $a_1 = a_2 = 0.5$, 4000 m and 3899 m.

4.3 Comparison of OEO architectures using the Allan variance

We will compare three architectures of the OEO with the Allan variance for short-term frequency stability. These architectures are: 1) the single loop OEO (RF filter $Q = 200$), 2) the OEO with regenerative amplifier (RF filter equivalent $Q = 5000$), 3) the dual-loop

OEO (RF filter $Q = 200$). Phase noise PSD calculated using Eq. (3.16) for (1) and (2) and Eq. (4.13) for (3) is presented in Fig. 4.12.

We use Eq. (1.40) to estimate the Allan variances for these cases. The results are presented in Fig. 4.13.

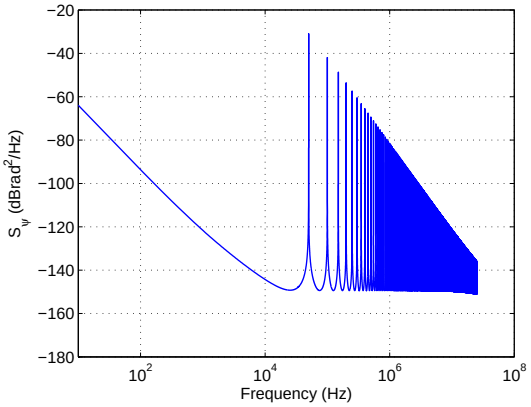

(a) The single loop architecture. RF filter $Q = 200$. The first spurious peak is -29 dBrad^2/Hz.

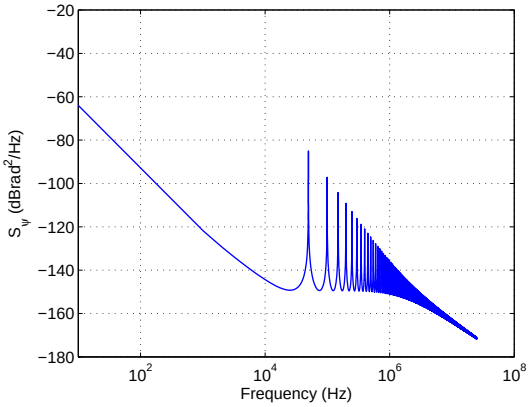

(b) The architecture using the RA. Equivalent RF filter $Q = 5000$. The first spurious peak is peak -85 dBrad^2/Hz.

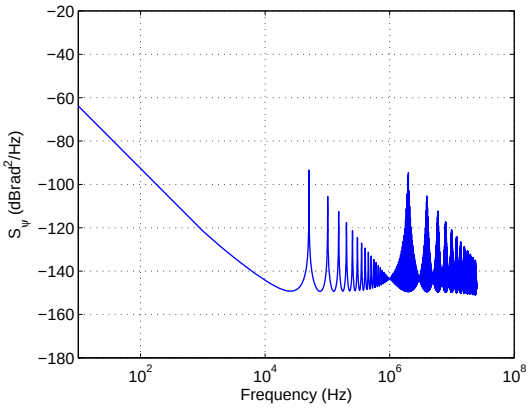

(c) The dual-loop architecture. Two loops: $a_1 = a_2 = 0.5$, 4000 m and 3899 m. RF filter $Q = 200$. The first spurious peak is -94 dBrad^2/Hz.

Figure 4.12: OEO phase noise PSD.

Examining Fig. 4.13, we can see that the $1/f^3$ phase noise produces constant $\sigma_y^2(\tau) = 5.5 \cdot 10^{-24}$, which shows up for $\tau > 300$ ms. On the left-hand side, the slopes are of 10^{-2}/decade. They show up at different τ. This difference can be ascribed to different distribution of spectral energy due to the different Q-factors and the influence of additional loop. This diagram illustrates well the enhancement of OEO short-term stability due to using the techniques suppressing the spurious peaks.

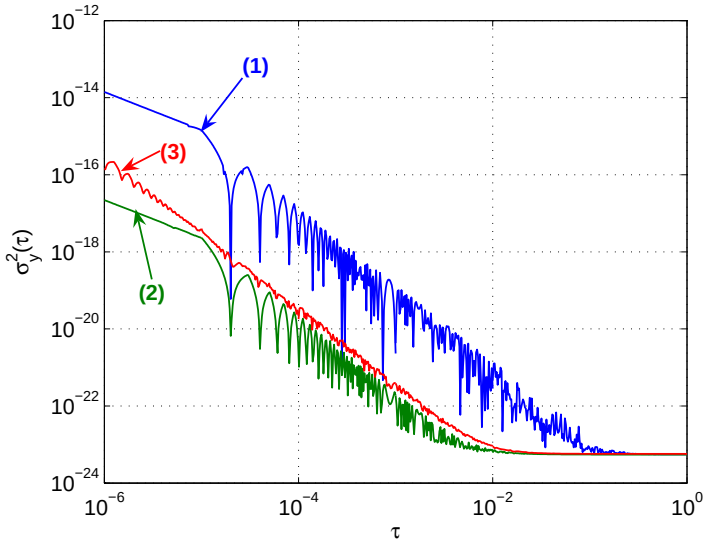

Figure 4.13: The Allan variance for the three variants: 1) the single loop OEO (RF filter $Q = 200$), 2) the OEO with the RA (RF filter equivalent $Q = 5000$), 3) the dual-loop OEO (RF filter $Q = 200$).

4.4 The architecture with a feedforward amplifier and a VMDP

As it was earlier indicated, the flicker phase noise of the photodiode (-120 dBrad^2/Hz) is higher than the one of the AML amplifier. Therefore, it can limit the achievable phase noise. To reduce the photodiode flicker phase noise, the same solution, which is used to reduce the amplifiers flicker, can be applied. According to Ref. [21], the flicker coefficient of the parallel amplifier is

$$b_{-1} = \frac{1}{m}[b_{-1}]_{\text{branch}} \,. \tag{4.16}$$

Thus, the flicker phase noise of photodiodes can be reduced by parallel connection of them. Such architecture is already realized in the form of the velocity matched distributed photodetector [75, 76, 77]. These photodetectors combine very high bandwidth (hundreds of gigahertz) and very high photocurrents (tens of milliamperes). Parallel connection of 10 photodiodes was already considered in articles. Therefore 10 dB reduction of flicker phase noise is already achievable. Taking into account the high rates of optoelectronic technology advance, integration of higher number of photodiodes seems possible. Another issue is the possible inverse dependence of the flicker noise on the junction volume. It was discussed in Ref. [21] in relation to amplifiers. A photodiode in VMDP has much smaller surface, and therefore smaller junction volume than a single fast photodiode. Additional study is therefore necessary – under the last hypothesis of this paragraph, we can expect that it can have higher flicker noise.

According to the same principle, we can expect that the multiloop architecture reduces the flicker noise due to the parallel connection of photodiodes.

The amplifier flicker noise can significantly limit the oscillator spectral purity. Therefore we use the AML microwave amplifiers with low flicker noise. To our knowledge, AML is the only one company that produces low flicker phase noise amplifiers. Reference [21] explains why the low flicker is achieved by parallel connection of several amplifiers. When the number of amplifiers is doubled, the phase noise decreases by 2.5 dB and power consumption is doubled. The missing 0.5 dB is ascribed to the asymmetry in the power splitters and combiners. So any further reducing the noise requires a large number of amplifiers. Such amplifiers have higher noise figure than a single simple amplifier. Therefore, the use of an alternate way is actual. A feedforward amplifier (FFA) [78] is an alternative that potentially can give lower phase noise levels in the part of amplifier without such difficulties. It is shown on Fig. 4.14 [21].

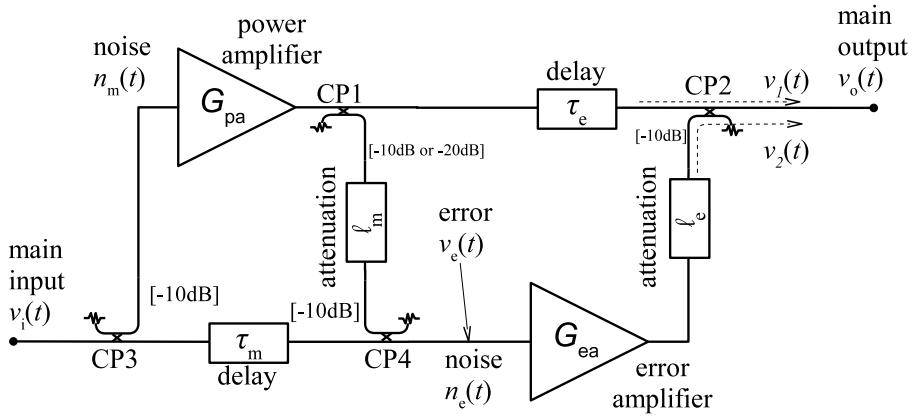

Figure 4.14: Feedforward amplifier [21].

Originally, the FFA configuration was conceived to reduce the harmonic distortion in amplifiers. More recently, this technique found application in the power amplifier for CDMA telecommunications, which require high linearity. Different aspects of FFA are discussed in [21, 69, 78, 79, 80, 81].

Examining Fig. 4.14, we can see that the interferometer CP4 produces an error signal by subtracting an amplified signal from its original after a corresponding scaling. Then the interferometer CP2 sums the amplified error signal and the amplified signal. In this way, the principal part of the signal distortion of FFA depends on the error amplifier that can be of small power and therefore made highly linear. The analysis of FFA suggests that the feedforward technique also reduces the $1/f$ noise. This should happen because the flicker of the power amplifier is detected and corrected for by the error amplifier. The latter cannot flicker around the carrier frequency ν_0 because the carrier power is close to zero at its input.

According to [69], the phase noise performance of the feedforward amplifier is governed

by the input power to the system, the phase noise characteristics of the amplifiers and the achievable carrier noise cancellation in the two interferometers (CP4, CP2):

$$S_{\varphi}^{\mathrm{FFA}} = \frac{S_{\varphi}^{\mathrm{pa}}}{NS} + \frac{k\mathcal{F}_{\mathrm{ea}}T_0\ell_{\tau_{\mathrm{m}}}}{P_{\mathrm{in}}(1-\eta_3^2)(1-\eta_4^2)} + \frac{S_{\varphi(1\ \mathrm{Hz})}^{\mathrm{ea}}}{CS}\frac{1\mathrm{Hz}}{f_{\mathrm{o}}}, \tag{4.17}$$

where $S_{\varphi}^{\mathrm{pa}}$ is the phase noise of the power amplifier, $S_{\varphi(1\ \mathrm{Hz})}^{\mathrm{ea}}$ is the flicker phase noise of the error amplifier at 1 Hz, NS is the noise suppression factor (in CP2), $\mathcal{F}_{\mathrm{ea}}$ is the error amplifier noise figure, $\ell_{\tau_{\mathrm{m}}}$ is the loss in the delay element τ_{m}, P_{in} is the input power, η_3 and η_4 are the voltage coupling coefficients at the couplers CP3 and CP4, f_{o} is the offset frequency, and CS is the carrier suppression factor (in CP4) defined as

$$\begin{aligned} CS &= \frac{\text{Power available at one combiner input} - \text{combiner loss}}{\text{Power input to error amplifier}} \\ &\approx \frac{P_{\mathrm{in}}}{P_{\mathrm{in}}^{\mathrm{ea}}}\,\frac{(1-\eta_3^2)(1-\eta_4^2)}{\ell_{\tau_{\mathrm{m}}}}\,, \end{aligned} \tag{4.18}$$

where $P_{\mathrm{in}}^{\mathrm{ea}}$ is the input power of error amplifier.

Assuming that $\mathcal{F}_{\mathrm{ea}} = 2$ dB, $\ell_{\tau_{\mathrm{m}}} = 0.75$ dB, $P_{\mathrm{in}} = 1$ mW, $\eta_3 = \eta_4 = -10$ dB, and $NS = CS = \infty$, we have $S_{\varphi}^{\mathrm{FFA}} = -170$ dBrad^2/Hz.

The carrier suppression factor can also be expressed in terms of amplitude mismatch ϵ and phase error φ [69]

$$CS = -10\log(1 + (1+\epsilon)^2 - 2(1+\epsilon)\cos\varphi)\,,\mathrm{dB}\,. \tag{4.19}$$

For example, for about 30 dB carrier suppression, it is necessary to provide $\epsilon = 0.03$ and $\varphi = 1$ °simultaneously. NS can be expressed in an identical manner.

In telecommunications, the carrier suppression at the error amplifier input must be ensured in the large bandwidth required by the CDMA systems. Therefore, the phase and amplitude balance condition requires the true group-delay matching at the error amplifier input. Of course, this is a difficult design task. Conversely, in the case of the oscillator we need to suppress the flicker only in a narrow bandwidth. Hence the delay-matching condition is replaced with the phase-matching condition, which is significantly easier to achieve. In practice, a variable phase shifter is sufficient.

In most oscillators the amplitude limitation is ensured by the amplifier. Unfortunately, the FFA cannot work saturated because the error amplifier saturates. This difficulty can be avoided in the case of OEO because the MZ modulator can be used to limit the oscillator power, letting the FFA in fully linear operation.

4.5 Conclusion

In this chapter, the use of a regenerative amplifier, a dual optoelectronic loop, velocity matched distributed photodiodes, and a feedforward amplifier for improving the OEO phase noise performance is discussed. Experimental data of applying the regenerative amplifier in the OEO are presented. The considered methods give a high potential for further reducing the OEO phase noise.

...

Conclusions and perspectives

Conclusions

In this work, we have introduced the OEO model based on the stochastic nonlinear delay differential equation. This equation includes the resonator terms, EOM modulation function, time delay, and noise components. Such model allows studying all essential processes occurring in OEO. Linearizing this equation around the fundamental frequency, we found the expression for phase noise and amplitude noise of OEO.

We introduced the most significant sources of noise in this model: the thermal noise, shot noise, laser RIN, combined effect of laser frequency noise and the fiber dispersion, and the flicker noise of the amplifier and the photodiode flicker. The thermal noise, shot noise, and laser high frequency RIN set the white noise in the loop. We measured the laser low frequency RIN and the laser frequency noise using the cross-correlation method that reduces the noise contribution of photodetectors.

We calculated phase noise levels of these components as well as total phase noise levels for three OEO configurations based on the classical architecture. We also measured the OEO phase noise for these configurations. A good agreement between experiment and theory was obtained, which validates the model. The model also conforms well to the Leeson effect [67]. The best result obtained in our experiments is: -66 dBrad^2/Hz at 10 Hz, -143 dBrad^2/Hz at 10 kHz, -149 dBrad^2/Hz at 25 kHz.

We arranged the components according to their noise magnitudes. In all cases, in the flicker noise frequency range (from 10 Hz to about 2 kHz), the highest contribution was the phase noise produced by the delay fluctuation, which is caused by the laser frequency noise combined with the fiber dispersion. Concerning the white phase noise and phase noise floor, the situation depends on microwave amplifier gain that increases the white noise contribution. Therefore it is preferable to decrease microwave amplifier gain or completely exclude the microwave amplifier from the loop. This conclusion coincides with conclusions of other authors but we note that this solution allows to decrease the white noise contribution also but not only to eliminate the amplifier noise.

The arrangement by phase noise contribution shows the priority of solutions for de-

creasing the total phase noise level of OEO. The first proposed solution is the use a fiber with zero dispersion at the laser wavelength. This can provide about -72 dBrad^2/Hz at 10 Hz and -153 dBrad^2/Hz at 10 kHz in the configuration with one amplifier (22 dB). Then the photodiode flicker phase noise and LD RIN should be decreased. Remaining contributions are amplifier flicker phase noise and the photodiode shot noise. Every next noise level becomes more and more difficult to decrease.

As a method to decrease the OEO noise spurs, we considered the regenerative amplifier. It is a positive feedback amplifier with a loop gain close to, but less than 1. It is often used in optical applications for strong amplification of optical pulses, usually with ultrashort pulse durations in the picosecond or femtosecond domain [82]. In microwave applications, it allows to get a narrow pass band without using a high Q filter. Drawbacks of such a method are 1) the necessity of strict control and stabilization of the loop gain since the bandwidth and stability of this amplifier depend on the gain, 2) the introduced thermal sensitivity of RF cable in the regenerative amplifier loop, which is higher than the one of the optical fiber, 3) that the flicker noise introduced by the regenerative amplifier is higher than the one of a cascaded amplifier of similar technology and gain.

Other methods include the use of a feedforward amplifier, and/or a velocity matched distributed photodetector. They allow to reduce the phase noise of amplifier and photodetector.

Measurement of OEO phase noise requires a measurement bench having very low noise floor. We used the method of comparing a signal with its delayed copy by a phase detector in the form of saturated microwave mixer. The 2 km fiber spool served as a delay line. The cross-correlation method was used to decrease the noise floor further.

Since the measurement bench adjustment can deviate from the required one mainly because of temperature fluctuations, we developed two I controllers: one for stabilizing the quadrature condition at the mixer input and one for stabilizing the operating point of MZ EOM. They facilitate long time measurement cycles and decrease the possibility of measurement errors.

We considered the application of the Bode integral principle to the phase noise characteristic of an oscillator. We found it applicable to the oscillator phase noise model according to the phase noise transfer function, but it is not applicable to the model based on the stochastic nonlinear delay differential equation. The sensitivity function principle, which is part of the Bode integral principle, is still useful in resolving optimization problems.

We have calculated the time jitter of a dual optical loop architecture vs. the length of second loop and the relative optical intensity in it. The diagram showed many possible combinations of these two parameters that give low time jitter. The global minimum is obtained at almost equal length of the loops, but other minima do not differ significantly in the phase noise performances, and they can be obtained at much less length of the

second loop.

Perspectives

The OEO phase noise study has shown the large potential of a classical OEO architecture for obtaining low phase noise oscillator. It confirms the idea that the simpler things the better. We have achieved the phase noise level close to the best reported levels. Using the conclusions and the proposed solutions, the phase noise of OEO can be reduced further.

While the technology advances, the fiber spools get more compact. This increases the possibility to make OEO more compact since the demand of compact solutions gets stricter. For example, the General Photonics offers fiber spools of 3.5 inch in diameter [83].

Significant performance improvement and size reduction can be achieved using WGM optical resonators that have dimensions from several millimeters to several hundreds micrometers, have very high Q factor, and large FSR [84, 85]. Their drawback is the difficulties of light coupling, which is very sensitive to vibration. But most likely they will be resolved soon.

Appendix A

The quadrature control loop circuit

Basing on the determined parameters, we implemented the I controller for every measurement channel. Since for the purpose of quadrature condition $V_0 = 0$ V, the summator before the I controller (see Fig. 2.12) is not necessary and the inverting circuit can be placed after the integrator. The integrator is shown on figure A.1. The integrator is implemented with an operational amplifier U_{1A} and capacitive negative feedback C_1, C_2. The second operational amplifier U_{1B} with resistive negative feedback ($G = -1$) is used as an inverting amplifier. Both of the amplifiers are included in IC TL082A. Since the characteristics of the RF mixer has positive or negative slope (see Eq. 2.22), it is necessary to use or not use the inverting amplifier depending on which slope is used during the measurement.

For the determined in Section 2.4.1 characteristics, $C_\mathrm{I} = C_1C_2/(C_1 + C_2) = 500$ μF, $R_1 = \tau_\mathrm{I}/C_\mathrm{I} = 200$ kΩ. The capacitance $C_\mathrm{I} = 500$ μF is made of two electrolytic capacitors of 1000 μF each connected in series with different polarity direction. In such a way, they form a non-polarized capacitor of capacitance equal to the half of nominal. Non-polarized capacitors of such capacitance are expensive and rare. And this solution allows to avoid this difficulty. Jumper J1 serves to reset the capacitors before closing the loop. Jumper J_2 serves for changing output signal polarity. The resistor R_5 with diodes D_1 – D_4 limit the output signal to prevent going out of the range of LD operational temperatures. The supply voltage is +15 V and −15 V.

The steps of measurement procedure using the quadrature control loop are

1. To close the “Reset” jumper and the “+” or “-” jumper on the I controller board;
2. To prepare the measurement bench and DUT for measurement cycle;
3. To adjust with the phase shifter the quadrature condition in the inputs of the mixer to have 0 V mean voltage in the output of the measurement bench using a voltmeter;

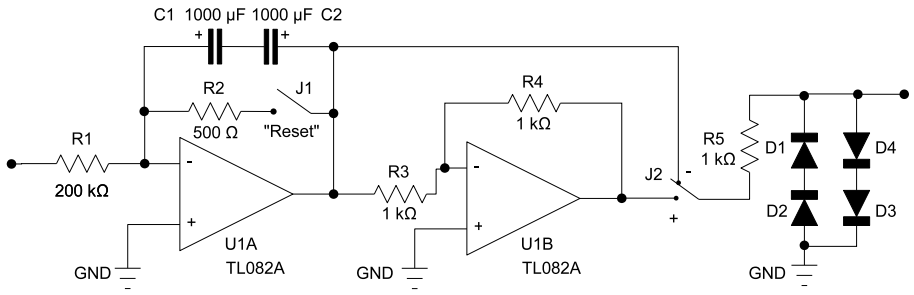

Figure A.1: The I controller circuit scheme.

4. To open the "Reset" jumper on the I controller board;
5. To observe the V_{out} in the output of measurement bench;
6. To change the position of "+" or "-" jumper to the opposite if the absolute value of V_{out} increases;

Then the measurement can be done. At the end of measurement session, before switching off or disconnecting the oscillator under test, it is necessary to close the "Reset" jumper to prevent running the laser temperature to the operation temperature bound.

Appendix B

MZ operating point control loop circuit

The I controller for MZ modulator circuit scheme is shown in Fig. B.1. Two channels are shown there. The integrators are built with operational amplifiers U_{2A}, U_{2B}, negative capacitive feedback C_1, C_6, and resistors R_5, R_9. The resistors R_3, R_8 and potentiometers P_1, P_2 serve to create reference voltages for integrators and consequently define the operation point of MZ modulators. The resistors R_6, R_{10} are the current-voltage conversion resistors for the photodiodes integrated in modulators. The IC U_1 is the source of stable reference voltage. The jumpers J_2, J_7 and the resistors R_2, R_7 serve to reset the integrators capacitors. The jumpers J_3, J_4, J_8, J_{10} serve to change the polarity of transfer function since operation point can be on positive or negative slope of MZ modulator. The supply voltage is +10 V and −10 V.

The controller adjustment procedure for one channel is the following:

1. To connect a voltmeter to contacts J_6;
2. To close the contacts 1-2 of jumpers J_3 and J_4;
3. To close the reset jumper J_2;
4. To adjust the potentiometer P_1 to ground;
5. To open the reset jumper J_2;
6. To vary the potentiometer P_1 and find the maximum voltage value $V_{\max}$; if during varying the potentiometer, the voltage uncontrollably goes to some value and stays there it necessary to come back to the step (2), close contacts 2-3 instead 1-2 of jumpers J_3 and J_4, and repeat further steps;
7. To adjust the potentiometer P_1 so as to have $V_{\max}/2$.

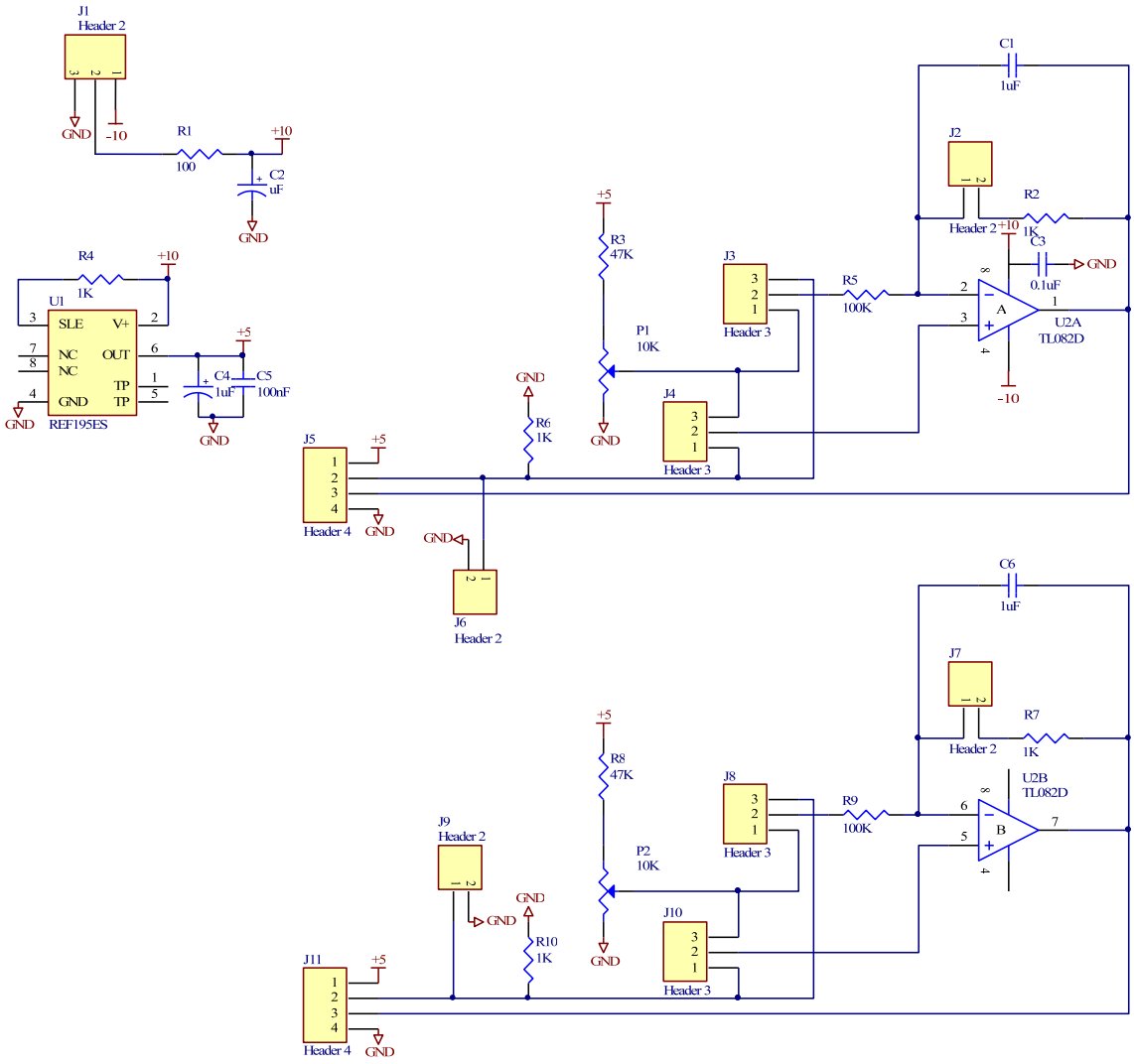

Figure B.1: The I controller for MZ modulator circuit scheme.

Once the adjustment procedure is done, the controller can function without adjustment if the input optical power stays unchanged. It is necessary to turn on the controller when there is the input optical power otherwise the output voltage can be fixed at some non-optimal value.

Appendix C

The phase noise PSD for a dual loop architecture

The dynamics of two loop OEO microwave oscillation can be described as follows

$$x + \tau\frac{\mathrm{d}x}{\mathrm{d}t} + \frac{1}{\theta}\int_{t_0}^{t} x(s)\mathrm{d}s = \beta\cos^2[a_1 x(t-\tau_{\mathrm{d}1}) + a_2 x(t-\tau_{\mathrm{d}2}) + \phi], \tag{C.1}$$

where $\tau_{\mathrm{d}1}$ and $\tau_{\mathrm{d}2}$ are the delays created by two loops, a_1 and a_2 are the amplitude coefficients of signals in the two loops ($a_1 + a_2 = 1$).

Since we are interested by single-mode microwave oscillations, the solution of Eq. (C.1) can be expressed under the form

$$x(t) = A(t)\cos(\omega_0 t + \psi(t)) \tag{C.2}$$

and we can assume that

$$\omega_0\tau_{\mathrm{d}1} = 2\pi n \qquad \text{and} \qquad \omega_0\tau_{\mathrm{d}2} = 2\pi m, \tag{C.3}$$

where n and m natural numbers. Therefore

$$\begin{aligned} a_1 x(t-\tau_{\mathrm{d}1}) + a_2 x(t-\tau_{\mathrm{d}2}) &= A(t)\cos(\omega_0 t + \psi(t-\tau_{\mathrm{d}1}) + \beta) \\ \beta &= \arctan\left(\frac{a_2\sin(\Delta\psi)}{a_1 + a_2\cos(\Delta\psi)}\right) \\ \Delta\psi &= \psi(t-\tau_{\mathrm{d}2}) - \psi(t-\tau_{\mathrm{d}1}). \end{aligned} \tag{C.4}$$

Since $\Delta\psi \ll 1$ we can rewrite (C.4) as

$$a_1 x(t-\tau_{\mathrm{d}1}) + a_2 x(t-\tau_{\mathrm{d}2}) = A(t)\cos(\omega_0 t + \psi(t-\tau_{\mathrm{d}1}) + a_2\Delta\psi)\,. \tag{C.5}$$

Then Eq. (3.13) can be modified as

$$\dot{\psi} = \mu\left(\psi_{\tau_{\mathrm{d}1}} + a_2\Delta\psi - \psi + \varsigma_\psi(t) + \frac{\eta_{\mathrm{m}}(t)}{2Q} + \frac{\xi_{\mathrm{a},\psi}(t)}{|\mathcal{A}_0|}\right)\,. \tag{C.6}$$

Then we have

$$|\Psi(\omega)|^2 = \mu^2 \frac{\left|\frac{\tilde{\eta}_{\mathrm{m}}(\omega)}{2Q}\right|^2 + \left|\frac{\sqrt{2D_{\mathrm{a}}}}{|\mathcal{A}_0|}\right|^2 + |\varsigma_\psi(\omega)|^2}{\left|i\omega + \mu\left[1 - e^{-i\omega\tau_{\mathrm{d}1}} - a_2\left(e^{-i\omega\tau_{\mathrm{d}2}} - e^{-i\omega\tau_{\mathrm{d}1}}\right)\right]\right|^2} \tag{C.7}$$

and finally taking into account that $a_2 = 1 - a_1$

$$|\Psi(\omega)|^2 = \mu^2 \frac{\left|\frac{\tilde{\eta}_{\mathrm{m}}(\omega)}{2Q}\right|^2 + \left|\frac{\sqrt{2D_{\mathrm{a}}}}{|\mathcal{A}_0|}\right|^2 + |\varsigma_\psi(\omega)|^2}{\left|i\omega + \mu\left[1 - a_1 e^{-i\omega\tau_{\mathrm{d}1}} - a_2 e^{-i\omega\tau_{\mathrm{d}2}}\right]\right|^2}\,. \tag{C.8}$$

Bibliography

[1] S. Romisch, J. Kitching, E. Ferre-Pikal, L. Hollberg, and F.L. Walls. Performance evaluation of an optoelectronic oscillator. *IEEE Trans. Ultras. Ferroelec. and Freq. Contr.*, 47(5):1159–1165, September 2000.

[2] R.T. Logan Jr., L. Maleki, and M. Shadaram. Stabilization of oscillator phase using a fiber-optic delay-line. In *Proc. Freq. Control Symp.*, pages 508–512, 1991.

[3] G. Van Wiggeren and R. Roy. Optical communication with chaotic waveforms. *Phys. Rev. Lett.*, 81(16):3547–3550, 1998.

[4] S. Donati and C. Mirasso. Optical chaos and its applications to cryptography. *IEEE J. Quantum Electron.*, 38(9):1138–1140, 2002.

[5] E. Genin, L. Larger, J.-P. Goedgebuer, Min Won Lee, R. Ferriére, and X. Bavard. Chaotic oscillations of the optical phase for multigigahertz-bandwidth secure communications. *IEEE J. Quantum Electron.*, 40(3):294–298, March 2004.

[6] N. Gastaud, S. Poinsot, L. Larger, J.-M. Merolla, M. Hanna, J.-P. Goedgebuer, and F. Malassenet. Electro-optical chaos for multi-10 Gbit/s optical transmissions. *Electron. Lett.*, 40(14):898–899, July 2004.

[7] A. Neyer and E. Voges. High-frequency electro-optic oscillator using an integrated interferometer. *Appl. Phys. Lett.*, 40(1):6–8, 1982.

[8] X.S. Yao and L. Maleki. Optoelectronic microwave oscillator. *J. Opt. Soc. Am. B - Opt. Phys.*, 13(8):1725–1735, 1996.

[9] X. S. Yao and L. Maleki. High frequency optical subcarrier generator. *Electron. Lett.*, 30(18):1525–1526, 1994.

[10] X.S. Yao, L. Maleki, and D. Eliyahu. Progress in the opto-electronic oscillator - A ten year anniversary review. In *Proc. MTT-S*, Fort Worth, TX, 2004.

[11] Yu Ji, X.S. Yao, and L. Maleki. Compact optoelectronic oscillator with ultralow phase noise performance. *Electron. Lett.*, 35(18):1554–1555, September 1999.

[12] D. Eliyahu, K. Sariri, J. Taylor, and L. Maleki. Opto-electronic oscillator with improved phase noise and frequency stability. In *Proc. SPIE Photonics West*, pages 139–147, 2003.

[13] P. Urquhart. Transversely coupled fiber fabry-perot resonator: theory. *Appl. Opt.*, 26(3):456–463, 1987.

[14] J.E. Heebner, V. Wong, A. Schweinsberg, R.W. Boyd, and D.J. Jackson. Optical transmission characteristics of fiber ring resonators. *IEEE J. Quantum Electron.*, 40(6):726–730, 2004.

[15] Kerry Vahala, editor. *Optical Microcavities*. World Scientific, 2004.

[16] P.H. Merrer, H. Brahimi, and O. Llopis. Optical techniques for microwave frequency stabilization: resonant versus delay line approaches and related modelling problems. In *Proc. of 2008 IEEE Topical Meeting on Microwave Photonics, Gold Coast: Australia*, 2008.

[17] H. Tavernier, N.N.T. Kim, P. Féron, R. Bendoula, P. Salzenstein, E. Rubiola, and L. Larger. Optical disk resonators with micro-wave free spectral range for optoelectronic oscillator. In *Proc. of European Time and Frequency Forum, Toulouse: France*, 2008.

[18] A.B. Matsko, A.A. Savchenkov, N. Yu, and L. Maleki. Whispering-gallery-mode resonators as frequency references. I. Fundamental limitations. *J. Opt. Soc. Am. B*, 24(6):1324–1335, June 2007.

[19] Karl J. Åström and Tore Hägglund. *Advanced PID control*. ISA – Instrumentation, Systems, and Automation Society, 2006.

[20] Michał Odyniec. *RF and Microwave Oscillator Design*. Artech House, 2002.

[21] Enrico Rubiola. *Phase Noise and Frequency Stability in Oscillators*. Cambridge University Press Series, 2008.

[22] M. Lax. Classical noise. v. noise in self-sustained oscillators. *Phys. Rev.*, 160(2):290–306, 1967.

[23] D. Ham, W. Andress, and D. Ricketts. Phase noise in oscillators. In *Proc. of Second International Symposium on Acoustic Wave Devices for Future Mobile Communication Systems*, 2004.

[24] Y. Pomeau. The effect of a delay term on phase diffusion of a selfoscillator. *C. R. Acad. Sci. Paris*, 310(II):1025–1029, 1990.

[25] D. Goldobin, M. Rosenblum, and A. Pikovsky. Controlling oscillator coherence by delayed feedback. *Phys. Rev. E*, 67(6):061119–1 – 061119–7, 2003.

[26] Graham C. Goodwin, Stefan F. Graebe, and Mario E. Salgado. *Control System Design*. Prentice Hall PTR, 2000.

[27] J.A. Barnes et al. Characterization of frequency stability. *IEEE Trans. Instrum. Meas.*, IM-20(2):105–120, May 1971.

[28] J. Rutman and F.L. Walls. Characterization of frequency stability in precision frequency sources. In *Proc. of the IEEE*, volume 79(7), pages 952–960, 1991.

[29] E. Rubiola and V. Giordano. On the 1/f frequency noise in ultra-stable quartz oscillators. *IEEE Trans. Ultras. Ferroelec. and Freq. Contr.*, 54(1):15–22, January 2007.

[30] D. Wolf. 1/f-noise. In *Proc. of 5th Int. Conf. Noise, Bad Nauheim, West Germany*, pages 122–133, 1978.

[31] V.F. Kroupa, editor. *Frequency Stability: Fundementals and Measurement.* IEEE Press, 1984.

[32] Yang Jiang, Jin long Yu, Hao Hu, Wen rui Wang, Yao tian Wang, and En ze Yang. Phase-modulator-based optoelectronic oscillator for generating short optical pulse and microwave signal. *Opt. Eng.*, 46(9):090502–1 – 090502–3, September 2007.

[33] A.L. Lance, W.D. Seal., and F. Labaar. *Infrared and Millimeter Waves*, volume 11, chapter Phase Noise and AM Noise Measurements in the Frequency Domain, pages 239–289. Academic Press, 1984.

[34] MITEQ http://www.miteq.com.

[35] Poseidon Scientific Instruments Pty Ltd. http://www.psi.com.au.

[36] Wenzel Associates Inc. http://www.wenzel.com.

[37] C. McNeilage, J.H. Searls, E.N. Ivanov, P.R. Stockwell, D.M. Green, and M. Mossammaparast. A review of sapphire whispering gallery-mode oscillators including technical progress and future potential of the technology. In *Proc. of IEEE Intl. Freq. Control Symp. and Exposition*, 2004.

[38] OEwaves Inc. http://www.oewaves.com.

[39] R.A. Woode, M.E. Tobar, and E.N. Ivanov. An ultra-low noise microwave oscillator based on a high-Q liquid nitrogen cooled sapphire resonator. In *Proc. Intl. Freq. Control Symp.*, 1995.

[40] C.W. Nelson, A. Hati, D.A. Howe, and W. Zhou. Microwave optoelectronic oscillator with optical gain. In *Proc. Intl. Freq. Control Symp. and Europ. Freq. Time Forum Joint Meeting*, 2007.

[41] Shouhua Huang, Lute Maleki, and Thanh Le. A 10 GHz optoelectronic oscillator with continuous frequency tunability and low phase noise. In *Proc. Freq. Control Symp. and PDA Exhibition*, 2001.

[42] D. Eliyahu and L. Maleki. Tunable, ultra-low phase noise YIG based opto-electronic oscillator. *Proc. MTT-S 2003 - Philadelphia, PA*, pages 1–3, 2003.

[43] S. Poinsot, H. Porte, J.-P. Goedgebuer, W. T. Rhodes, and B. Boussert. Continuous radio-frequency tuning of an optoelectronic oscillator with dispersive feedback. *Optics Lett.*, 27(15):1300–1302, August 2002.

[44] X. Steve Yao and Lute Maleki. Dual microwave and optical oscillator. *Optics Lett.*, 22(24):1867–1869, December 1997.

[45] Y.K. Chembo, L. Larger, H. Tavernier, R. Bendoula, E. Rubiola, and P. Colet. Dynamic instabilities of microwaves generated with optoelectronic oscillators. *Optics Lett.*, 32(17):2571–2573, 2007.

[46] W.F. Walls. Practical problems involving phase noise measurements. In *Proc. of the 33rd Annual Precise Time and Time Interval (PTTI) Meeting*, pages 407–416, 2001.

[47] E. Rubiola and V. Giordano. Advanced interferometric phase and amplitude noise measurements. *Rev. Sci. Instrum.*, 73(6):2445–2457, 2002. Also http://arxiv.org, document arXiv:physics/0503015v1.

[48] F. Sthal, X. Vacheret, S. Galliou, P. Salzenstein, E. Rubiola, and G. Cibiel. Advanced bridge instrument for the measurement of the phase noise and of the short-term frequency stability of ultra-stable quartz resonators. In *Proc. Intl. Freq. Control Symp. and Europ. Freq. Time Forum Joint Meeting*, 2007.

[49] E. Rubiola, E. Salik, S. Huang, Nan Yu, and L. Maleki. Photonic-delay technique for phase-noise measurement of microwave oscillators. *J. Opt. Soc. Am. B - Opt. Phys.*, 22(5):987, May 2005.

[50] E. Rubiola. Tutorial on the double balanced mixer. *http://arxiv.org arXiv:physics/0608211*, 1:1–52, Aug 2006.

[51] E. Rubiola, V. Giordano, and J. Groslambert. Very high frequency and microwave interferometric phase and amplitude noise measurements. *Rev. Sci. Instrum.*, 70(1):220–225, January 1999.

[52] K. Volyanskiy, J. Cussey, H. Tavernier, P. Salzenstein, G. Sauvage, L. Larger, and E. Rubiola. Applications of the optical fiber to the generation and to the measurement of low-phase-noise microwave signals. *J. Opt. Soc. Am. B - Opt. Phys.*, 25(12):2140–2150, May 2008.

[53] E. Rubiola. The magic of cross correlation in measurements from DC to optics. In *Proc. Europ. Freq. Time Forum*, April 2008.

[54] P. Salzenstein, J. Cussey, X. Jouvenceau, H. Tavernier, L. Larger, E. Rubiola, and G. Sauvage. Realization of a phase noise measurement bench using cross correlation and double optical delay line. *Acta Phys. Polonica A*, 112(5):1107–1111, 2007.

[55] E. Rubiola and V. Giordano. Correlation-based phase noise measurements. *Rev. Sci. Instrum.*, 71(8):3085–3091, 2000.

[56] E. Rubiola and R. Boudot. The effect of AM noise on correlation phase noise measurements. *IEEE Trans. Ultras. Ferroelec. and Freq. Contr.*, 54(5):926–932, May 2006.

[57] F. Lardet-Vieudrin and E. Rubiola. Low flicker-noise amplifier for 50 Ω sources. *Rev. Sci. Instrum.*, 75(5):1323–1326, May 2004.

[58] Thorlabs. *Operation Manual. Thorlabs Instrumentation. Thermoelectric Temperature Controller TED200C*, 3.05 edition, 21.07.2008.

[59] W.S. Woodward. Simple design equations for thermoelectric coolers. *Electronic Design*, Online ID 6325, February 1998.

[60] K. Volyanskiy, Y. K. Chembo, E. Rubiola, A. Hmima, P. Salzenstein, and L. Larger. On the phase noise in optoelectronic oscillators. In *Proc.* XI International Conference For Young Researchers: Wave Electronics and its Applications in the Information and Telecommunication Systems, *St.Petersburg, Russia, 25–28 May 2008. In press.*, 2008.

[61] K. Volyanskiy, Y. K. Chembo, L. Larger, and E. Rubiola. DFB laser contribution to phase noise in an optoelectronic microwave oscillator. In *Proc.* Laser Optics *conference, St. Petersburg, Russia, 23–28 June 2008. Also http://arxiv.org arXiv:0809.4132v1*, 2008.

[62] E. Rubiola, V. Giordano, K. Volyanskiy, and L. Larger. Phase and frequency noise metrology. In *Proc. of 7th Symposium on Frequency Standards and Metrology, Pacific Grove, CA, USA, 5-11 October 2008. World Scientific 2009, in press. Open preprint arXiv:0812.0180v1*, 2008.

[63] Y. K. Chembo, K. Volyanskiy, L. Larger, E. Rubiola, and P. Colet. Determination of phase noise spectra in optoelectronic microwave oscillators: a Langevin approach. *IEEE J. Quantum Electron.*, 45(2):178–186, February 2009.

[64] W. Shieh, X. S. Yao, L. Maleki, and G. Lutes. Phase-noise characterization of optoelectronic components by carrier suppression techniques. In *Proc. of Optical Fiber Comm. (OFC) Conf. (San José, CA, 1998)*, pages 263–264, 1998.

[65] E. Rubiola, E. Salik, N. Yu, and L. Maleki. Flicker noise in high-speed photodetectors. *IEEE Trans. Microw. Theory Tech.*, 54(2):816–820, February 2006. also http://arxiv.org, document arXiv:physics/0503022v1, March 2005.

[66] W. Shieh and L. Maleki. Phase noise characterization by carrier suppression techniques in RF photonic systems. *IEEE Photonic Technology Lett.*, 17(2):474 – 476, February 2005.

[67] D.B. Leeson. A simple model of feedback oscillator noise spectrum. In *Proc. of IEEE*, pages 329–330, 1966.

[68] R.V. Pound. Electronic frequency stabilization of microwave oscillators. *Rev. Sci. Instrum.*, 17(11):490–505, November 1946.

[69] C. McNeilage, E.A. Ivanov, P.R. Stockwell, and J.H. Searls. Review of feedback and feedforward noise reduction techniques. In *Proc. Int. Freq. Control Symp.*, 1998.

[70] E.N. Ivanov, M.E. Tobar, and R.A. Woode. Advanced phase noise suppression technique for next generation of ultra-low noise microwave oscillator. In *Proc. Int. Freq. Control Symp.*, pages 314–320, 1995.

[71] X. Steve Yao and Lute Maleki. Multiloop optoelectronic oscillator. *IEEE J. Quantum Electron.*, 36(1):79–84, January 2000.

[72] T.C. Teyo, N.S. Mohd. Shah, P. Poopalan, and H. Ahmad. Regenerative erbium-doped fibre amplifier subject to external injection. *Optics Comm.*, 209:223–228, 2002.

[73] L. Maleki and D. Eliyahu. Low phase noise and spurious level in multi-loop opto-electronic oscillators. In *Proc. of the 2003 IEEE International Frequency Control Symposium and PDA Exhibition jointly with the 17th European Frequency and Time Forum*, pages 405–410, 2003.

[74] T. Bánky, B. Horváth, and T. Berceli. Optimum configuration of multiloop optoelectronic oscillators. *J. Opt. Soc. Am. B - Opt. Phys.*, 23(7):1371–1380, July 2006.

[75] Sang-Sun Lee, Sang-Gyu Park, and Myung-Ryul Choi. A design method for velocity-matched distributed photodetectors. *Journal of the Korean Physical Society*, 42(5):701–705, May 2003.

[76] Daniel Lasaosa, Jin-Wei Shi, Donato Pasquariello, Kian-Giap Gan, Ming-Chun Tien, Hsu-Hao Chang, Shi-Wei Chu, Chi-Kuang Sun, Yi-Jen Chiu, and John E. Bowers. Traveling-wave photodetectors with high power-bandwidth and gain-bandwidth product performance. *IEEE Journal of Selected Topics in Quantum Electronics*, 10(4):728–741, July/August 2004.

[77] K. S. Giboney et al. Traveling-wave photodetectors. *IEEE Photonic Technology Lett.*, 4 (12):1363, 1992.

[78] N. Pothecary. *Feedforward Linear Power Amplifiers.* Artech House, Norwood, MA, 1999.

[79] P.B. Kenington. *High linearity RF amplifier design.* Artech House, 2000.

[80] S. Römisch and F. Ascarrunz. An effective noise-reduction scheme for microwave amplifiers. In *Proc. of the 2003 IEEE International Frequency Control Symposium and PDA Exhibition Jointly with the 17th European Frequency and Time Forum*, pages 401–404, 2003.

[81] J.K.A. Everard and C.D. Broomfield. Reduced transposed flicker noise in microwave oscillators using GaAs-based feedforward amplifiers. *IEEE Trans. Ultras. Ferroelec. and Freq. Contr.*, 54(6):1108–1117, June 2007.

[82] R. Paschotta. *Encyclopedia of Laser Physics and Technology.* Wiley-VCH, Berlin, 2008.

[83] http://www.generalphotonics.com.

[84] A.A. Savchenkov, V.S. Ilchenko, A.B. Matsko, and L. Maleki. Photonic frequency synthesis and control with whispering gallery mode resonators. In *Holey Fibers and Photonic Crystals/Polarization Mode Dispersion/Photonics Time/Frequency Measurement and Control, 2003 Digest of the LEOS Summer Topical Meetings*, 2003.

[85] A.A. Savchenkov, A.B. Matsko, V.S. Ilchenko, N. Yu, and L. Maleki. Whispering-gallery-mode resonators as frequency references. II. Stabilization. *J. Opt. Soc. Am. B - Opt. Phys.*, 24(12):2988–2997, December 2007.